

# Slow and Fast Light in Semiconductors

*Forrest G. Sedgwick*



Electrical Engineering and Computer Sciences  
University of California at Berkeley

Technical Report No. UCB/EECS-2008-15

<http://www.eecs.berkeley.edu/Pubs/TechRpts/2008/EECS-2008-15.html>

February 14, 2008

Copyright © 2008, by the author(s).  
All rights reserved.

Permission to make digital or hard copies of all or part of this work for personal or classroom use is granted without fee provided that copies are not made or distributed for profit or commercial advantage and that copies bear this notice and the full citation on the first page. To copy otherwise, to republish, to post on servers or to redistribute to lists, requires prior specific permission.

**Slow and Fast Light in Semiconductors**

by

Forrest Grant Sedgwick

B.S. (University of California, Berkeley) 2000

A dissertation submitted in partial satisfaction of the

requirements for the degree of

Doctor of Philosophy

in

Engineering – Electrical Engineering and Computer Sciences

And the Designated Emphasis

in

Nanoscale Science and Engineering

in the

Graduate Division

of the

University of California, Berkeley

Committee in Charge:

Professor Constance J. Chang-Hasnain, Chair

Professor Ming C. Wu

Professor Peter Y. Yu

Spring 2008

The dissertation of Forrest Grant Sedgwick is approved:

---

Professor Constance J. Chang-Hasnain

---

Date

---

Professor Ming C. Wu

---

Date

---

Professor Peter Y. Yu

---

Date

University of California, Berkeley

Spring 2008



## **ABSTRACT**

### **Slow and Fast Light in Semiconductors**

by

Forrest Grant Sedgwick

Doctor of Philosophy in Engineering – Electrical Engineering and Computer Sciences

And the Designated Emphasis in Nanoscale Science and Engineering

University of California, Berkeley

Professor Connie J. Chang-Hasnain, Chair

Slow and fast light are the propagation of optical signals at group velocities below and above the speed of light in a given medium. There has been great interest in the use of nonlinear optics to engineer slow and fast light dispersion for applications in optical communications and radio-frequency or microwave photonics. Early results in this field were primarily confined to dilute atomic systems. While these results were impressive, they had two major barriers to practical application. First, the wavelengths were not compatible with fiber optic telecommunications. More importantly, the bandwidth obtainable in these experiments was inherently low; 100 kHz or less.

Within the last five years slow and fast light effects have been observed and engineered in a much wider variety of systems. In this work, we detail our efforts to realize slow and fast light in semiconductor systems. There are three primary advantages of semiconductor systems: fiber-compatible wavelengths, larger bandwidth, and simplification of integration with other optical components.

In this work we will explore three different types of physical mechanisms for implementing slow and fast light. The first is electromagnetically induced transparency (EIT). In transporting this process to semiconductors, we initially turn our attention to quantum dots or “artificial atoms”. We present simulations of a quantum dot EIT-based device within the context of an optical communications link and we derive results which are generally applicable to a broad class of slow light devices. We then present experimental results realizing EIT in quantum wells by using long-lived electron spin coherence.

The second mechanism we will explore is coherent population oscillations (CPO), also known as carrier density pulsations (CDP). We examine for the first time how both slow and fast light may be achieved in a quantum well semiconductor optical amplifier (SOA) while operating in the gain regime. Again, we simulate the device within an optical link and we study the limitations of the fast light effect using practical metrics such as bit error rate and power penalty. Finally we present some preliminary experimental results.

Our third study revolves around ultrafast intraband effects of spectral hole burning and carrier heating in SOAs. These experiments employ sub-picosecond pulses, demonstrating record-breaking bandwidth for slow and fast light of 1 THz. Our initial demonstration of fast light based on intraband processes achieves an advance of 2.5 times the input pulse width, an important milestone and a record for slow and fast light in semiconductors. Finally, we demonstrate a novel technique for improving performance by chirping the pulse at the input and then recompressing the pulse at the output. In addition to improving the fast light advance observed at gain bias, we observe

an unexpected tunable delay effect by changing the sign of the chirp at the input. When both the delay and advance are employed we observe a five-fold increase in temporal shift, more than 10 times the input pulse duration.

---

Professor Constance J. Chang-Hasnain  
Dissertation Committee Chair

---

Date

*To my parents Skip and Lana Sedgwick,  
and to Kathy  
for all the love and support*

# Contents

Acknowledgement .....	iii
1 Introduction .....	1
1.1 Applications.....	2
1.2 Definitions and Basic Equations.....	5
1.3 Kramers-Kronig Relations .....	9
1.4 General Analyses of Slow and Fast Light .....	10
2 Electromagnetically Induced Transparency.....	12
2.1 Basics of EIT.....	12
2.2 EIT in Quantum Dots .....	15
2.3 (001) and (110) QW, spin dephasing .....	23
2.4 Summary .....	30
3 Coherent Population Oscillations .....	31
3.1 Population Oscillations and Temporal Gratings .....	32
3.2 Experiments on QW .....	35
3.2.1 (001), Surface Normal, Absorption and MZI .....	36
3.2.2 (001), Surface Normal, Time Domain Measurements .....	41
3.2.3 (001), Waveguide, Room Temperature .....	47
3.3 Summary .....	52
4 Population Pulsations in Semiconductor Optical Amplifiers .....	53
4.1 Motivation.....	53
4.2 Background and Theory .....	54
4.3 Simulation of Slow Light Propagation.....	59
4.3.1 Single Device .....	60
4.3.2 Cascade .....	65
4.4 Simulation of Fast Light Propagation.....	68
4.5 Experimental Results .....	72
4.6 Summary .....	73
5 Intraband Effects in Semiconductor Optical Amplifiers.....	74
5.1 Motivation.....	74
5.2 Background: Ultrafast Carrier Dynamics in an SOA .....	76
5.2.1 Potential for Slow and Fast Light .....	78
5.3 Experimental Results .....	83
5.3.1 Setup, Equipment, and Techniques .....	83

5.3.2	Fast Light Results.....	84
5.3.3	Slow Light .....	88
5.3.4	Cascaded SOAs.....	91
5.3.5	SOA Loop.....	92
5.3.6	Multiple Pulses.....	95
5.3.7	Polarization .....	97
5.3.8	Pulse duration .....	99
5.4	TWDM: Chirped Input Pulses.....	101
5.4.1	Motivation and Theory .....	101
5.4.2	Chirper Experiments .....	102
5.4.3	Negative Chirp and Delay.....	107
5.4.4	Maximizing Delay and Advance .....	110
5.5	Theory and Simulation .....	113
5.5.1	Well-Known Effects.....	113
5.5.2	Nonlinear Group Index.....	116
6	Conclusion.....	123
7	Appendix: Auto- and Cross-Correlation .....	126
8	Bibliography .....	128

## Acknowledgement

One of the most fortunate blessings I have had in my life was to fall under the tutelage of my advisor, Connie Chang-Hasnain. Her technical knowledge and skills as a researcher have been a source of invaluable assistance in conducting all the work discussed in this dissertation and much, much more. Much more importantly her patience, wisdom, and inspiration have reached into all areas of my life; I deeply aspire to one day prove as much a wellspring of these truly precious gifts for my own students as she has been for myself. I am in debt to many of the faculty on campus, but I would like to explicitly express my gratitude to Professor J. Steven Smith, who helped me along

and provided encouragement and advice during a somewhat rocky first year of graduate school; Professor T. Kenneth Gustafson for helpful (and friendly!) discussions and for serving on my Qualifying Exam Committee; and to my Dissertation Committee, Professor Ming C. Wu and Professor Peter Y. Yu, without which this would not be possible.

All of the work presented in this dissertation was done in collaboration with too many colleagues to list here, but I am grateful to all of them for toiling with me. Specifically I would like to thank Pei-Cheng Ku, who was my first mentor and who brought slow and fast light to our group; Phedon Palinginis, a physicist providing heroic assistance to a group of engineers; Shanna Crankshaw and Bala Pesala, my partners in crime with whom I have struggled through many long and sleepless nights; Alexander Uskov, Michael Moewe, Michael Chung-Yi Huang, Xiaoxue “Wendy” Zhao, Ye “Mervin” Zhou, Linus Chuang, Chris Chase, Devang Parekh, Matthias Kuntz, Vadim Karagodsky, Roger Chen, Zhangyuan Chen, Carlos Mateus, Lukas Chrostowski, Nobby Kobayashi, Eui-Tae Kim, KobWai-Son “Wilson” Ko, Jui-Yen “Jason” Lin, and Chih-Yun “Steve” Wu – I am very proud to have been a part of CCHG with you. I am also grateful for our fantastic collaborators Professor Hailin Wang and his group at the University of Oregon, and Professor Shun-Lien Chuang and his group at the University of Illinois, Urbana-Champaign.

On a personal note, I would like to thank all of my friends and family, especially Sean, Melissa, and Kathy, for bringing balance and love into my life. I have had a hundred great teachers throughout my lifetime and I wish I could thank them all here. But I am

lucky beyond reason to have had such wonderful parents, my first teachers, who fed my curiosity, instilled me with self-discipline, supported me with their faith, and filled my childhood with love. Lastly, I am profoundly grateful for the abilities and opportunities God has given me, the lessons I have been taught, and all the lessons yet to learn.

# 1 Introduction

The term “slow light” refers to the propagation of an optical signal through a device with a speed considerably less than  $c/n$ , where  $c$  is the speed of light in a vacuum and  $n$  is an average index of refraction of the device. Conversely, the term “fast light” refers to the propagation of a signal through a device with a speed in excess of  $c/n$ . Throughout this work, an optical signal will be a slowly-varying modulation, usually of the amplitude, of an optical-frequency sinusoidal “carrier”.

In the February 1999 issue of *Nature*, researchers led by Lene Hau at Harvard University announced an experimental demonstration of light pulses propagating through a Bose-Einstein condensate at 17 m/s [1]. This result captured the imagination of both the scientific community and the popular press. Thus began a rapid increase in publications focused both on generating slow light, and on potential applications of the effect.

The principles behind the results presented in [1] were not new; the idea of realizing extremely low group velocity via electromagnetically induced transparency (EIT) goes back to theoretical work done by Harris et. al. in July of 1992 [2] and experimental observations of a 165-fold reduction in pulse propagation velocity via EIT were reported Kasapi et. al. in March of 1995 [3]. In fact, the extremely slow and fast group velocity associated with atomic absorptions lines have been known since the beginning of the 20<sup>th</sup> century [4], but were practically unobservable at the time. The results of the 1990’s were produced by technological and theoretical advances which allowed the creation of

dispersive and absorptive spectral features not found in nature and enabled the direct observation of the associated extreme group velocities.

Part of the rapid growth of the slow light field has been due to the realization that a wide variety of physical effects can also produce similar dispersion, allowing a body of earlier work to be re-examined for potential slow and fast light applications. We will see later in this section that the heroic bicycle-speed velocities of the early experiments are accompanied by very small bandwidths, making them unsuitable for many types of practical applications.

## 1.1 Applications

Applications for slow light are divided into two main categories. The first consists of those applications which benefit purely from the “slowness.” These are applications such as nonlinearity enhancement [6,5,7] single-photon quantum optics [8]. For these applications, slow light serves to increase the interaction time between a pulse and a medium or between two optical pulses. Additionally, slow light effects compress a pulses spatially. A 2.5  $\mu\text{s}$  pulse which is 750 m long while propagating in free space is compressed to 43  $\mu\text{m}$  after upon entering the slow light medium (a pulse entering a fast light medium undergoes a corresponding stretching). This compression further enhances optical nonlinearities [1,6]. As we shall see in Section 1.3, slow light is linked to an increase in transmission or suppression of absorption, another highly desirable property when working with single photon pulses.

The second class of applications consists of those that make use of the additional ability to adjust the group index over a wide range in most slow and fast light systems.

This class of applications is the primary target of the research presented in this work. Dynamical changes of the slow and fast light medium are the basis of halted light [10,9] and stored light [11] experiments. Our primary interests lay in two broad subsets of applications within this class: radio frequency (RF) photonics [12] and all-optical networking [13].

The basic premise of RF photonics is that microwave signals on transmission lines are replaced by modulated light beams in fibers. A very broadband microwave signal becomes a narrow band signal in the optical domain, simplifying design [14]. For example, a device with a DC to 300 GHz bandwidth is difficult to implement with microwave components, but a similar bandwidth requirement is trivial for optical fibers, amplifiers, phase shifters, etc [15]. Of particular relevance to slow and fast light research is the construction of broad bandwidth delay lines. Time delay is a functional building useful for constructing RF filters with arbitrary responses, for antenna remoting, and for many other types of signal processing [12,14,16]. The variable nature of the time delays produced by slow and fast light devices offers the ability to create rapidly reconfigurable or even general microwave signal processing components.

Another field in which slow and fast light may have a major impact is in the realization of an all-optical packet switched network. Current fiber optic packet-switched networks rely on optical transmission of data point-to-point, with electronic switching and processing of packets at each router. Recent experimental research has provided potential methods of switching [17] and regenerating [19,18] packets in the optical domain, without need for optical-electronic conversion. When two packets

arrive at a switch simultaneously and both are to be routed to the same output port there is a risk that one of the packets will be lost or “dropped.” Dropping packets is avoided by use of a buffer, which stores incoming packets until their destination port is free. An all-optical buffer is a crucial component in realizing an all-optical network, yet a practical approach for realizing such a device remains elusive. Slow and fast light effects offer a basis for constructing a compact all-optical buffer [20,13].

The most important performance metrics for a buffer are storage capacity, bandwidth, retrieval latency, and size [13,21]. A variable delay line can act as a buffer by delaying packets on an incoming port until the destination port is free. The storage capacity of such a device is the amount of delay divided by the duration of a bit (in this work we will always take a bit to be an optical pulse, i.e. NRZ or RZ amplitude modulation). A simple method of implementing a variable delay is to select from an array of fiber loops of various lengths. Such a buffer can store a very large number of bits at very high bandwidths. However, once bits are sent on a loop, they cannot be retrieved until they have traversed the loop; the retrieval latency is poor. Also, calculations have shown that the buffering capacity of a typical large-scale “core” router operating at 40 Gbps would demand 40 Gm of fiber [21]. By decreasing the propagation speed of light, a far shorter device is required. If the slow light effect can be switched off while pulses are in the device, then the retrieval time is also greatly improved.

## 1.2 Definitions and Basic Equations

To explore the propagation of light in a medium, we want to solve the following problem. Given the electric field as a function of time at a point in space called the source (for convenience taken to be at the origin), find the electric field at every other point in space. The time and space behaviors of the electric field are linked to each other via the wave equation

$$\frac{\partial^2 E}{\partial z^2} - \frac{1}{c^2} \frac{\partial^2 E}{\partial t^2} = \mu_0 \frac{\partial^2 P}{\partial t^2} \quad 1.1$$

where for pedagogical purposes we have restricted ourselves to a single spatial dimension. Eq. (1.1) is derived from Maxwell's equations for an insulating, dielectric medium with no free currents or charges. The response of the material to the electric field  $E(z, t)$  is to acquire a polarization  $P(z, t)$ .

One way to solve (1.1) is to use a Fourier transform in space and in time such that  $E(z, t) \rightarrow E(k, \omega)$ , where  $k$  is the spatial frequency (also called wave vector or, in complex structures, the propagation constant) and  $\omega$  is the temporal frequency. If the response of the material is linear, then we can write

$$P(\omega) = \epsilon_0 \chi(\omega) \cdot E(\omega) \quad 1.2$$

which defines the electric susceptibility  $\chi$ . Equation (1.1) then becomes an algebraic equation

$$k(\omega) = \sqrt{1 + \chi(\omega)} \cdot \frac{\omega}{c} = n(\omega) \cdot \frac{\omega}{c} \quad 1.3$$

where we have defined the refractive index  $n \equiv \sqrt{1 + \chi}$ . Thus the spatial and temporal frequencies are not independent, and we can consider  $k$  to be a function of  $\omega$ . Taking the inverse Fourier transform in the spatial dimension

$$E(x, \omega) = E(0, \omega)e^{ik(\omega) \cdot z} = E(0, \omega)e^{i\frac{\omega}{c}n(\omega) \cdot z} \quad 1.4$$

gives the field at an arbitrary point  $x$  and solves our problem. We can see from Eq. (1.4) that the field at  $z$  is related to the field at the origin by a frequency-dependent phase shift. If  $n$  is constant, then this phase shift is proportional to  $\omega$ . A linear phase shift in the frequency domain corresponds to a temporal shift in the time domain and thus, after taking the inverse Fourier transform again

$$E(x, t) = \int E(0, \omega)e^{i\frac{\omega}{c}n \cdot z} dt = E(0, t - z/v_p). \quad 1.5$$

where

$$v_p \equiv \frac{c}{n} = \frac{c}{\sqrt{1 + \chi}} \quad 1.6$$

is called the phase velocity. This is the speed at which the electric field propagates from the source at the origin to other points. Equation (1.5) also shows that the refractive index  $n$ , in addition to being the ratio between  $k$  and  $\omega$ , is also the ratio of  $c$  to the phase velocity.

In general the susceptibility and refractive index are not constant. In this case we expand Eq. (1.3) in a Taylor series about the frequency  $\omega_0$

$$k(\Delta\omega) = k^{(0)} + k^{(1)}\Delta\omega + \frac{1}{2}k^{(2)}(\Delta\omega)^2 + \dots \quad 1.7$$

where  $\Delta\omega = \omega - \omega_0$  and  $k^{(n)} = \partial^n k / \partial \omega^n$  evaluated at  $\omega_0$ . This expansion is most relevant for signals with a narrow spectrum centered about  $\omega_0$ . In the time domain, these signals can be written

$$E(t) = A(t)e^{i\omega_0 t} + c.c. \quad 1.8$$

where  $A(t)$  is a slowly varying, complex amplitude. The rapidly varying sinusoidal oscillation at  $\omega_0$  is called the carrier. In analogy with Eq. (1.5),

$$A(z, t) = A(0, t - k^{(1)}z) = A(0, t - z/v_g) \quad 1.9$$

where

$$v_g \equiv \frac{1}{k^{(1)}} = \left(\frac{\partial k}{\partial \omega}\right)^{-1} \quad 1.10$$

is the group velocity. For a dispersionless medium or vacuum,  $k^{(1)}$  is the only non-zero term in Eq. (1.7) and the group velocity is equal to the phase velocity. If dispersion is linear,  $k^{(0)}, k^{(1)} \neq 0$ , then the amplitude  $A(z, t)$  propagates at  $v_g$ , while the phase of the carrier propagates at the phase velocity (Eq. (1.6))  $v_p = \omega/k^{(0)}$ .

In nature, the index of refraction ranges typically between 1 and 5 and the phase velocity is never more than an order of magnitude less than  $c$ . However, the group velocity also depends on the frequency derivative of  $n$

$$v_g(\omega) = \frac{c}{n + \omega \cdot \partial n / \partial \omega} \quad 1.11$$

or

$$v_g(k) = \frac{c}{n} \left(1 - \frac{k}{n} \cdot \frac{\partial n}{\partial k}\right). \quad 1.12$$

If  $n(\omega)$  changes rapidly over a small frequency range, even if by only a small amount, then the derivative in (1.11) may be very large and  $v_g$  can be many orders of magnitude less than  $c$ . This is the quintessential slow light effect. If  $n(\omega)$  is decreasing, then the derivative is negative and  $v_g > v_p$ . This is called fast light. In analogy to the index of refraction (see Eq. (1.6) ), it is useful to define a group index

$$n_g \equiv n + \omega \cdot \partial n / \partial \omega = \frac{c}{v_g}. \quad 1.13$$

The delay of an optical signal is proportional to  $n_g$  which often makes it a more convenient parameter than  $v_g$  for calculations.

In Section 1.1 we discussed our target applications, which revolve around using slow and fast light to produce tunable time shifts. If group velocity can be swept from a very large value to a very small value, then a large temporal shift can be obtained with a short device. Therefore, a large change in group velocity is our first performance metric when comparing slow and fast light systems. In practice, this is accomplished not by changing the magnitude of  $n$ , but by changing  $\partial n / \partial \omega$ .

The importance of the slope of  $n(\omega)$  leads to an important trade-off and to our second performance metric. A small but finite change in  $n$  can produce an arbitrarily low  $v_g$  if  $n$  changes over an arbitrarily small spectral width  $\Delta\omega$ . Indeed, the impressive  $v_g$  of 17 m/s obtained in [1] was not due to a particularly large  $\Delta n$  but rather that the quantum coherence in the Bose-Einstein condensate allowed for a spectral feature of extremely narrow  $\Delta\omega$ , on the order of 1 MHz. However, if the spectral width of the feature is decreased, the bandwidth of the delayed pulses must also decrease, and

hence the duration of the pulses must increase. The *fractional* delay, the delay normalized to the input pulse duration, remain *unchanged*. This important constant is called the delay-bandwidth product (DBP) or, in the case of fast light, advance-bandwidth product (ABP). These terms are somewhat of a misnomer, in much of the literature they do not refer to the product of the pulse bandwidth and delay, but rather to the delay divided by the duration of the pulse, usually measured at FWHM. For an optical buffer application, DBP is equivalent to storage, and can be given the units of “bits.”

The higher order terms in (1.7) are called the group velocity dispersion (GVD). In general these terms are responsible for pulse broadening and distortion. It is important to note that a careful examination of (1.11) shows that a constant  $\partial n/\partial\omega$  does not produce a constant group velocity.

### 1.3 Kramers-Kronig Relations

If the polarization response of the material to the electric field is linear, it can be written as

$$P(t) = \int E(\tau)\chi(\tau - t)d\tau \quad 1.14$$

where  $\chi(\tau)$  is the impulse response of the material. The restriction of causality implies that the impulse response of the system must be zero before the impulse arrives, i.e.  $\forall t < 0, \chi(t) = 0$ . We also assume that the response of the system is finite, i.e. as  $t \rightarrow \infty, \chi(t) \rightarrow 0$ . This assumption must be true for any passive system, but is not necessarily true for an active system. These conditions place restrictions on the

frequency domain response of the medium  $\chi(\omega)$  (for derivation, see Appendix E of [22]).

$$\chi_{Re}(\omega) = \frac{1}{\pi} \cdot P \int \frac{\chi_{Im}(\omega')}{\omega' - \omega} d\omega' \quad 1.15$$

$$\chi_{Im}(\omega) = -\frac{1}{\pi} \cdot P \int \frac{\chi_{Re}(\omega')}{\omega' - \omega} d\omega' \quad 1.16$$

where  $\chi_{Re}$  and  $\chi_{Im}$  are the real and imaginary parts of  $\chi(\omega)$  and  $P \int$  is the principle value integral.

The Kramers-Kronig relations are difficult to use in practice because of their integral nature. A large absorption peak located very far from a range of frequencies of interest can still significantly affect the dispersion. However, the link between the absorption spectrum ( $\chi_{Im}$ ) and the refractive index is an important heuristic for understanding slow light systems. Narrow changes in the absorption spectrum must be accompanied by spectrally narrow change in the refractive index, and therefore a large or small group index. We will see that the physical effects employed to create these narrow spectral features are nonlinear. However, the response to a weak probe or signal remains linear, and the nonlinearities due to any strong control or pump fields are treated as a modification to the linear response experienced by the signal. In this case, Equations (1.15) and (1.16) remain valid for the signal.

#### 1.4 General Analyses of Slow and Fast Light

An ideal slow or fast light device has a constant group velocity and flat absorption spectrum over the bandwidth of a potential signal. For a constant group velocity, the

coefficients of Eq. (1.7) must satisfy  $k^{(m)} = 0$  for  $m > 1$ . Noting that the group index  $n_g = ck^{(1)}/2$ , the ideal dispersion of the refractive index is

$$n(\omega)_{ideal} = n_g + (n_0 - n_g) \frac{\omega_0}{\omega} \quad 1.17$$

where  $n_0$  is the refractive index at  $\omega_0$ . When the spectral width of the dispersion is small, the situation most commonly of interest is slow light devices, then  $\omega \cong \omega_0$  and

$$n(\omega)_{ideal} \simeq n_0 - (n_0 - n_g) \frac{\Delta\omega}{\omega_0} + (n_0 - n_g) \left(\frac{\Delta\omega}{\omega_0}\right)^2 + \dots \quad 1.18$$

As mentioned earlier, it is important to note that a refractive index which is linear in  $\omega$  does not offer a constant group velocity. Even if the bandwidth of a signal fits entirely within a linear regime of  $n(\omega)$ , the length over which the signal may propagate without distortion, and hence the maximum delay it can experience, will be limited by the GVD.

A very useful approximation for estimating the group index of the resonances which we will study in this work can be derived by considering a homogeneously broadened two-level system. Detailed variations of the susceptibility  $\chi(\omega)$  due to this transition are given in many textbooks covering quantum electronics, for example [23]. Under the assumption  $\chi/n_{bac} \ll 1$ , the absorption  $\Delta\alpha$  and index  $\Delta n$  due to the transition are

$$\Delta\alpha(\delta) = \frac{\Delta\alpha_0}{(\Delta\omega/2)^2 + \delta^2} \cdot \left(\frac{\Delta\omega}{2}\right)^2 \quad 1.19$$

$$\Delta n(\delta) = \frac{\delta}{(\Delta\omega/2)^2 + \delta^2} \cdot \frac{\Delta\omega\Delta\alpha_0}{4} \quad 1.20$$

where  $\delta$  is the frequency detuning from the transition frequency,  $\Delta\alpha_0$  is the change in absorption at  $\delta = 0$ , and  $\Delta\omega$  is the FWHM of the absorption line. The group index at the

center of this Lorentzian absorption peak can be found by taking the derivative of Eq. (1.20), assuming that  $\omega \cdot dn/d\omega \gg n_0$ , and then using the definition of  $n_g$ , Eq. (1.13), we obtain

$$n_g(\delta = 0) \cong \frac{\alpha_0}{\Delta\omega}. \quad 1.21$$

Though Eq. (1.19) and (1.20) were obtained for an absorption peak with low background absorption, Eq. (1.21) can be used quite generally to estimate group index even when the resonance is a Lorentzian dip in a constant background absorption.

## 2 Electromagnetically Induced Transparency

### 2.1 Basics of EIT

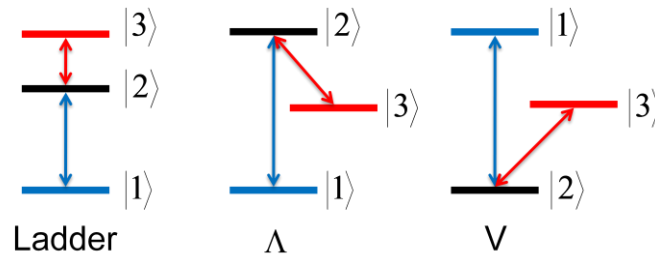


**Figure 2.1.** The three classes of EIT systems: Ladder or cascade (left), Lambda (center), and Vee (right). Two of the transitions are dipole allowed ( $|1\rangle \rightarrow |2\rangle$  and  $|2\rangle \rightarrow |3\rangle$ ) and one is forbidden ( $|1\rangle \rightarrow |3\rangle$ ).

Electromagnetically induced transparency (EIT) is a Raman process involving three states and two coherent optical electromagnetic fields. One of the fields, the “probe” or “signal,” is a weak perturbation relative to the other field, the “pump” or “control” field. The driving fields are each resonant with a different dipole-allowed transition. The third transition in the three state system is dipole forbidden. Figure 2.1 shows three different “classes” of EIT systems: the ladder, the lambda, and the V. We use the convention of Ku [24] whereby the states are numbered such that the  $|1\rangle \rightarrow |2\rangle$  and the  $|2\rangle \rightarrow |3\rangle$

transitions are dipole allowed and correspond to the signal and pump, respectively. The  $|1\rangle \rightarrow |3\rangle$  transition is dipole forbidden.

The signal and pump are described in terms of the optical frequencies  $\omega_s$  and  $\omega_p$ , respectively, and the Rabi frequencies  $\Omega_{s,p} \equiv \mu E_{s,p}/2\hbar$ , where  $\mu$  is the dipole moment of the appropriate transition and  $E$  is the electric field amplitude. The coherence  $\sigma_{xy}$  of the  $|x\rangle \rightarrow |y\rangle$  transition is defined as the slowly varying envelope of the appropriate off-diagonal element of the density matrix:  $\sigma_{xy} \equiv \langle x|\hat{\rho}|y\rangle e^{i\omega_s t}$  [25]. All of the influence of the material upon the propagation of the field is due to the coherence of the relevant transition; thus our goal is to calculate the coherence at the signal frequency and thus determine the absorption, refractive index, and group index experienced by the signal. For definiteness we will choose a ladder system as discussed in detail in [24].

The time evolution of the  $|1\rangle \rightarrow |2\rangle$  coherence is given by

$$\dot{\sigma}_{21} = -i\Omega_s N_{21} - (\gamma_{21} + i\delta_s)\sigma_{21} + i\Omega_p^* \sigma_{31} \quad 2.1$$

where  $N_{xy} \equiv \rho_{xx} - \rho_{yy}$  is the population difference between  $|x\rangle$  and  $|y\rangle$ ,  $\gamma_{xy}$  is the dephasing rate of the  $|x\rangle \rightarrow |y\rangle$  transition, and  $\delta_s \equiv \Delta E_{21}/\hbar - \omega_s$  is the detuning between the signal field and the  $|1\rangle \rightarrow |2\rangle$  transition. The first two terms on the RHS of Eq. (2.1) yield a typical Lorentzian absorption peak of width  $\gamma_{21}$ . This is the absorption spectrum which the signal would experience in the absence of the pump. The third term asserts that if coherence exists between states  $|1\rangle$  and  $|3\rangle$  then the pump field, which connects states  $|3\rangle$  and  $|2\rangle$ , generates coherence between  $|2\rangle$  and  $|1\rangle$ . One should not view this process as population transferred from  $|1\rangle$  to  $|3\rangle$  and then from  $|3\rangle$  to  $|2\rangle$ , but more like a two-photon resonant Raman process.

Assuming that the pump detuning is zero ( $\delta_p \equiv \Delta E_{32}/\hbar - \omega_p = 0$ ) and that  $\Omega_p \gg \Omega_s$ , the time evolution for the  $|1\rangle \rightarrow |2\rangle$  coherence is given by

$$\dot{\sigma}_{31} = -(\gamma_{31} + i\delta_s)\sigma_{31} + i\Omega_p\sigma_{21}. \quad 2.2$$

The first term is due to the pump and signal fields, the second term mirrors the third term in (2.1); the pump field transforms coherence between  $|2\rangle$  and  $|1\rangle$  into coherence between  $|1\rangle$  and  $|3\rangle$ .

The steady state solution for Eq. (2.2) is

$$\sigma_{31} = \frac{i\Omega_p}{(\gamma_{31} + i\delta_s)} \cdot \sigma_{21}. \quad 2.3$$

Substituting (2.3) into (2.1), the steady state solution of Eq. (2.1) is

$$\sigma_{21} = -\frac{i\Omega_s N_{21}}{\gamma_{21} + i\delta_s + |\Omega_p|^2/(\gamma_{31} + i\delta_s)}. \quad 2.4$$

When no pump is present, (2.4) reduces to

$$\sigma_{21}^{(0)} = -\frac{i\Omega_s N_{21}}{\gamma_{21} + i\delta_s} \quad 2.5$$

which is the response of a simple homogeneously broadened two level system. When  $\delta_s \rightarrow 0$ ,  $\sigma_{12}^{(0)}$  is large and imaginary, corresponding to an absorption peak. However,  $\sigma_{31}$  also peaks as  $\delta_s \rightarrow 0$  (for an ideal EIT system  $\gamma_{31} \rightarrow 0$ ). By inspection of Eq. (2.1), we see that if we wish to maintain  $\dot{\sigma}_{21} = 0$  then  $\sigma_{21}$  must decrease. This is the behavior observed in Eq. (2.4). For a good EIT system,  $\gamma_{21} \gg \gamma_{31}$  such that  $\sigma_{21} \sim \sigma_{21}^{(0)}$  when  $\delta_s \gg \gamma_{31}$  and  $\sigma_{21} \rightarrow 0$  as  $\delta_s \rightarrow 0$ . These conditions describe a spectrally narrow transparency region embedded within a homogeneously broadened absorption line.

Figure 2.2(a) shows the absorption experienced by the signal with the pump on (red, solid) and pump off (black, dashed). Our interest in the spectrally narrow absorption window created by EIT lies in the corresponding large dispersion of refractive index, Figure 2.2(b). We stress once more that the “hole” is created in a homogeneously broadened absorption line; thus EIT is a very different process than “spectral hole burning” – the creation of an absorption dip in an inhomogeneously broadened line via saturation.

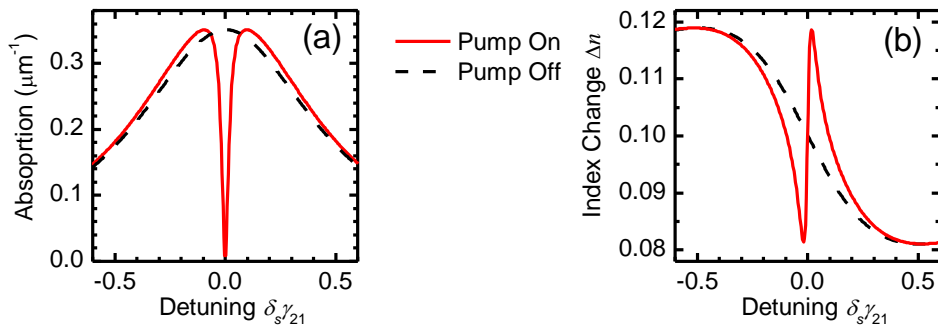


Figure 2.2(a). Typical signal absorption spectrum with the pump off (black) and pump on (red). Switching on the pump creates a narrow “hole” in the absorption line. Figure 2.2(b). Change in refractive index due to the  $|1\rangle \rightarrow |2\rangle$  transition with the pump off (black) and pump on (red). The steep positive dispersion at  $\delta_s = 0$  causes slow light.

## 2.2 EIT in Quantum Dots

Quantum dots (QD) [26] provide atom-like energy structures within a semiconductor material system and therefore offer an obvious method for transporting a process from atomic systems to semiconductors. Chang-Hasnain et. al. [13] and Ku et. al. [20,24] give detailed theoretical analyses regarding the use of InAs QD for an EIT-based optical buffer. In this section, we will describe a simulation of an optical communications data link through such an EIT-based device. The device itself will consist of a waveguide of length  $L$  with multiple layers of dots embedded within [20,13]. Using this simulation, we

hope to quantify distortion, residual absorption, and delay with practical metrics such as bit error rate (BER) and power penalty.

A simplified schematic of the two CB levels and a single VB level involved in the EIT scheme is shown in Figure 2.3(a). The signal is resonant with the interband transition while the pump is resonant with the intersubband transition. The low occupation of  $|2\rangle$  at thermal equilibrium ensures that the pump can propagate with minimal absorption, and in all our calculations we will assume that the pump power is constant along the length of our device. The pump intensity considered will be  $5 \text{ MW/cm}^2$ , an easily attainable value in a waveguide device. The electric susceptibility for the signal due to EIT is

$$\chi_{EIT}(\omega_s) = -i \frac{\Gamma |\mu_{21}|^2}{V \epsilon_0} \frac{N_{21}}{\gamma_{21} + i\delta_s + |\Omega_p|^2 / (\gamma_{32} + i\delta_s + i\delta_p)} \quad 2.6$$

where  $\Gamma$  is an optical confinement factor,  $V$  is the volume of a single quantum dot and  $\mu_{21}$  is the dipole matrix element between  $|2\rangle$  and  $|1\rangle$ . The effects of pump detuning  $\delta_p$  have also been included here. Our device consists of an array of quantum dots embedded with a waveguide. We assume a homogeneous linewidth  $2\gamma_{21}$  of 1 meV and a non-radiative coherence rate  $\gamma_{31}$  of  $10 \mu\text{eV}$  [13]. We will neglect inhomogeneous broadening in the calculations presented here.

A schematic of the simulation is shown in Figure 2.3(b). The process begins with a stream of pseudo-random data expressed as ideal square pulses (amplitude modulated NRZ encoding) at bit rate  $B$ . These pulses are smoothed by a low pass filter. The data stream is Fourier transformed to the frequency domain and the frequency components

mapped onto values of the signal detuning (we will take the pump detuning to be zero for all of these calculations). For each frequency component, the amplitude is scaled and the phase shifted in accordance with Eq. (2.6). After the slow light device, the signal is converted back to the time domain with an inverse Fourier transform and then the amplitude of the signal is scaled to the average power level  $P_{rec}$  desired at the receiver. The power penalty, discussed in more detail later, is obtained from measurements of BER as a function of  $P_{rec}$ .

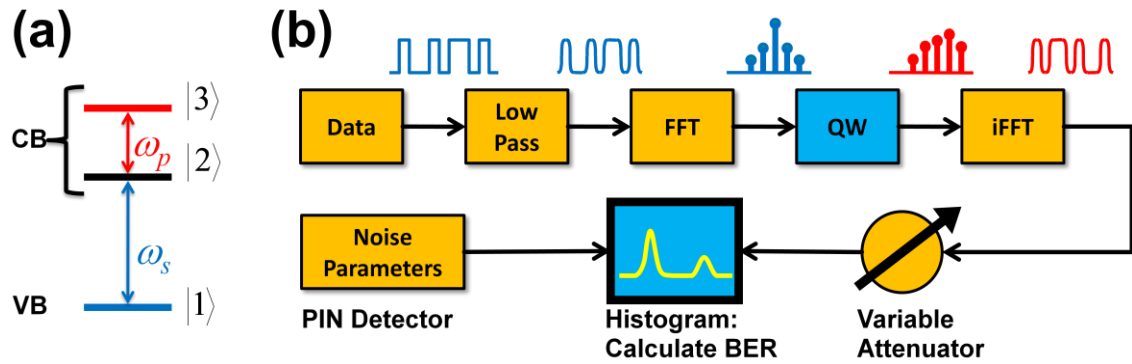


Figure 2.3(a). Energy levels for our ladder type EIT scheme. The pump is resonant with a CB intersubband transition and the signal with an interband transition. The low occupation of  $|2\rangle$  at thermal equilibrium prevents the pump from being absorbed. The absorption dip due to EIT reduces or eliminates absorption of the signal. Figure 2.3(b). Schematic of the simulated link employing the QD-based EIT device as a buffer. A pseudo-random bit stream is propagated through an EIT susceptibility. The intensity level at the middle of each bit period and the noise statistics of a PIN detector are combined to form a histogram. The bit error rate of the link is extracted from the histogram as a function of received power.

Every data stream begins with a one followed by several zeros to act as a synchronization pulse. The shift in the maximum of this pulse is used to measure delay. Also, the “clock” at the receiver is set to this point, i.e. after this instant the intensity will be sampled at a period  $B^{-1}$  to determine the received bits. Ideally, if the intensity is above half the average received power, the bit is a one, while if it is below it is a zero. However, noise must also be taken into account or else the BER may be zero even at infinitesimally small values of  $P_{rec}$ . The noise is modeled by assuming a normal

distribution about the actual intensity and is parameterized by the intensity-dependent variance  $\sigma$ . The probability that an individual bit is misinterpreted is then given by integrating the normal distribution from the threshold to  $\infty$  for a one or to  $-\infty$  for a zero [27]. The BER is then determined by adding up the error probabilities of the individual bits. Our simulation assumes a PIN type detector and models thermal noise and shot noise, where we assume that the detected intensity is large enough that the shot noise can be described by a normal distribution.

As long as the intensity at the decision instant remains on the correct side of the threshold level, then an arbitrarily low BER can be obtained sufficient amplification of the signal. A performance metric which takes this dependence of BER on  $P_{rec}$  into account is the power penalty. For a given link, the power required to obtain a specified BER (usually  $10^{-9}$ ) is measured with and without the device under consideration. The difference in required received power is the power penalty.

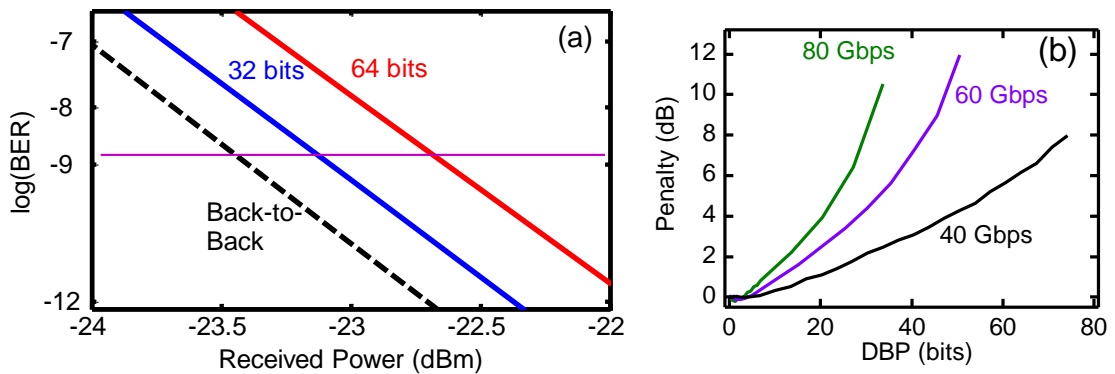


Figure 2.4(a). BER vs. received power  $P_{rec}$  for three different storage capacities (DBP) at 10 Gbps. First, the back to back case (black, dashed): there is no slow light device and the BER at low  $P_{rec}$  is caused solely by the noise at the receiver. Next the length of the device is adjusted such that 32 bits (blue) and 64 bits (red) are stored in the device. The power penalty is the increase in power from the back to back case required to maintain a BER of  $10^{-9}$ . The penalty is 0.3 dB and 0.8 dB for the 32 and 64 bit buffers, respectively. Figure 2.4(b). Power penalty as a function of DBP for three different bit rates. The DBP is increased by increasing the length of the device. The cost of higher storage is a higher power penalty.

Typical results from the  $P_{rec}$  sweeps are shown in Figure 2.4(a). Here the device length is changed to show BER vs.  $P_{rec}$  for different storage capacities (DBP) at 10 Gbps. The dotted black line shows the back to back case, DBP = 0. The BER here is caused only by the noise at the receiver. When the signal is passed through a DBP = 32 device, there is some amount of distortion and more received power is required to maintain the same BER. A longer device (64 bits) requires still more power. The power penalty is measured by taking the increase in  $P_{rec}$  at a BER of  $10^{-9}$  (purple line) relative to the back to back case. At 10 Gbps, it is 0.3 dB and 0.8 dB for the 32 bit and 64 bit buffers, respectively. Figure 2.4(b) plots power penalty as a function of DBP at 40 Gbps (black), 60 Gbps (violet), and 80 Gbps (green). The DBP is increased by increasing the device length. The increase of penalty with  $B$  is not surprising, since we expect higher bandwidth signals to experience more GVD and gain dispersion as the high frequency components fall further from the center of the absorption dip. However, one immediately sees that there is also a trade-off between power penalty and the amount of storage one requires. Therefore DBP cannot be increased arbitrarily by increasing  $L$ .

Under the simplest analysis of the DBP of a slow light system, the DBP scales linearly with increasing device length. To first order, DBP is maximized when the signal bandwidth,  $B$ , is set equal to the FWHM of the absorption dip,  $\Delta\omega$ . Thus from Eq. (1.21)  $DBP \approx \Delta\alpha_0 L$  [28]. However, this approximation is only valid for a short device, where the bandwidth of the transmission is equal to the absorption dip FWHM. A long device can be pictured as a series of short devices, each a bandpass filter with width  $\Delta\omega$ . The bandwidth of the cascade is less than the bandwidth of the individual “filters”.

More quantitatively, the transmission  $T$  is related to the absorption by  $T = \exp(-\alpha L)$ . The exponential dependence of  $T$  upon  $\alpha$  means that the bandwidth narrows with increasing  $L$ . We can write  $T$  as a function of detuning  $\delta$  from the absorption dip center

$$T(\delta) = e^{-\alpha_{bac} L} e^{-\Delta\alpha(\delta)L} \quad 2.7$$

where  $\alpha_{bac}$  is the background absorption. Assuming a Lorentzian absorption dip (Eq. (1.19) ) of depth  $-\Delta\alpha_0$  and FWHM  $\Delta\omega$ , we define  $T_0$  as the transmission at the bottom of the dip and set  $T(\delta_{3dB})/T_0 = 1/2$  to find that the 3 dB transmission bandwidth

$$2\delta_{3dB} = \Delta\omega \sqrt{\frac{\ln(2)}{\ln(2) + \Delta\alpha_0 L}} \quad 2.8$$

For long devices,  $\delta_{3dB} \sim L^{-1/2}$ . Since delay is proportional to  $L$ , we surmise that if restrict the signal bandwidth to be less than or equal to the transmission bandwidth, then the DBP goes as  $\sqrt{L}$ .

Figure 2.5(a) plots  $T(\delta)/T_0$  as a function of  $\delta$  for various device lengths, as calculated numerically from the actual EIT dispersion (2.6). As  $L$  increases, the transmission window narrows. Figure 2.5(b) plots the delay-bandwidth product as a function of  $L$ , obtained by multiplying the 3 dB bandwidth by the group delay at  $\delta = 0$  (technically, this literal delay-bandwidth product is proportional to, but not the same as, the DBP as defined in Section 1.1). The fit is very close to a square root dependence, indicating that our simpler analysis with a Lorentzian hole is a very good one. Note that this analysis overestimates the DBP because it does not take further limitations due to GVD into account.

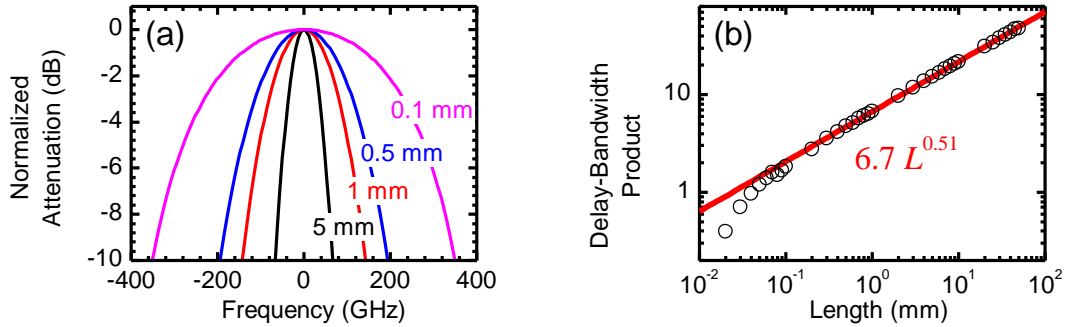


Figure 2.5(a). The normalized attenuation as a function of frequency for several different device lengths. As the length increases, the transmission bandwidth narrows, demonstrating the cascaded filter effect. Figure 2.5(b). Delay – bandwidth product vs. device length, as calculated numerically from the curves in (a). The red line is a linear fit on the log-log plot, demonstrating a square root dependence.

Figure 2.6(a) plots the maximum bit rate which can be transmitted, subject to a specified power penalty, as a function of DBP. These results were calculated using the simulation outlined on Figure 2.3(b). The DBP is increased by increasing  $L$ . At higher power penalties, larger bit rates are permissible for the same size device. For a specified penalty limit, there is a tradeoff between signal bandwidth and the maximum possible storage. This trade-off is predicted by Eq. (2.8); the DBP goes as  $\sqrt{L}$ , the bandwidth goes as  $L^{-1/2}$ , thus the storage – bit rate product (SBP) is a constant. Figure 2.6(b) plots the SBP versus device length for a 3 dB penalty limit. The SBP deviates from a constant value at small  $L$ , where the maximum bandwidth is independent of  $L$  is instead determined by the shape of the absorption dip.

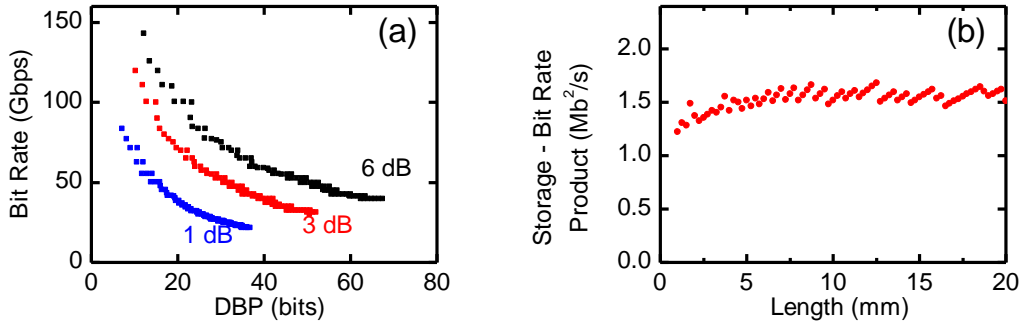


Figure 2.6(a). Maximum bit rate achievable, subject to a specified power penalty limit, as a function of DBP (device length). Penalty limits are 1 dB (blue), 3 dB (red) and 6 dB (black). Figure 2.6(b). Storage – bit rate product (SBP) vs. device length for a power penalty of 3 dB. SBP is another metric for slow light systems which reflects that there is a trade-off between the maximum DBP and the signal bandwidth.

There is an upper limit on the maximum DBP which can be obtained by increasing the size of the device. This upper limit is inversely proportional to the bandwidth, and the proportionality constant, the SBP, is a new performance metric. This metric is useful because the effects of other device parameters upon maximum DBP, such as pump power, dephasing rates, etc., only need to be explored at a single bandwidth. Just as DBP expresses the maximum bandwidth for a given delay, SBP expresses the maximum storage at a given bandwidth.

Finally, it should be noted that the SBP is proportional to the delay but depends on the square of the bandwidth. This suggests that the width of a spectral feature  $\Delta\omega$  is more important than a large  $\Delta\alpha$  and  $\Delta n$ . However, the group velocity decreases with increasing spectral width and the delay per unit length of device, the storage density [21], decreases. The benefit of having a slow light device is lost as the device ceases to be compact. This represents one final trade-off between maximum storage and storage density.

### 2.3 (001) and (110) QW, spin dephasing

The biggest obstacle to realizing EIT in semiconductor QD remains the inhomogeneity of the QD population [24]. To date, EIT-type slow light has not been observed in QD systems. Semiconductor quantum wells (QW) are a much more well-understood type of device structure. The 2D confinement allows the exciton absorption peaks to play a significant role in the optical response of the material even at room temperature [29]. However, EIT depends critically on the robustness of the non-radiative coherence  $\sigma_{31}$ . Prior work has relied upon exciton spin coherence [30], biexciton two-photon coherence [31], and intervalence band coherence [32]. All of these coherences are vulnerable to carrier-carrier and carrier-phonon scattering and have only been observed at low temperatures. We will instead focus on an EIT system centered on the electron spin coherence [35,34,33], which is potentially much more robust [38,37,36]

Three sub-bands play a role in the dipole-allowed transitions at the band edge of a (001) GaAs QW: the conduction band (CB), the heavy hole (HH) band, and the light hole (LH) band. All three bands are doubly degenerate due to the spin degree of freedom. The states in the conduction band have *s*-like symmetry and can be labeled either spin up or spin down. Due to spin-orbit coupling, the valence band (VB) states are labeled with the total angular momentum component  $J_z$ ; the LH states are  $J_z = \pm 1/2$  while the HH states are  $J_z = \pm 3/2$ . The split-off levels are not considered here. A schematic of these states and the dipole-allowed transitions is shown on Figure 2.7(a). The VB and CB states are coupled either by circularly polarized light (red and blue solid lines) or linearly polarized in the growth direction (purple dotted lines). Figure 2.7(b) shows the

orientation of the fields relative to the QW. The crossed transitions are accessed by light that is left- and right-hand circularly polarized along the growth direction ( $z$ -axis). Accessing the vertical transitions requires light that is linearly polarized along the  $z$ -axis. To accomplish this, the QW sits in a waveguide and the light propagates along the  $x$ -direction, in the plane of the QW. The two linear polarization states used as a basis for the waveguide modes are labeled TE (green) and TM (purple), where the TM-mode is polarized along the  $z$ -direction and therefore accesses the vertical transitions. Finally, because the wavelength of the light is much larger than the excitons and because we are using the dipole approximation, the propagation direction of the light is not important in the selection rules; the circularly polarized light need not be normally incident on the QW. Instead the field of the TE polarized waveguide mode can drive these transitions, as linear polarization along the  $y$ -axis can be decomposed into  $\sigma^+$  and  $\sigma^-$ .

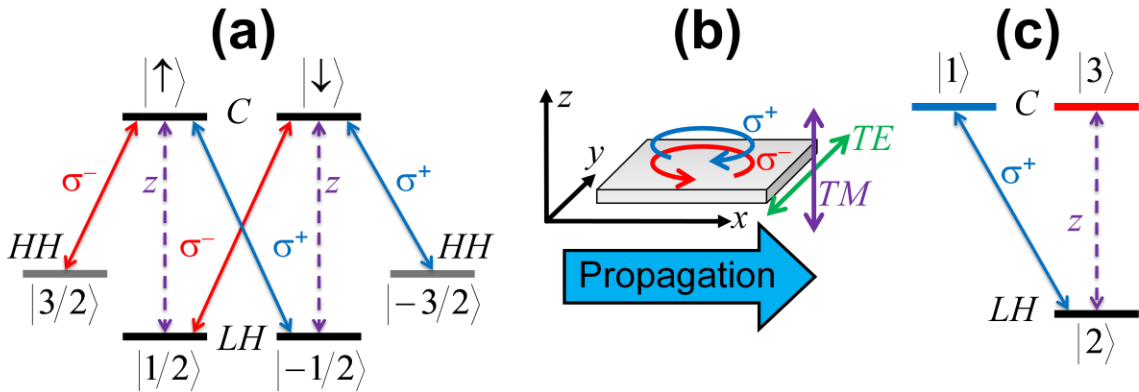


Figure 2.7(a). Schematic of energy levels and dipole-allowed transitions at the  $\Gamma$ -point. The valence band states are labeled with  $J_z$ , the conduction band states are labeled with the spin. The transitions are labeled with the optical field polarization. Figure 2.7(b). Definition of coordinate frame and optical field polarizations relative to QW (gray box). Colors match to those in (a). Light propagates in the  $x$ -direction in either the TM polarization (purple), perpendicular to the growth plane, or the TE polarization (green). The TE-polarized light can be decomposed into two circular components (red and blue). Thus the TM-polarized light is linked to the vertical LH to CB transitions in (a) and the TE-polarized light is linked to the crossed LH to CB transitions. Figure 2.7(c). Three levels from (a) which form a V-type EIT system: one LH level and both conduction band levels. The levels are labeled and colored as in Figure 2.1. There are two such systems present in (a), forming a “double-V” system. The HH levels are not part of the EIT scheme.

Figure 2.7(c) clarifies how the levels and selection rules shown in Figure 2.7(a) form a “double-V” EIT system [34,35]. The states are labeled as in Figure 2.1. The transitions from a single LH state to both of the CB states are the pump and signal, while the non-radiative coherence is between CB states of the opposite spin. Therefore, the crucial parameter  $\gamma_{31}$  is inversely proportional to the spin coherence lifetime. In an ideal EIT system,  $\gamma_{31} \rightarrow 0$ .

Conversely, EIT also provides a method to optically measure the spin coherence lifetime without use of spin precession [33]. Earlier methods of measuring spin coherence were time-resolved techniques involving ultrafast circularly polarized pulses. Spin-polarized populations are optically generated. An external or internal magnetic field is oriented perpendicular to the spin axis and the precession is calculated from the oscillation of the spin polarization along the spin axis [38]. Using the EIT resonance

outlined above, a spin coherence can be optically generated and detected by observing the absorption dip experienced by the signal beam. Measurements by Sarkar et. al. [33] on (001) GaAs QW reveal a dephasing rate of  $\gamma_{31}/2\pi$  of 1 GHz, i.e. a spin coherence lifetime of 1 ns, at temperature of 20 K. The absorption dip due to EIT was observed to persist up to 50 K, where the lifetime dropped to 0.3 ns.

There are three primary relaxation mechanisms for spin-polarized carriers in a semiconductor: Bir-Aronov-Pikus (BAP), Eliot-Yafet (EY) and D'Yakonov-Perel (DP) [36,39]. The dominant spin dephasing mechanism in (001) GaAs QW is the D'Yakonov-Perel effect [37]. The DP effect has its origins in the lack of inversion symmetry in GaAs. This allows terms in the Hamiltonian which are proportional to  $k^3$ . Such terms resemble a magnetic field and cause spin-orbit coupling. The orientation of this field is  $\bar{k}$ -dependent, so as the electron is scattered it experiences different "magnetic fields" and precesses about different axes. However, in (110) QW this mechanism is suppressed. The electron still feels an effective magnetic field, but for all in-plane  $\bar{k}$  the field is oriented along the same direction, parallel to the growth axis. The entire spin population precesses about the same "field" coherently. Prior experiments have demonstrated spin relaxation times above 1 ns at room temperature [38,37]. The use of (110) QW offers the hope that the EIT resonance observed in [33] can be extended to room temperature.

The EIT scheme we will be investigating for (110) QW resembles the double-V of the (001) QW which we have presented above. A detailed theoretical treatment of the similarities and differences was carried out by Chang et. al. [34]. The primary difference

is a mixing between HH and LH bands. However, two LH-like states still couple to the CB states with similar selection rules, albeit with slightly elliptical polarizations as opposed to circular and linear.

The structure of our sample consists of a (110) GaAs substrate, 1.18  $\mu\text{m}$  of  $\text{Al}_{.29}\text{Ga}_{.71}\text{As}$  (WG cladding), 0.17  $\mu\text{m}$  of  $\text{Al}_{.15}\text{Ga}_{.85}\text{As}$  (WG core), 0.40  $\mu\text{m}$  of  $\text{Al}_{.30}\text{Ga}_{.70}\text{As}$  (WG cladding), and a 20 nm GaAs cap. A 13 nm GaAs layer embedded within the top cladding layer located 60 nm above the edge of the WG core forms a single QW. The quality of the growth is quite good; the photoluminescence (PL) linewidth is very narrow, approximate 2 meV at 10 K. Note that the small size of the core means that the fundamental mode of the WG extends far into both cladding layers; the quantum well is only slightly offset from the peak of the mode. The samples are cleaved and approximately 150  $\mu\text{m}$ . No lateral confinement mechanism is used.

Figure 2.8 shows the experimental setup for measuring the EIT-induced absorption dip, based on the techniques described in [33]. The pump laser is a CW Ti:Sapphire ring laser, the signal is an external cavity single mode diode laser. Beam samples from each laser are beaten together on a fast detector and the signal measured on an RF spectrum analyzer. This allows the tuning between the two lasers to be controlled to within tens of MHz. The beams are mechanically chopped at kilohertz frequencies  $f_1$  and  $f_2$ . A lock-in amplifier detects the signal at  $f_1 - f_2$ , which is proportional to the difference in transmission between the pump on and pump off. Two half wave plates cross-polarize the pump and signal as per the selection rules described above. An additional advantage of the cross-polarized beams is that the pump can then be filtered at the output with a

polarizer. The beams are coupled into and out of the sample WG with microscope objectives. The sample sits in a continuous flow liquid helium cryostat and our initial measurements are made at low temperature.

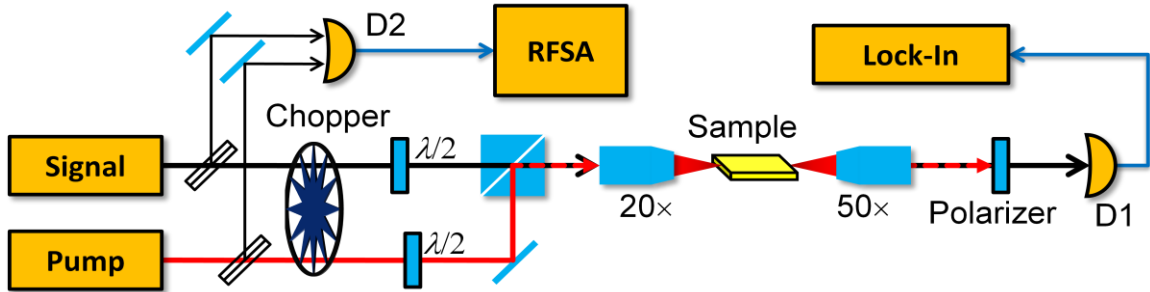


Figure 2.8. Experimental setup for measuring the EIT-induced absorption dip. Light from the pump laser is shown in red, the signal is shown in black, and electrical connections are dark blue. The pump is a single mode CW Ti:Sapphire ring laser, the signal is a single mode external cavity tunable diode laser. Small amounts of both beams are split off and incident on a fast detector (D2) which feeds into an RF spectrum analyzer (RFSA), allowing the pump-signal detuning to be controlled to within tens of MHz. The pump and signal are mechanically chopped at different frequencies, allowing high-precision lock-in detection of the differential transmission. Half wave plates cross-polarize the pump and signal, allowing the pump beam to be filtered by a polarizer at the output.

An example of the EIT-induced dip in absorption is shown in Figure 2.9(a), taken at 10 K. For these experiments, the pump is TM-polarized while the signal is TE. The lasers are tuned near the center of the LH absorption peak. The change in transmission  $\Delta T/T$  is plotted as a function of pump-signal detuning. For small changes in absorption,  $\Delta\alpha L \cong \Delta T/T$ . At large detuning, there is a broad “background” change in absorption due to effects such as band-filling and saturation. The EIT signature is the narrow 600 MHz (FWHM) peak in transmission at zero detuning. The depth of this absorption dip is approximately 3%.

Due to the elliptically polarized nature of the selection rules, it is necessary to verify that this resonance is related to spin coherence and not due to population oscillations, discussed in Section 3. This is done by adding a magnetic field parallel to the growth

direction, which changes the states at the band-edge as shown in Figure 2.9(b). The degeneracy of the CB spin states is lifted and the double-V system is split into two V-type EIT systems. Consequently, two absorption dips are now observed, as seen in Figure 2.9(c). Note that EIT condition occurs at two-photon resonance, in our V-system this means the detunings of the signal and pump from their respective transitions are equal (this is slightly different than the ladder system discussed earlier, where the resonance occurs at  $\delta_s = -\delta_p$ ). Thus, the splitting in the peaks shown on Figure 2.9(c) is twice the splitting of the states.

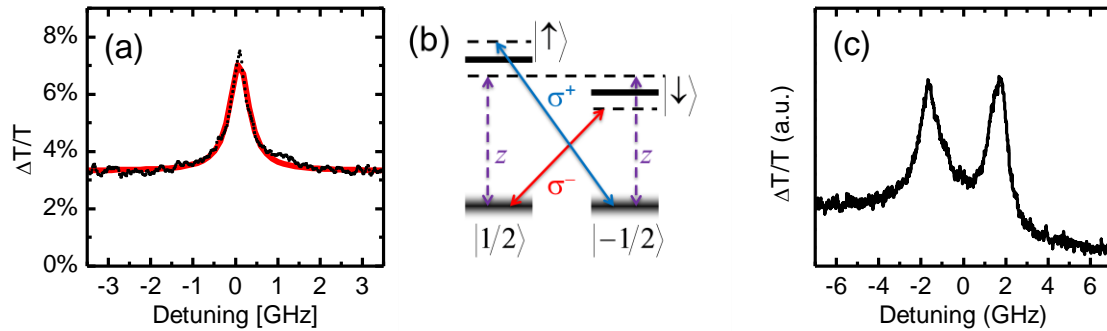


Figure 2.9(a). Change in transmission as a function of pump-signal detuning. Red line is a Lorentzian fit. Figure 2.9(b). EIT levels after a magnetic field has been applied along the growth direction ( $z$ -axis). The field lifts the degeneracy of the CB spin states, dividing the double-V system into two V-type systems. Figure 2.9(c). Change in transmission in the presence of the magnetic field. The splitting of the transmission peak confirms the origin of the resonance in the spin coherence.

Figure 2.10 shows a study of the temperature dependence of the EIT resonance. Figure 2.10(a) shows the transmission peaks at various temperatures. No substantial reduction in peak size is measured, but the signal to noise ratio decreases with increasing temperature. This is due to mechanical instabilities in the continuous flow cryostat. Above 50 K the amount of thermal drift makes collecting a trace a matter of luck, above 100 K no resonance could be observed. The largest  $\Delta\alpha L$  measured was 10% at 40 K and 8 mW of pump power. By Eq. (1.21), this also implies a potential DBP on the

order of 0.1. The temperature dependence of the electron spin coherence is summarized in Figure 2.10(b). We observe a roughly constant coherence lifetime of 0.5 ns from 4 K to 100 K. However, there is substantial variability of the measured coherence time from spot to spot on the sample. Another possible complication is that the slow drift of the cold finger of the cryostat might result in changes of the coupling efficiency of the pump with the quantum well.

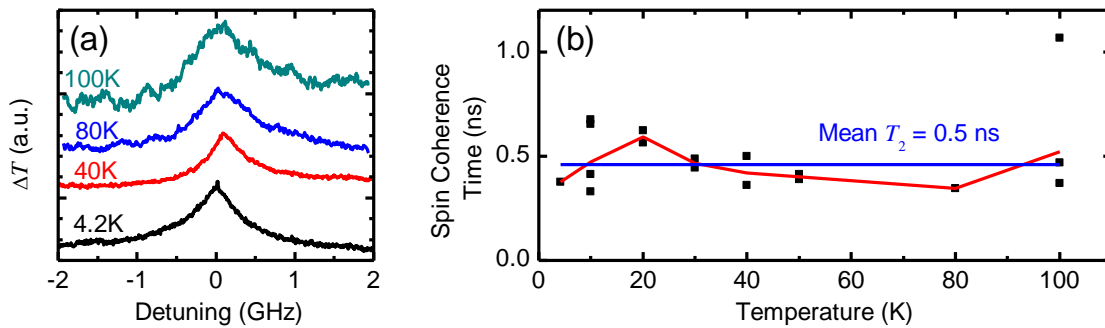


Figure 2.10(a). Change in transmission  $\Delta T$  vs. pump-signal detuning at various temperatures, offset is for clarity. The signal to noise ratio is decreasing at increasing temperatures due to mechanical instability in the cryostat. Figure 2.10(b). Spin coherence time as a function of temperature at 2.5 mW pump power. Data points are black squares, red line represents the average value at each temperature, blue line is the mean value at all temperatures (0.5 ns).

## 2.4 Summary

We have presented work on two possible routes by which EIT may come to be realized in semiconductors. First, we have simulated the performance of a QD-based EIT slow light device in an optical communication link. Though the simulation was based on EIT, the results are quite general and are applicable to slow light systems where the linear response to the signal may be approximated as a Lorentzian transmission spectrum. Our analysis of the BER of the link quantifies distortion in terms of power penalty and presents a trade-off between bit-rate and maximum length. From this we advance a new performance metric for such slow light devices: the storage – bit rate

product. For large storage the spectral bandwidth  $\Delta\omega$  must be much larger than the signal bandwidth.

We also examine spin coherence as the foundation for a second approach to EIT in semiconductors. We present the first measurements of EIT resonance due to spin coherence in (110) QW. This is an important first step in bringing such an EIT scheme up to room temperature. Spin coherence lifetime does not exceed 1 ns as the spin lifetime does, but does seem to remain constant as temperature is increased to 100 K.

### 3 Coherent Population Oscillations

The rapid decoherence of optical excitations in semiconductors greatly multiplies the difficulty of achieving large changes in group velocity as reported in atomic systems. As mentioned in the previous section, advances of atom-like semiconductor nanostructures such as quantum dots (QDs) may enable the realization of large group index, but due to problems with inhomogeneity experimental demonstration is still lacking. By focusing on more robust coherences such as electron spin coherence, we have shown that it is possible to reproduce EIT in quantum wells, but there are currently no experimental results demonstrating that this effect can persist to room temperature.

In 2003, Bigelow et. al. [40] first reported the use of coherent population oscillation (CPO) in ruby to produce room temperature slow light. Like EIT, CPO also uses a strong pump beam to create a narrow spectral window in a homogenous absorption line, which then creates a slow light dispersion for a weak signal beam. Unlike EIT, CPO does not involve any exotic or potentially fragile quantum coherences, depending only on

the lifetime of a population grating induced two coherent beams. In a high quality quantum well (QW) structure at low temperatures this lifetime has been shown to be around 1 ns [41] (as measured with nondegenerate four wave mixing, closely related to the CPO effect discussed here). We will begin this section with a quick background of the physical processes. We will then show experimental observation of CPO in GaAs/AlGaAs QW, CPO in a QW waveguide, time-domain measurements of the delay of a modulation, and demonstration of the CPO effect at room temperature.

### 3.1 Population Oscillations and Temporal Gratings

A complete, quantitative derivation of the CPO effect in semiconductors is given by Ku in [24], an outline of the approximations and techniques used will be given here. First, the density matrix formalism is used to treat the evolution of a two level system interacting with two coherent, co-polarized optical fields under the dipole and rotating wave approximations. One field, called the pump, is strong enough to saturate the medium, while the other, called the signal is much weaker and may be treated as a perturbation. Under this approximation, the two relevant material parameters, inversion and coherence, can be solved exactly for the pump in a steady state condition by simply neglecting the signal. The effect of the signal on the material is then calculated to first order. The pump and signal beat together, creating a small sinusoidal modulation of the optical intensity at the pump/signal detuning  $\delta \equiv \omega_s - \omega_p$ . If  $\delta$  is smaller than the decay rate of the inversion  $(T_1)^{-1}$ , then the population inversion also obtains a small coherent oscillation at frequency  $\delta$ . This oscillation in turn affects the coherence, allowing the pump at  $\omega_p$  to contribute to the susceptibility at  $\omega_s$ . The coherence

generated by the pump at  $\omega_s$  has a different phase than that generated by the signal, and therefore interferes destructively, reducing the absorption experienced by the signal. Physically, the oscillation of the population inversion acts as a “temporal grating” which scatters energy from the pump frequency to the probe frequency and effectively increases the transmission of the probe. Again, this CPO-induced reduction in absorption is only present for small detuning:  $\delta < (T_1)^{-1}$ .

Using a further approximation that the coherence dephasing time  $T_2$  is short enough that  $T_2 \ll T_1$  and  $T_2 \ll \Omega_p^{-1}$ , the absorption  $\alpha$ , index  $n$ , and group index  $n_g$  experienced by the signal are

$$\alpha(\omega_s) = \frac{\alpha_0}{1 + I_0} \left( 1 - \frac{I_0(1 + I_0)}{(\delta T_1')^2 + (1 + I_0)^2} \right) \quad 3.1$$

$$n(\omega_s) = n_{bac} + \frac{c\alpha_0}{2\omega_s} \cdot \frac{I_0}{1 + I_0} \cdot \frac{\delta T_1'}{(\delta T_1')^2 + (1 + I_0)^2} \quad 3.2$$

$$n_g(\omega_s) = n_{bac} + \frac{c\alpha_0 T_1}{2} \cdot \frac{I_0}{1 + I_0} \left( 1 + \frac{(1 + I_0)^2 - (\delta T_1')^2}{[(\delta T_1')^2 + (1 + I_0)^2]^2} \right) \quad 3.3$$

where  $\alpha_0$  is the unsaturated absorption of the 1→2 transition and  $n_{bac}$  is the background refractive index. The pump parameter  $I_0$  is given by

$$I_0 = \left| \frac{\mu E_p}{\hbar} \right|^2 \cdot T_1 T_2 \quad 3.4$$

where  $\mu$  is the dipole moment of the 1→2 transition for the pump beam. The derivation sketched above also neglect a wave-mixing term that generates a polarization at  $2\omega_p - \omega_s$ . In an absorber, this “conjugate” wave can be neglected as long as a wave is

not specifically injected at this frequency. We will return to the subject of the conjugate wave in Section 4.

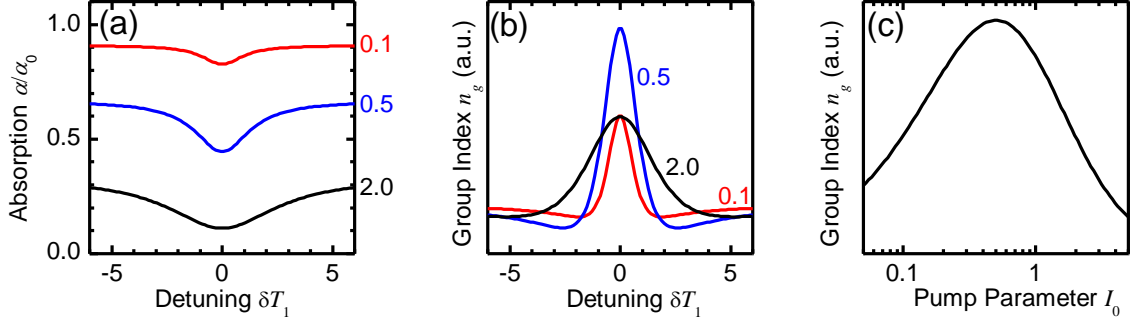


**Figure 3.1(a).** Absorption of signal, normalized to unsaturated background absorption, as a function of pump – signal detuning for different values of the pump parameter  $I_0$  (shown on right). When  $I_0 \ll 1$ , the hole deepens with increasing  $I_0$  but the FWHM is determined only by  $T_1$  and remains constant. When  $I_0 \gg 1$  the depth of the hole saturates and the FWHM increases with increasing  $I_0$ . **Figure 3.1(b).** Group index vs. detuning for different  $I_0$ , showing maximum  $n_g$  and minimum GVD at  $\delta = 0$ . **Figure 3.1(c).** Group index vs.  $I_0$  at  $\delta = 0$ . Maximum  $n_g$  occurs at  $I_0 = 0.5$ , when the hole is deepest but power broadening has not yet begun.

Figure 3.1 shows the qualitative features of the signal absorption and group index produced by CPO. Figure 3.1(a) is the absorption spectrum at three different values of  $I_0$ . Simple saturation of the transition causes a reduction in the absorption at large  $\delta$  (the “background”) as  $I_0$  is increased. The CPO-induced change in absorption is the spectrally narrow hole near  $\delta = 0$ . For  $I_0 \ll 1$ , the width of the hole depends only on  $T_1$  while the depth scales linearly with  $I_0$ . As  $I_0$  is increased the depth of the hole saturates and the width becomes proportional  $I_0$ . It should be emphasized that this dip forms in a *homogeneously* broadened absorption line, this effect is physically distinct from the phenomenon of spectral hole burning (SHB) in an inhomogeneously broadened absorption peak. The width of an SHB dip depends on the dephasing time  $T_2$ , typically on the order of 100 fs in semiconductors, while the width of the CPO resonance depends on  $T_1$ , which can be on the order of a nanosecond. The narrowness of the dip

allows low group velocity to be achieved. Also, the dependence of the CPO broadening upon  $I_0$  is linear, whereas the broadening of the SHB dip goes as  $\sqrt{I_0}$ .

From the discussions in Section 1, we immediately expect that the narrow spectral dip is accompanied by a slow light dispersion. Figure 3.1(b) shows the functional dependence of the group index  $n_g$  on the detuning for the same three values of  $I_0$  in (a). At zero detuning the group index is maximum and the group velocity dispersion (GVD) is minimum. When  $I_0 \gg 1$  the second order GVD decreases with increasing  $I_0$ .

Figure 3.1(c) plots  $n_g$  at  $\delta = 0$  as a function of  $I_0$  at  $\delta = 0$  (see Eq. (3.3)). Maximal slowdown is achieved when  $I_0 = 0.5$ , when the hole is deepest. The group index gradually decreases as  $I_0$  is increased past this point as the spectral hole broadens without deepening. This is significant because in a real device  $I_0$  will decrease exponentially with propagation distance as the pump is absorbed, meaning that  $n_g$  will be maximized at only one point along the device. This is in contrast to EIT systems, which can be arranged such that neither pump nor signal are absorbed. Finally, one should note that there is a trade-off between spectral width and  $n_g$  for  $I_0 \gtrsim 1$ . As discussed in Section 2.2, for long devices (and long delays) the *bandwidth* is much smaller than the spectral width. Therefore, depending on system design specifications,  $I_0 = 0.5$  might not be the optimum operating condition.

### 3.2 Experiments on QW

We now present the results of our investigations of the CPO effect in semiconductor quantum wells (QW). Two basic experimental geometries will be examined: a normal incidence geometry where the pump and signal are pass through several quantum wells

while propagating roughly parallel to the growth direction, and a waveguide geometry where the pump and signal propagate in the plane of a single QW. We will focus most of our attention on the heavy hole exciton absorption peak as these transitions are the most similar to the idealized two level system outlined above. At low temperatures, the population oscillations will consist of pulsations in the exciton density and the width of the CPO peak will be determined by the lifetime of these pulsations. At room temperature the excitons thermalize almost immediately into an electron-hole plasma, however we shall see that it is the much longer radiative recombination lifetime of the plasma which determines the spectral width of the CPO absorption dip, and it is still possible to obtain a narrow dip and large group index.

### 3.2.1 (001), Surface Normal, Absorption and MZI

In our first experiments investigating CPO in semiconductors [42], the pump and the signal are nearly normally incident upon our sample, intersecting within the sample at a small angle  $\Delta\theta$  with respect to each other. This geometry simplifies the experiment by spatially separating the pump and the signal at the output (recall that the pump and signal must have parallel polarizations). However, this configuration slightly changes the physical process. In addition to the temporal modulation, the population pulsation also has a spatial pattern with a radial frequency  $K = 4\pi \sin(\Delta\theta/2) / \lambda$ , where  $\lambda$  denotes the optical wavelength in the sample. As  $K$  increases the diffusion becomes more effective at “washing out” the population grating. Hence, the lifetime  $T_1$  must be modified such that  $(T_1')^{-1} = (T_{1,rad})^{-1} + D \cdot K$ , where  $D$  is the exciton diffusion coefficient and  $T_{1,rad}$  is the radiative recombination lifetime [41]. Finally, the saturation of the

transition is much for complicated in semiconductors due to many body effects.

Therefore, Eq. (3.4) must also be modified such that

$$I_0 = \frac{I_{pump}}{I_{sat}} \quad 3.5$$

where  $I_{pump}$  is the pump intensity and  $I_{sat}$  is a phenomenological parameter.

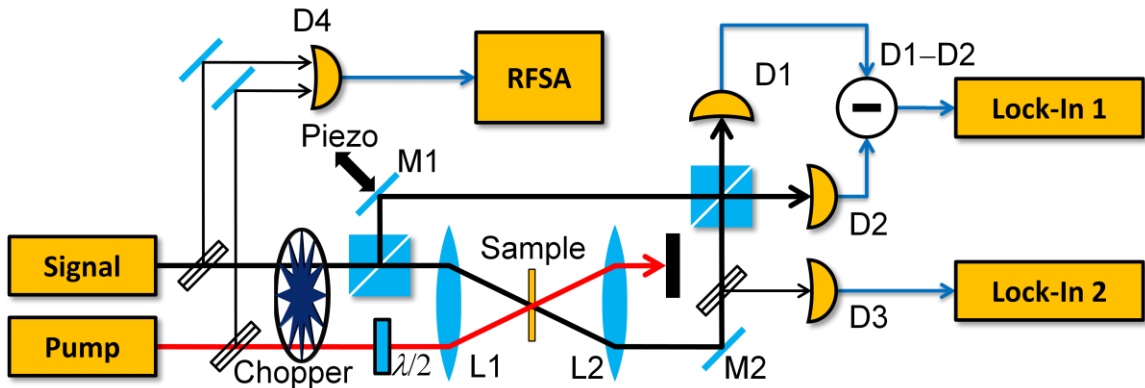


Figure 3.2. Experimental setup for measuring transmission and refractive index associated with CPO. Light from the pump laser is shown in red, the signal is shown in black, and electrical connections are dark blue. The pump is a single mode CW Ti:Sapphire ring laser, the signal is a single mode external cavity tunable diode laser. Small amounts of both beams are split off and incident on a fast detector (D4) which feeds into an RF spectrum analyzer (RFSA), allowing the pump-signal detuning to be controlled to within tens of MHz. As the signal frequency is swept, the transmission is measured by detector D3 and the dispersion is measured by an interferometer composed of M1, M2, the two beam splitters, and D1 and D2. The signal beam is mechanically chopped so that sensitive lock-in detection techniques can be used.

Figure 3.2 shows the experimental setup. The basic concept is that the pump and signal are focused onto the same spot on the sample, the signal frequency is swept, and the absorption and refractive index experienced by the signal are measured as a function of pump-signal detuning  $\delta$ . The pump is a tunable, single-mode CW Ti:Sapphire laser. We fix the pump wavelength at the exciton absorption peak of the heavy-hole transition. The signal is a tunable, single-mode, external cavity diode laser. The polarization angle between the beams is adjusted via a half-wave plate in the pump path such that both beams are linearly polarized along the same direction, as required

to observe CPO. Sampled beams from both lasers are coincident on a fast ( $> 40$  GHz) detector D4, which is then connected to an RF spectrum analyzer (RFSA). This allows the pump-signal detuning to be set with an accuracy of tens of MHz. The pump and signal are then mechanically chopped at two different frequencies  $f_1$  and  $f_2$  so that sensitive lock-in detection can be employed after the sample. Differential transmission is measured by locking to the difference frequency  $f_1 - f_2$ . The pump and signal are incident on different regions of the lens L1, creating an angle  $\Delta\theta$  between the beams as they are focused onto the sample. This angular separation allows the pump to be easily blocked after the sample.

The method of measuring absorption and refractive index are based on that used in [43]. The transmission of at the signal wavelength is proportional to the signal measured by detector D3. Estimates of absorption are made by normalizing the intensity measured by D3 to a single measurement made with signal beam detuned past the lower energy edge of the heavy-hole resonance, where the sample should be essentially transparent. The refractive index is measured by the Mach-Zehnder interferometer formed by M1, M2, the two cube beam splitters, and the balanced pair of detectors D1 and D2. A piezoelectric actuator on M1 allows the path lengths in the two arms to be precisely matched. The difference signal is then

$$\Delta I \propto e^{-\alpha(\omega)L} \cdot \cos[\omega L/c \cdot n(\omega)] \quad 3.6$$

where  $\alpha(\omega)$  is the absorption and  $n(\omega)$  is the refractive index. The signal from D3 can be used to eliminate the exponential term, allowing (3.6) to be solved for  $n$ .

The sample sits in a liquid helium cryostat held near 10 K. It is a multiple-quantum well (MQW) structure consisting of 15 GaAs(135Å)/Al<sub>0.3</sub>Ga<sub>0.7</sub>As(150 Å) QWs grown by molecular beam epitaxy (MBE) on a (001) GaAs substrate. After growth, the substrate of the sample is polished down to a thickness of approximately 100 μm and the sample is mounted on a sapphire disk for good thermal conductivity.

Figure 3.3(a) shows absorption spectra as a function of detuning for various values of pump intensity. The absorption  $\alpha L$  is defined by  $I_{out} = I_{in} \exp(-\alpha L)$ , where  $L$  is the thickness of the 15 quantum wells. The sample is kept at a temperature of 10 K. The pump is tuned to the HH exciton resonance. As the pump power is increased, the overall absorption decreases due to saturation of the HH resonance. Many-body effects such as a blue shift due to exchange repulsion and a broadening of the absorption resonance due to excitation induced dephasing [44] are also observed and contribute to the  $\Delta\alpha L$  at large detuning. There is also a sharp dip in absorption centered at zero detuning which increases in depth with increasing pump intensity. This narrow dip is the result of CPO between the pump and the signal.

Several qualities of this dip point toward its origins in CPO. The spectral width of the dip is much smaller than the exciton homogeneous linewidth, indicating that this is not due to spectral hole burning. Also, the spectral width of the dip depends on the relative angle between the pump and signal, reflecting effects of exciton spatial diffusion. At low excitation levels, the linewidth of the dip corresponds to a grating lifetime of 0.51 ns and 0.33 ns for  $\Delta\theta = 2.5^\circ$  and  $5^\circ$ , respectively which are quantitatively consistent with previous FWM study for delocalized excitons [45].

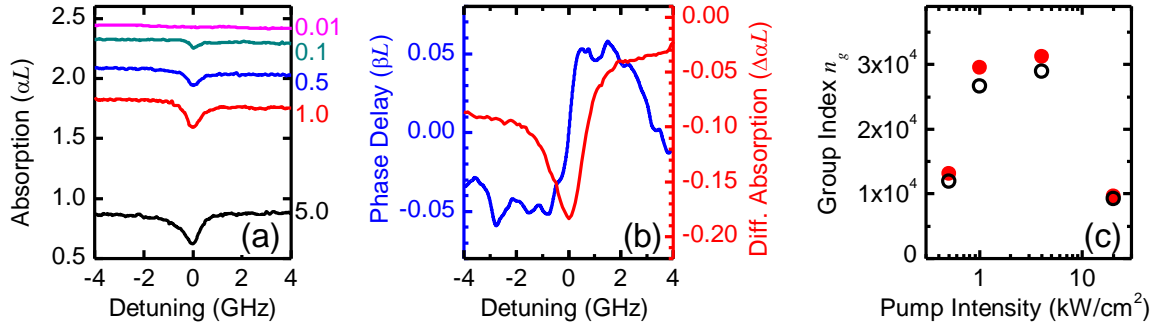


**Figure 3.3(a).** Signal absorption vs. detuning for various pump intensities (labeled in kW/cm). As pump power is increased, the background absorption decreases due to saturation and the CPO-induced dip also deepens. **Figure 3.3(b).** Phase delay (blue), proportional to refractive index, and change in absorption (red) vs. detuning. The rapid change in index at zero detuning results in slow light. **Figure 3.3(c).** Group index as a function of pump intensity as calculated directly from the index dispersion (red dots) and estimated from the absorption via Kramers-Kronig relations (black circles). The two measurements match well, confirming that the simpler absorption measurements can be used to estimate delay as opposed to more complicated measurements of refractive index. Also seen is the rise, peak, and fall of  $n_g$  as pump intensity is increased, which is as expected by theory.

Figure 3.3(b) shows the results from the Mach-Zehnder interferometer for a pump intensity of 1 kW/cm<sup>2</sup>. Phase delay, proportional to refractive index, and change in absorption are plotted as functions of pump-signal detuning. The group index at zero detuning is inversely proportional to the slope of the phase delay; at this pump power  $n_g = 31,200$ , corresponding to a group velocity of only 9,600 km/s. The linear region of the dispersion is about 1.5 GHz, although at higher pump intensities the FWHM of the gain dip broadened to 2 GHz. This is a 100-fold increase over the previous record bandwidth of 15 MHz reported with EIT-like Raman resonance in solid hydrogen [46] and 16 million times larger than that of the original CPO slow light in ruby [40].

Group index as a function of pump intensity is plotted on Figure 3.3(c) (red dots). The plot is qualitatively similar to the behavior predicted by Eq. (3.3) (see Figure 3.1(b)), increasing, peaking, and then decreasing with pump intensity. Additionally, we can estimate the group index from the absorption dip alone, assuming a Lorentzian hole and using Eq. (1.21). These estimates are also plotted on Figure 3.3(c) (black circles) and are

in good agreement with the directly measured values. The agreement is significant because the absorption dip can be measured with greater accuracy and a simpler experimental setup than the phase delay.

Note that  $I_{sat}$  in Eq. (3.5) depends on the relative angle  $\Delta\theta$  between the pump and signal because the decay rate of the population grating due to spatial diffusion of the excitons increases as  $\Delta\theta$  is increased. From Eq. (3.1) we find that the depth of the hole should be

$$\Delta\alpha = \frac{\alpha_0 I_0}{(1 + I_0)^2} \quad 3.7$$

The saturation intensity  $I_{sat}$  is obtained from a numerical fit of Eq. (3.7) to the depth of the absorption dip vs. pump intensity; and is 2.5 kW/cm<sup>2</sup> and 1.6 kW/cm<sup>2</sup> for  $\Delta\theta = 2.5^\circ$  and  $5^\circ$ , respectively.

### 3.2.2 (001), Surface Normal, Time Domain Measurements

We now turn to time-domain measurements of the CPO effect. This was the technique used in [40], where a single laser produces both the pump and signal beam. Our experimental setup is shown in Figure 3.4. The beam from a single CW Ti:Sapphire laser at optical frequency  $\omega_0$  passes through an electro-optic modulator and is subjected to a sinusoidal amplitude modulation at RF frequency  $\delta$ . The fundamental component at  $\omega_0$  acts as the pump while the side bands at  $\omega_0 \pm \delta$  act as the signal. The pump-signal detuning can be adjusted simply by changing the RF frequency  $\delta$ . This alleviates the difficulties of keeping two lasers tuned within tens of MHz of each other

as well as difficulties mode-matching the two beams. The modulation depth is approximately 5%.

The pump/signal is focused onto the sample in a surface-normal geometry by a 20× microscope objective, collected and collimated and directed onto detector D1. The modulation is measured by an oscilloscope. A reference trace is measured by tuning  $\omega_0$  below the heavy-hole transition, into the bandgap. When  $\omega_0$  is tuned back up into the HH transition, the CPO effect causes a delay which is measured on the scope as a phase shift of the modulation. This delay is then measured for different pump powers and different values of detuning.

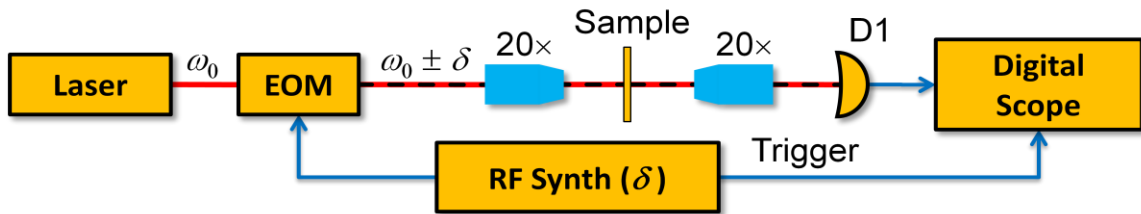


**Figure 3.4. Experimental setup for time-domain measurements.** A single laser at frequency  $\omega_0$  is amplitude modulated at RF frequency  $\delta$ . The fundamental component acts as a pump while the side bands at  $\omega_0 \pm \delta$  serve as the signal. The light is focused with a microscope objective onto the sample, collected, and collimated onto a detector. The modulation is measured by an oscilloscope. A reference trace is taken by tuning  $\omega_0$  below the HH resonance. When the laser is tuned back to the HH transition a delay due to CPO is measured as a phase shift of the RF modulation. Delay is measured as a function of pump power and detuning  $\delta$ .

The sample is the same as that used in Section 3.2.1, where a group index of 31,200 was inferred from the dispersion and absorption measurements. The time-domain studies presented here are the first direct demonstration of slow light resulting from the CPO response in a QW structure. As above, the experiments were carried out at the peak of the inhomogeneously broadened heavy-hole (HH) exciton absorption resonance.

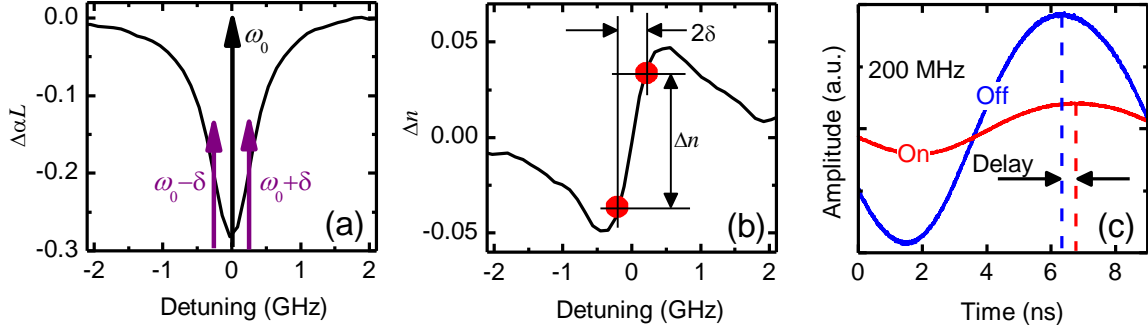


Figure 3.5(a). Change in absorption due to CPO vs. pump-signal detuning as measured by the two-laser setup in Figure 3.2. Overlaid is the spectrum of the modulated beam from the setup in Figure 3.4, consisting of the fundamental component (black) and the side modes (purple). Figure 3.5(b) shows the dispersion as measured by the interferometer in Figure 3.2, the red dots indicate the positions of the modulation side bands. The difference in refractive index leads to a group delay. Figure 3.5(c). Modulation traces when the laser is tuned below the band edge (blue) and on the HH resonant (red). The phase difference between the two is due to the group index described in (b).

Figure 3.5 illustrates in more detail how the single modulated beam can signal the CPO resonance. Figures 3.5(a) and (b) show absorption and index dispersion as measured by the two-laser setup in Figure 3.2. The spectrum of the single laser modulated beam is overlaid on Figure 3.5(a). It consists of the fundamental component (black) and two side-bands (purple). The temporal shift of the sinusoidal modulation is given by

$$\Delta T_{RF} = \frac{\Delta k}{2\delta} L \cong \omega_0 \frac{\Delta n}{\delta} \cdot \frac{L}{c} \equiv n_{mod} \cdot \frac{L}{c} \quad 3.8$$

where  $\Delta n$  is the difference in refractive index between the two side bands (red circles on Figure 3.5(b)) and we have defined the modulation index  $n_{mod}$  in analogy to the group index [40]. Note that  $\Delta T_{RF}$  is slightly different than the group delay  $T_g \equiv c/n_g$  at  $\omega_0$ .  $T_g$  is determined by the group index  $n_g$ , roughly proportional to the slope of the dispersion at  $\omega_0$ , while  $T_{RF}$  is determined by  $n_{mod}$ , which is proportional to the slope of the line connecting the red dots in Figure 3.5(a). In other words,  $T_g$  is a measurement of the index dispersion at  $\omega_0$  while  $\Delta T_{RF}$  is a measurement of the index difference

between two frequencies *near*  $\omega_0$ . As  $\delta \rightarrow 0$ ,  $\Delta T_{RF} \rightarrow T_g$ . Also, for the dispersion of a Lorentzian dip  $n_g \geq n_{mod}$  (see Eq. (1.20) ).

Figure 3.5(c) shows the intensity measured by detector D1 when  $\omega_0$  is tuned off-resonance (blue), below the HH absorption where there is no CPO and  $\Delta n = 0$ , and when it is tuned on-resonance (red), within the HH absorption. The amplitude and time shift change as  $\delta$  is swept and the sidebands map out the absorption and dispersion.

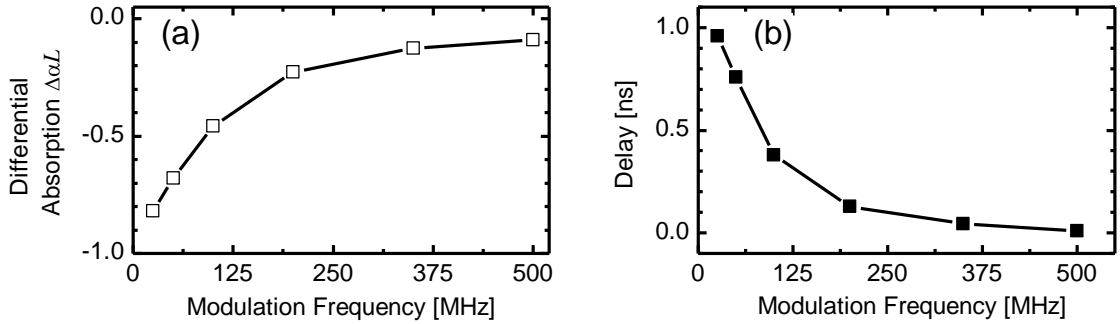


**Figure 3.6(a).** Differential absorption (on-resonance minus off-resonance) as a function of modulation frequency  $\delta/2\pi$  for a pump power of 4 mW. The modulation frequency is equivalent to the detuning. The CPO-induced spectral hole is visible as a reduction of absorption as  $\delta \rightarrow 0$ . The hole is narrower compared with that measured in Figure 3.3(a) because the grating lifetime  $T_1$  no longer has a diffusion term ( $\Delta\theta = 0$ ). **Figure 3.6(b).** Delay of modulation between on- and off-resonance. As shown in Figure 3.1(b) the group index is highest at  $\delta = 0$ .

Figure 3.6(a) shows the differential attenuation and time delay as a function of the modulation frequency  $\delta/2\pi$  with 4 mW of power incident on the sample. The differential absorption is the difference in absorption when  $\omega_0$  is tuned on the HH resonance and when it is tuned below resonance. The minimum as  $\delta \rightarrow 0$  reveals the absorption dip due to CPO. At this intensity the width of the CPO absorption dip is determined only by the HH-exciton lifetime. The half width at half maximum (HWHM) of 120 MHz indicates  $T_1 = 1.3$  ns, which is consistent with previous studies [41]. This value is less than that shown in Figure 3.3(a) because the spatial diffusion which reduces  $T_1$  in

that experiment is inherently absent in the measurement carried out here due to the co-propagating pump and signal  $\Delta\theta = 0$ .

The delay as a function of modulation frequency is shown on Figure 3.6(b). As above, a reference trace is first taken with  $\omega_0$  tuned below the HH exciton resonance, where the propagation of the modulation is not affected by CPO. Then the laser is tuned back into resonance with the HH exciton transition and CPO causes a temporal shift in the modulation. Time delays greater than 1 ns are achieved at  $\delta/2\pi = 25$  MHz. Given the length of the active region  $L = 195$  nm, this time delay implies a velocity of 200 m/s and a modulation index  $n_{mod} \sim 1.5 \times 10^6$ . We emphasize again that the delay defined in Eq. (3.8) and shown on Figure 3.6(b) is a lower bound on the group delay.

The increase in group index over that obtained from the frequency-domain measurements of Section 3.2.1 arises mainly from the absence of exciton spatial diffusion and the perfect mode matching of the signal and pump. This results in a linewidth reduction and, because the spectral area of the CPO resonance is conserved, an increase of the transparency depth by a similar factor. Thus the increase in group index goes as the square of the linewidth reduction factor.

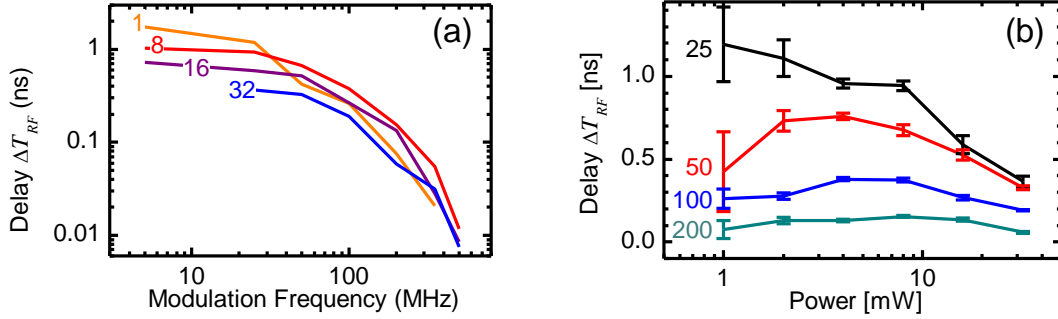


Figure 3.7(a). RF delay vs. modulation frequency for various pump powers (in mW). As the pump power increases, the region of low GVD (constant delay) becomes wider but the maximum delay decreases. Figure 3.7(b). Delay as a function of pump power for various modulation frequencies (in MHz). At most frequencies this curve follows the peaked response observed in Figure 3.3(c). However, at the lowest frequency, 25 MHz, the delay continues to increase with decreasing pump power. This suggests that another easily saturated, even narrower resonance may exist.

Figure 3.7(a) shows  $\Delta T_{RF}$  as a function of modulation frequency for various pump powers, in mW. Low pump powers (1 mW) have the highest delay but also have a high GVD. Even though the spectral width of the absorption is 120 MHz (HWHM), there is still significant GVD at 10 MHz, limiting the bandwidth of a potential signal. At 8 mW, the delay is constant out to 25 MHz and at 32 mW GVD is zero out to 50 MHz. In all cases, the GVD determines a tighter bandwidth than the absorption dip.

Figure 3.7(b) shows the power dependence of  $\Delta T_{RF}$  as a function of modulation frequency. Initially, the delay increases with power as CPO creates a deeper hole and larger  $\Delta n$ . The group index and delay then peaks, as is seen most clearly at 50 MHz detuning, and then rolls off as power is increased further. This power dependence reflects the saturation behavior and power broadening of the CPO absorption dip. At the smallest detuning, 25 MHz, no peak in delay is measured. One problem is that at low frequencies the RF phase shift is more difficult to measure. Combined with the lower signal to noise ratio at low power, this leads to the large error bars in this region. Additionally, it may be possible that an even narrower, easily saturated resonance, such

as population oscillation from impurities, is contributing at small  $\delta$  and small power. Figure 3.7 demonstrates that the delay can be tuned optically, simply by adjusting pump power. It should be emphasized that the power of the signal will not be important, as long as it is low compared with that of the pump.

### 3.2.3 (001), Waveguide, Room Temperature

Observation of CPO-induced slow light propagation at room temperature is complicated by the presence of LO-phonons and thermally excited electron-hole pairs (plasma). Scattering with LO-phonons ionizes the excitons on a picosecond or sub-picosecond time scale. The electron-hole plasma screens the Coulomb interaction and reduces the oscillator strength of the exciton transition. In comparison with the low temperature conditions described in the previous sections, at room temperature the optical depth of the QW ( $\alpha_0 L$ ) is dramatically reduced while the saturation intensity of the excitonic optical nonlinearity is increased [29].

To address these characteristics of excitonic optical nonlinearities at room temperature we turn our attention to the waveguide (WG) geometry, which provides several advantages over the surface normal geometry. First, a large and variable optical depth is achieved simply by controlling the length of the WG sample, rather than by growing a large MQW structure. Second, the strong optical confinement in the WG allows the high optical intensities required to achieve CPO at RT to be more readily attained. Finally, the diffraction effects present in the tightly focused spot of the normal incidence experiments are suppressed as the optical field propagates as a confined WG mode. Ultimately the waveguide geometry is preferred for practical devices as it

simplifies integration with other components in a planar lightwave circuit. The observation of CPO in a WG geometry is also an important prerequisite to the creating an electron spin-based EIT resonance.

Despite exciton ionization, results are similar to those obtained at low temperature and reflect the general properties associated with a CPO process. More specifically, the measured operating bandwidth is related to the recombination rate of electron-hole pairs, *not* the lifetime of the excitons. Thus the spectral width of the CPO resonance is still narrow enough to generate a large group index.

The sample used in this study was grown on a (110)-oriented n-type GaAs wafer by MBE. Starting from the substrate, the structure consists of 1.19  $\mu\text{m}$   $\text{Al}_{0.26}\text{Ga}_{0.74}\text{As}$  (WG cladding), 0.17  $\mu\text{m}$  of  $\text{Al}_{0.15}\text{Ga}_{0.85}\text{As}$  (WG core), 60 nm  $\text{Al}_{0.3}\text{Ga}_{0.7}\text{As}$  (barrier), 5.4 nm GaAs (QW), 0.345  $\mu\text{m}$  of  $\text{Al}_{0.3}\text{Ga}_{0.7}\text{As}$  (barrier), and a 20 nm GaAs cap layer. The overall structure provides a single mode planar WG with the QW and barriers forming one of the cladding layers. Numerical simulation using this structure shows that only the fundamental mode propagates and that the QW is only slightly offset from the peak of the mode. Because of the small core size, the mode extends a considerable distance into the cladding. The QW confinement factor  $\Gamma$  is approximately 1%. The sample consists of a cleaved 440  $\mu\text{m}$  long strip. The strip is several millimeters wide, so there was no lateral confinement. The strip is mounted on a thin copper bridge using silver paste to provide good thermal contact.

The experimental setup is the same single-laser time domain configuration shown in Figure 3.4 except that the light is now coupled in and out of the waveguide, increasing

the difficulty of alignment. Initially we use TE-polarized light, defined as in-plane with the QW and the WG slab. A 20X (N.A. = 0.42) microscope objective couples light into the WG and 50X (N.A. = 0.55) objective re-collimates the beam at the output. The coupling efficiency, measured by tuning the laser below the absorption edge, varies depending on facet quality, but is typically on the order of 5%. Not all of the light incident upon the input facet couples into the waveguide, some of the light is scattered over the top of the waveguide, which can also be collimated by the output objective. Because of the absorption in the QW, this scattered light, which experiences no CPO, can mask the light from the WG. Therefore, spatial filtering at the output is crucial to separate scattered light from the WG mode. By using the transmission below the band-edge as a reference, we can compensate for imperfections in coupling and estimate the optical depth  $\Gamma\alpha L$  at the HH and LH exciton peaks as 4.1 and 5.0, respectively.

As before, delay is measured in two steps: first a reference trace is taken with  $\omega_0$  tuned below the HH exciton absorption, then a second trace is taken with the laser tuned into resonance with the HH transition.

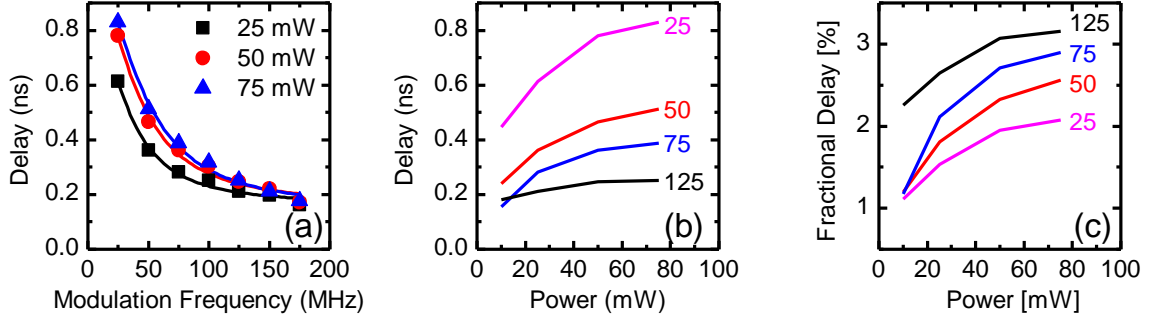


**Figure 3.8(a).** Delay as a function of modulation frequency for three different input powers. Solid lines are Lorentzian fits. All frequencies measured lie outside the zero GVD regime. **Figure 3.8(b).** Delay vs. pump power at various modulation frequencies (in MHz). The maximum power available, 75 mW, is still not quite enough to reach the peak delay seen in Figure 3.3(c). **Figure 3.8(c).** Fractional delay (RF phase shift) vs. input power for various modulation frequencies. Because the delay is decreasing sub-linearly with frequency, the fractional delay is higher at higher modulation frequencies.

Figure 3.8(a) plots delay as a function of modulation frequency at three different power levels. Delays of up to 830 ps are measured for 75 mW, the highest available input power. The solid lines are Lorentzian fits ( $n_{mod}(\delta)$  is a Lorentzian). The linewidth of the modulation delay is the same as the absorption dip [40], therefore the lifetime of the photoexcited electron-hole plasma can be extracted from the fits. The extracted lifetime of  $5.9 \pm 0.3$  ns is in excellent agreement with the value of 5 ns previously measured in (001) QW at room temperature [47]. This good agreement shows furthermore that recombination time as well as oscillator strength are comparable in (001)- and (110)-oriented QWs. A linear fit of the power dependence of the FWHM to  $\Delta\omega = 2(1 + P_{pump}/P_{sat})/T_1$  yields a value of 120 mW for  $P_{sat}$ .

Figure 3.8(b) plots  $\Delta T_{RF}$  as a function of pump power for different modulation frequencies. The beginnings of the same trend observed in the previous sections can be seen in Figure 3.8(b); the delay increases with increasing power and is just beginning to saturate. The maximum optical power available with our equipment (75 mW) is still insufficient to fully saturate the CPO response. The modulation frequencies studied are

outside the zero GVD part of the CPO resonance, consequently the delays are larger at lower modulation frequency.

Figure 3.8(c) presents the power dependence of the fractional delay  $\Delta T_{RF} \delta / 2\pi$  for different modulation frequencies. The maximum fractional delay of 3.2%, corresponding to an RF-phase shift of  $11.5^\circ$ , is measured at maximum pump power and a modulation frequency of 100 MHz. Since we are still below saturation of the hole depth, see Figure 3.8(b), we expect that the maximum achievable fractional delay can be slightly higher than the measured 3.2 %.

For the maximum delay of 830 ps measured, we obtain a modulation index of 565, which is three orders of magnitude smaller than that obtained in our low-temperature study. The primary source for the discrepancy is the WG geometry itself. The surface normal geometry allows the entire optical mode to interact with the QW active region while the WG has a significantly reduced confinement factor  $\Gamma$ . While the WG increases the intensity of the optical field and enables the near-saturation of the QW absorption resonance, and hence the generation of CPO, the reduced overlap of the optical mode with the active region means only a small fraction of the mode “feels” the CPO-induced dispersion. Thus, the mode travels with a greatly reduced modulation index  $\Gamma n_{mod}$ . One way to partially mitigate this problem would be to use a ridge WG structure; the lateral confinement would provide even larger intensities at a given pump power.

A second source of the discrepancy between the group index of the low temperature and room temperature experiments is that the modulation index is a lower bound on the group index. In the low temperature experiments  $T_1$  was smaller (1.3 ns) and the

modulation frequencies studied were within the zero GVD regime where  $n_{mod} \cong n_g$ . Figure 3.8(a) clearly shows that we are not studying this regime at room temperature, and  $n_{mod} < n_g$ .

### 3.3 Summary

Our experiments with CPO in semiconductor QW represent several important milestones. Slow light dispersion was measured in semiconductors for the first time [42] and a group velocity of 9,600 km/s was inferred. The bandwidth of this feature was a little over 1 GHz, several orders of magnitude larger than the first slow light experiments and approaching a bandwidth practical for communications. This achievement was followed by the first direct observation of time delay due to slow light in a semiconductor [48]. The group velocity was only 200 m/s but at the expense of bandwidth, leaving a DBP of approximately 3%. Finally, there was the first observation of slow light at room temperature in a semiconductor [49]. The group index was lower, but due to the WG geometry the propagation length was much longer (440  $\mu\text{m}$ ) and the DBP remained approximately 3%.

A second set of practical problems with CPO schemes in general relates to the configuration of the pump. The pump must be co-polarized with the signal and at the same wavelength. If the pump and signal co-propagate as well, then separating the two is impossible. The result is a degradation in the extinction ratio of the signal. It may be possible to mitigate this problem with nonlinear optical amplifiers such as those used for all-optical 3R regeneration [18]. A second issue is that the pump must be absorbed. This prevents the pump from remaining at an optimal value along the entire length of

the device. One solution is to divide the device into short, individually pumped sections. A second solution, population oscillations in a gain medium, is the topic of Section 4.

Finally these CPO results have important implications for implementing our EIT scheme in (110) QW. First, the EIT scheme requires a WG geometry due to the nature of the selection rules. Measuring EIT is just a matter of cross-polarizing the pump and signal beams. Second, the observation of the CPO response in a (110) QW demonstrates predominantly intrinsic carrier recombination. This is not a trivial achievement due to increased strain in (110) QWs and the corresponding increase in the possibility of forming dislocation defects. The electron spin coherence time cannot exceed the carrier lifetime, so the 5 ns  $T_1$  lifetime measured at room temperature further supports the idea that EIT based on electron spin coherence in (110) QW will be a sufficiently long-lived at room temperature to observe slow light.

## **4 Population Pulsations in Semiconductor Optical Amplifiers**

### **4.1 Motivation**

One of the major drawbacks of the CPO slow light scheme which we examined in the previous section is that the pump beam is absorbed during propagation. The deleterious effects of the pump attenuation extend beyond the requirement for higher pump power; a more important problem is the relationship between pump intensity and the dispersion of the system. Because of pump absorption, the pump intensity cannot be maintained at its optimum value throughout the length of the device. For a long device,

only the initial portion is capable of producing tunable delay. However, if the pump intensity can be maintained at an optimum throughout the device, then tunable delay increases linearly with increasing device length (up to the limit imposed by the SBP). Ordinarily, a CPO-like effect in a gain medium would produce a hole in the gain, or a reduction in transmission, leading to fast light. However, we shall see in the following sections that in semiconductors the hole is asymmetric and both slow and fast light may be observed. The pump intensity saturates toward a constant value, rather than falling to zero.

## 4.2 Background and Theory

When a semiconductor is biased to gain, a change in the carrier population  $N$  not only changes the gain, but also changes the index of refraction. This is ultimately linked to the asymmetry of the semiconductor gain spectrum. A symmetrical gain distribution, such as the Lorentzian line of an idealized two-level system, will be accompanied by a refractive index dispersion with a zero at the line center. If the inversion is changed, the height of the peak changes and the slope of the index dispersion changes, but the index remains unchanged. However, for an asymmetrical gain spectrum, the dispersion zero and gain peak will not coincide, and a change in gain at a fixed wavelength must also be correlated with a change in refractive index.

This change is quantified by the linewidth enhancement or “alpha” parameter [50]

$$\alpha_e \equiv \frac{d\chi_R/dN}{d\chi_I/dN} \quad 4.1$$

where  $\chi_R$  and  $\chi_I$  are the real and imaginary parts of the electric susceptibility and where  $N$  is the carrier density. This link between the gain and index has important consequences for the effects of population pulsations. Figure 4.1 shows the effect of  $\alpha_e$  increasing from 0 to 7 on the change in gain  $\Delta g$  (Figure 4.1a), the change in refractive index  $\Delta n$  (Figure 4.1b), and the group index  $n_g$  (Figure 4.1c). The situation when  $\alpha_e = 0$  (black curves) is analogous to the CPO in the absorption regimes discussed at length in Section 3. The pulsation of the carrier population causes a symmetric dip in the gain spectrum and an anti-symmetric index dispersion. Because the dip is in gain, the associated group index represents fast light ( $n_g < 0$ ). As  $\alpha_e$  is increased,  $\Delta g$  becomes more anti-symmetric,  $\Delta n$  becomes more symmetric, and  $n_g$  becomes anti-symmetric. The anti-symmetry of  $n_g$  means that a signal can experience either slow or fast light simply by changing the detuning from negative to positive detuning. Physically,  $\alpha_e = 0$  gives rise to a pulsation of the gain at the pump-signal beat frequency while the limit  $\alpha_e \rightarrow \infty$  gives rise to pulsations of the refractive index. Finite values of  $\alpha_e$  indicate that both the gain grating and index grating are playing a part in signal propagation.

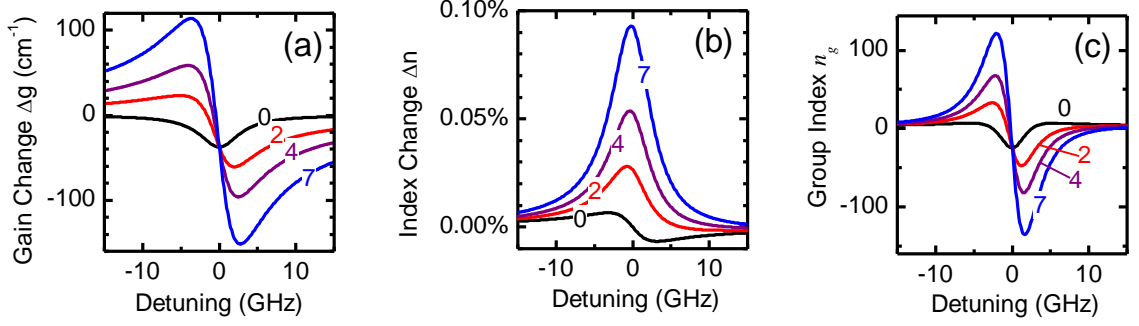


**Figure 4.1.** Change in material gain (a), refractive index (b), and group velocity (c) of signal due to pump-signal wave-mixing vs. pump-signal detuning for various values of  $\alpha_e$ . When  $\alpha_e = 0$  (black), there is a symmetric dip in gain and an anti-symmetric change in index, analogous to the CPO results shown in previous sections. At small detuning the signal experiences fast light ( $n_g < 1$ ). As  $\alpha_e$  is increased,  $\Delta g$  becomes increasingly anti-symmetric, and larger in magnitude. At the same time,  $\Delta n$  becomes more symmetric, leading to a sign change of  $n_g$  with detuning. For  $\alpha_e = 7$  (blue) the signal experiences fast light at positive detuning and slow light at negative detuning.

The first step in deriving quantitative expressions for  $\Delta g$  and  $\Delta n$  is to obtain the propagation equations for pump and signal fields. The slowly varying electric field envelope for a CW pump and signal (see Eq. (1.8)), is

$$A(z, t) = A_0(z, t) + A_1(z, t)e^{-i\delta t + ik_\delta z} \quad 4.2$$

where  $\delta = \omega_{probe} - \omega_{pump}$  is the radial frequency detuning and  $k_\delta$  is the corresponding slowly varying spatial frequency. In general, population pulsations of a gain medium can generate an additional amplitude at optical frequency  $\omega_{pump} + \delta$ . This wave is called the conjugate. In general the generation of the conjugate will strongly affect the propagation of the signal, but in this initial treatment we assume that the generation of the conjugate has been suppressed. For the solution to the carrier density rate equation we use the following ansatz [51].

$$N(z, t) = \bar{N} + N_\delta \cdot e^{-i\delta t + ik_\delta z} + c. c. \quad 4.3$$

where  $k_\delta$  is the spatial frequency of the pulsation and  $\bar{N}$  is the average carrier density. Assuming that the variations in carrier density are small,  $N_\delta \ll 1$ , we linearize the dependence of material gain upon  $N$

$$g(N) = g_N \cdot (N - N_{tr}) \quad 4.4$$

where  $g_N$  is the differential gain and  $N_{tr}$  is the carrier density required for transparency.

We describe the evolution of carrier density  $N(z, t)$  using Eq. (4.5) in the rate equation

$$\frac{\partial N}{\partial t} = -\frac{N - N_{SS}}{\tau_S} - v_{bg} \cdot g_N(N - N_{tr}) \cdot |E|^2 \quad 4.5$$

where  $N_{SS}$  is the steady-state value of the carrier density and  $\tau_S$  is the carrier lifetime.

Finally, we insert Eq. (4.5) into the propagation equation for the slowly varying electric field amplitude  $A(z, t)$

$$\frac{\partial A_j}{\partial z} - \frac{1}{v_{bg}} \frac{\partial A_j}{\partial t} = (1 - i\alpha_e) \cdot \Gamma g_N(N - N_{tr}) \quad 4.6$$

where  $j = p, s$  for the amplitudes of the pump and signal respectively,  $v_{bg}$  is the background group velocity for the “empty” waveguide, and  $\Gamma$  is the waveguide confinement factor. Note that  $\alpha_e$  introduces a complex coefficient to the gain, changing the phase shift of propagation which, by definition, is a change in refractive index.

Equation (4.3) and (4.5) will give solutions for  $\bar{N}$  and  $N_\delta$  which can be inserted into (4.6). Using (4.2) as a solution converts (4.6) to an algebraic equation between  $\omega$  and  $k$  for the pump and signal, which determines the signal index of refraction and gain:

$$\Delta n = \frac{c}{2\omega_{probe}} \cdot g_0 \cdot \frac{I_0}{1 + I_0} \cdot Re \left\{ \frac{\alpha_e + i}{(1 + I_0) - i\delta\tau_S} \right\} \quad 4.7$$

$$\Delta g = g_0 \cdot \frac{I_0}{1 + I_0} \cdot \text{Im} \left\{ \frac{\alpha_e + i}{(1 + I_0) - i\delta\tau_S} \right\}. \quad 4.8$$

where  $g_0$  is the *unsaturated* gain (gain at pump frequency in the limit of infinitesimally small input) and  $I_0 \equiv |E_0|^2 \cdot \tau_S v_{bg} g_N$  is a unitless parameter related to the pump intensity. Under the approximation that  $\alpha_e \gg 1$ , the maximum index change occurs at a detuning of  $\delta\tau_S = \pm(1 + I_0)$ .

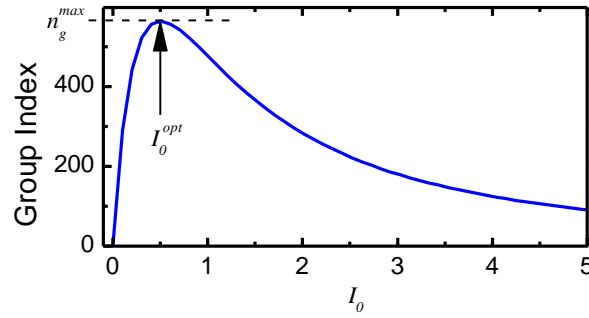


**Figure 4.2.** Group index  $n_g$  as a function of the dimensionless parameter  $I_0$  (proportional to the pump intensity) at the detuning  $\delta$  where  $n_g$  is maximal,  $\alpha_e = 7$ ,  $g_0 = 600 \text{ cm}^{-1}$ , and  $\lambda = 1.55 \text{ }\mu\text{m}^{-1}$ . The group index is maximal at an optimum value  $I_0^{\text{opt}} \cong 1/2$ .

Figure 4.2 shows the group index  $n_g$  at the detuning for which it is maximal as a function of  $I_0$ . The group index and optimum detuning are calculated numerically, without approximation, for  $\alpha_e = 7$ . There is clearly an optimum value when  $I_0 \cong 1/2$ . We would like  $I_0$  to maintain the optimum value over the length of the device. Under the assumption that the signal remains too weak to affect the pump, the evolution of  $I_0$  is also obtained from Eq. (4.6)

$$\frac{\partial I_0}{\partial z} = \left( \frac{g_0}{1 + I_0} - \beta \right) \cdot I_0 \quad 4.9$$

where  $\beta$  is the intrinsic loss of the waveguide. From Eq. (4.9) we see that  $I_0$  can be made constant throughout the waveguide by choosing  $\beta = g_0/(1 + I_0)$ , i.e. by designing a distributed loss into the device.

### 4.3 Simulation of Slow Light Propagation

Equations (4.7) – (4.9) allow us to numerically simulate the propagation of a data stream through a slow/fast light device based on the population pulsations described in the previous section. The flow of the simulation is very similar to that presented in Section 2.2 for EIT. A random stream of bits is rendered as a sequence of ideal square pulses in the time domain, translated to the frequency domain, sent through a low-pass filter, propagated through an SOA, and converted back to the time domain. Propagation through the SOA is done in steps: first  $I_0(z)$  is calculated by numerically integrating Eq. (4.9), then the device is divided into small slices, a transfer function is calculated for each slice, and finally the signal is propagated through each of the slices in succession. After converting the signal back to the time domain, it is divided up into bit slots and the traces from individual slots are overlaid on top of each other, forming an eye diagram. Shot noise and thermal noise are added to the signal in the form of Gaussian probability distributions with intensity-dependent variances. A very simple decision circuit calculates the probability of the intensity exceeding the decision threshold at the center of the bit slot. From this probability bit-error rate (BER) may be computed. Finally, the BER is computed for many different values of received power and compared to the BER vs. received power for a back-to-back link. The difference in received power required to maintain a BER of less than  $10^{-9}$  is the power penalty. The power penalty is a direct way of measuring the impact of distortion upon the design of a link.

### 4.3.1 Single Device

Table 4.1 shows the parameters which we will use for our simulation. We initially require that our device operate at a bit-rate of 10 Gbps, which is high enough to be of practical value for current fiber links. Some SOA parameters may be designed, while others are not easily adjustable. For the purposes of this simulation we take the carrier lifetime  $\tau_S$  to be fixed at 100 ps (for an SOA biased in the gain regime), the linewidth enhancement parameter  $\alpha_e$  to be 7, and the background group index  $n_{bg}$  (also equal to the background refractive index) to be 3.5. The waveguide loss  $\beta$  is determined by the requirement to keep  $I_0$  constant, while the device length  $L$  is limited by the requirement that the maximum gain not exceed a reasonable value, which we arbitrarily take to be 30 dB. There are three remaining “knobs” to adjust:  $g_0$ ,  $I_0$ , and  $\delta$ . We use our simulations to determine optimum values for these parameters.

Transmitter		SOA				Receiver (PIN)	
Bit-Rate	10 Gbps	$\tau_S$	0.1 ns	$\beta$	DEP.	Responsivity	1 A/W
Wavelength	1.55 $\mu\text{m}$	$\alpha_e$	7	$L$	DEP.	Load	50 $\Omega$
		$n_{bg}$	3.5	$g_0$	INDEP.	Dark Current	20 nA
				$I_0$	INDEP.	Bandwidth (Elec.)	10 GHz
				$\delta$	INDEP.	Bandwidth (Opt.)	100 GHz

**Table 4.1. Parameters for simulation. The unsaturated modal gain  $g_0$  and the dimensionless pump power  $I_0$  are the independent parameters. The waveguide loss  $\beta$  is chosen such that  $I_0$  is constant, the length  $L$  is chosen such that the total gain is less than 30 dB, and the detuning  $\delta$  is chosen for minimum spectral distortion.**

We first study the effect of the detuning  $\delta$ , searching for the optimal value. There are three factors to take into consideration when choosing a value for  $\delta$ . We would like to maximize the group index, minimize GVD, and minimize gain dispersion. Unfortunately, due to the asymmetry of the gain peak, these three factors cannot be optimized at a single detuning. Figure 4.3(a) shows typical curves for the gain (blue) and group index

(red) as a function of detuning. The group index is maximized and the GVD is minimized at detuning  $\delta_n$ , while the gain dispersion is minimized at detuning  $\delta_g$ . Figure 4.3(b) studies the difference between these two choices by plotting power penalty and DBP vs. device length for  $\delta_n$  (red) and  $\delta_g$  (blue). For this data we have used a narrow band signal ( $B = 2.5$  Gbps). At  $\delta_n$  group index is maximal, so DBP increases more rapidly with increasing  $L$ . However, the signal is suffering more distortion, as can be seen by the rapid increase in power penalty for  $L > 1$  mm. The lower power at  $\delta_g$  allows construction of a longer device with more storage (a higher SBP). Thus we will choose to operate at this point.

By taking the derivative of Eq. (4.8), an analytical expression for  $\delta_g$  can be found:

$$\delta_g = \frac{(1 + I_0)}{\tau_S} \cdot \frac{1 \pm \sqrt{1 + \alpha_e^2}}{\alpha_e} \quad 4.10$$

where the minus sign is for the gain peak (slow light) and the plus sign is for the gain valley (fast light). Equation (4.10) shows that when  $I_0 \ll 1$  the overall width of the spectral features induced by population pulsations depends only on carrier lifetime. When  $I_0 \gg 1$  the features broaden with increasing pump power. This is analogous to the power broadening of the CPO dip discussed in Section 3.1.

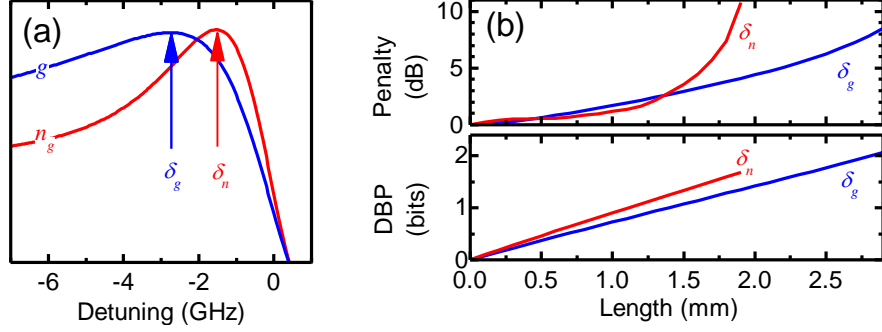


**Figure 4.3(a).** Gain  $g$  (blue) and group index  $n_g$  (red) as a function of pump-signal detuning. Two important values of detuning are highlighted with arrows:  $\delta_g$ , where gain dispersion is at a minimum, and  $\delta_n$ , where  $n_g$  is maximized and GVD is minimized. **Figure 4.3(b).** Power penalty (top) and DBP (bottom) vs. device length for signals detuned to  $\delta_g$  (blue) and  $\delta_n$  (red). The lower power penalty at  $\delta_g$  allows for larger fractional (higher SBP).

Next we turn our attention to the effect of  $g_0$ . First, we recognize that a frequency component of the signal at  $\omega_0 + \delta$  propagating a distance  $L$  consists of an amplitude change determined by  $g(\omega_0 + \delta)$ , and a phase change determined by  $n(\omega_0 + \delta)$ . Both of these are multiplied by  $L$  and sit in an exponential, yielding

$$E(L, \omega_0 + \delta) = E(0, \omega_0 + \delta) \cdot \exp \left[ \left( \frac{g}{2} + \frac{i(\omega_0 + \delta)}{c} n \right) \cdot L \right]. \quad 4.11$$

Inspection of Eq. (4.7), (4.8), and (4.11) reveals that  $g_0$  is always multiplied by  $L$  to keep the argument of the exponential dimensionless. We therefore conclude that the only effect of a change in  $g_0$  is to change the effective length of the device. Figure 4.4 shows the effect of sweeping  $g_0$  for various values of  $I_0$ . For each value of  $g_0$  and  $I_0$  the device length is set such that the gain is 30 dB. The delay (Figure 4.4(a)) is calculated from  $n$  and  $\partial n / \partial \omega$  at  $\delta_g$ , the bandwidth (Figure 4.4(b)) is calculated from the -3 dB points on either side of the gain maximum. Both delay and bandwidth are clearly independent of  $g_0$ . The difference is that larger values of  $g_0$  allow a given delay to be achieved with a shorter device (Figure 4.4(c)). Therefore, the unsaturated modal gain should be as high as possible.

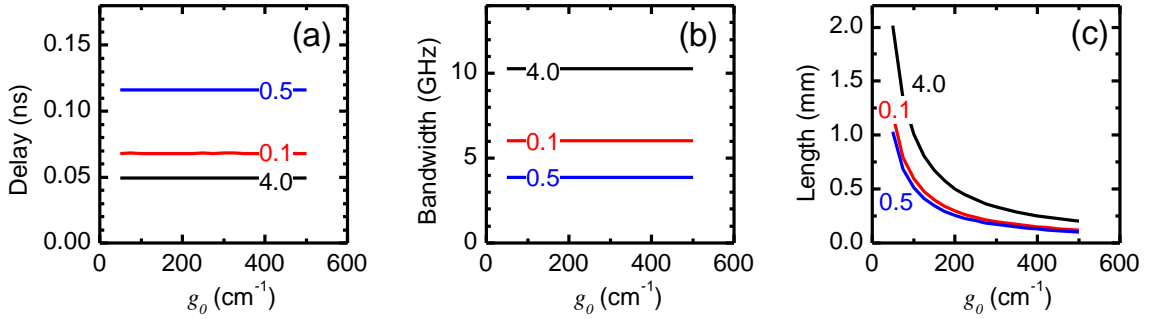


**Figure 4.4.** Delay (a), bandwidth (b), and maximum length (c) vs. unsaturated modal gain  $g_0$  for three values of  $I_0$ : 4.0 (black), 0.5 (blue), and 0.1 (red). Delay and bandwidth are independent of  $g_0$ , but larger values allow the same delay to be achieved in a shorter device. It is therefore desirable to have a large unsaturated modal gain.

We are now left with one more parameter to optimize. Figure 4.5(a) shows the impact of  $I_0$  on delay (blue) and bandwidth (red), as calculated in Figure 4.4. The functional dependence of delay is similar to that of  $n_g$  (Figure 4.2), but not identical, due to the dependence of  $L$  upon  $I_0$ . However, the bandwidth is at a minimum near  $I_0 \cong 0.5$ , where delay is at a maximum. The FWHM of the gain peak actually becomes constant for  $I_0 \ll 1$ , but the 3 dB bandwidth increases sharply as the overall height of the gain drops below 3 dB. Figure 4.5(b) shows the estimated maximum DBP and length as a function of  $I_0$ . For  $I_0 \gg 1$  the delay increases at the same rate that the bandwidth increases and the DBP saturates toward a constant value. A larger  $I_0$  realizes a larger bandwidth but the trade-off is an increase in device length. The smallest  $I_0$  which we expect to accommodate a 10 Gbps signal is 4, shown at the red arrow on Figure 4.5(a).

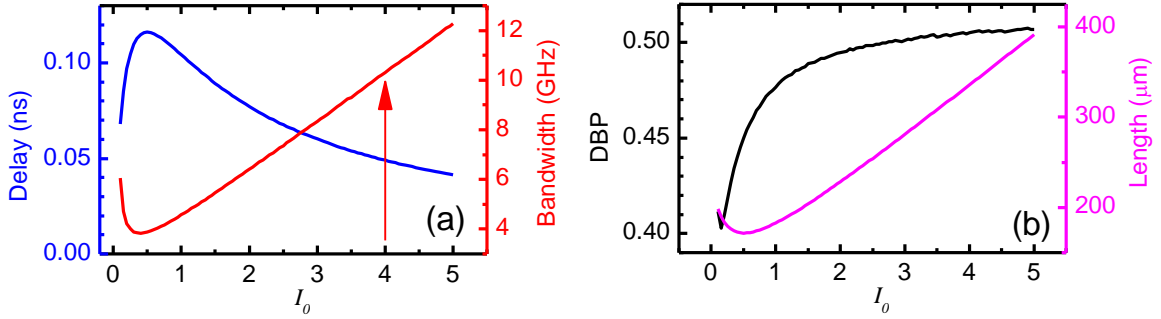


Figure 4.5(a). Delay (blue) and bandwidth (red) as a function of  $I_0$ . For each value of  $I_0$ , the length is chosen such that the maximum gain is 30 dB. The delay is calculated analytically from the group velocity at  $\delta_g$  and  $L$ . The bandwidth is calculated from the -3 dB points of  $G = \exp(gL)$  on either side of  $\delta_g$ . The red arrow indicates the lowest value of  $I_0$  with a bandwidth high enough for a 10 Gbps signal. Figure 4.5(b). Delay-bandwidth product (black) and length (magenta) as a function of  $I_0$ . When  $I_0 \gg 1$  delay is decreasing at the same rate bandwidth is increasing and DBP saturates to a constant value. The trade-off for increasing the bandwidth with very large  $I_0$  is that the required  $L$  increases linearly with increasing bandwidth.

Finally we examine the results of the numerical calculations performed above in the context of link performance. We simulate the transmission of a random stream of bits using the parameters given in Table 4.1 and  $\delta = \delta_g$  for various values of  $g_0$  and  $I_0$ . Figure 4.6(a) shows that the delay is independent of  $g_0$ . The same behavior is observed in power penalty, indicating that the bandwidth and GVD are also not functions of  $g_0$ . Figure 4.6(b) plots DBP (black) and power penalty (red) vs.  $I_0$ . The DBP follows the delay in Figure 4.5(a), decreases with increasing  $I_0$ , rather than saturating like the DBP plotted in Figure 4.5(b). This is because the *signal* bandwidth is not changing, the bit rate is held fixed, and therefore the DBP goes as the delay. The benefit of increasing  $I_0$ , the increase of spectral bandwidth, is reflected in the drop in power penalty. Note that there is a penalty of almost 5 dB at  $I_0 = 4$ , contrary to what was inferred from the bandwidth plot in Figure 4.5(a). This is due to other sources of distortion, including the asymmetry of the gain peak and the GVD. The trade-off between power penalty and small  $I_0$  directly translates into a trade-off between power penalty and device length.

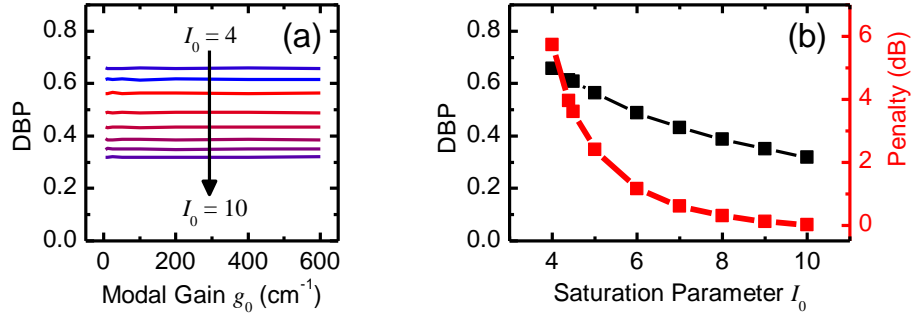


Figure 4.6(a). DBP as a function of modal gain  $g_0$  for various values of  $I_0$ . The delay is independent of  $g_0$ . Figure 4.6(b). DBP (black) and power penalty (red) as a function of  $I_0$  ( $g_0 = 300 \text{ cm}^{-1}$ ). The DBP drops like the delay as shown on Figure 4.5(a) rather than saturating as the DBP as shown on Figure 4.5(b) because the bit-rate is fixed at 10 Gbps. The decrease in bandwidth as  $I_0$  is decreased is reflected in the increasing power penalty.

### 4.3.2 Cascade

The limit on maximum gain restricts the maximum optical depth  $g_0L$ , and is the dominant limitation on DBP for large values of  $I_0$ . This restriction can be eased by including additional losses so that the total device gain is independent of  $I_0$ . However, the internal waveguide loss  $\beta$  is already set by the requirement that  $I_0$  be independent of  $z$ . Increasing  $\beta$  causes absorption of the pump and the advantages of working within a gain medium are lost.

Another possibility is the use of gain and attenuation stages. Each gain stage has its own pump and is followed by a broadband attenuator. This is similar to the work done by Öhman et. al. [53,52] and Maicas et. al. [54], where amplifiers were inserted between electro-absorption slow light devices to compensate for residual loss. With this scheme, the only limit on device length in our simulations becomes the amount of power penalty one is able to tolerate in the link. Figure 4.7(a) plots the DBP (black) and power penalty (red) vs. the number of slow light devices in such a cascade. The length of the slow light devices is chosen such that the gain of each device is 30 dB ( $g_0 = 100 \text{ cm}^{-1}$ ). The pump intensity parameter  $I_0$  has been increased to 8 where the power penalty of a single

device is small, see Figure 4.6(b). In order to quantify the advantages of a cascade, we arbitrarily select a maximal permissible power penalty of 4 dB. The 30 dB/device cascade reaches this limit partway through the third device in the cascade. The DBP at this point is 1.4 pulses. For comparison, Figure 4.6(b) shows that a single device subjected to the same 4 dB power penalty limit yields a DBP of only 0.5 (at  $I_0 \cong 4$ ), demonstrating a nearly 3-fold improvement by use of the cascade. Figure 4.7(b) shows the results from a similar simulation but with the gain per device limited to only 10 dB. The cascade extends to 5 devices before hitting the 4 dB limit, but the DBP is only 1.1.

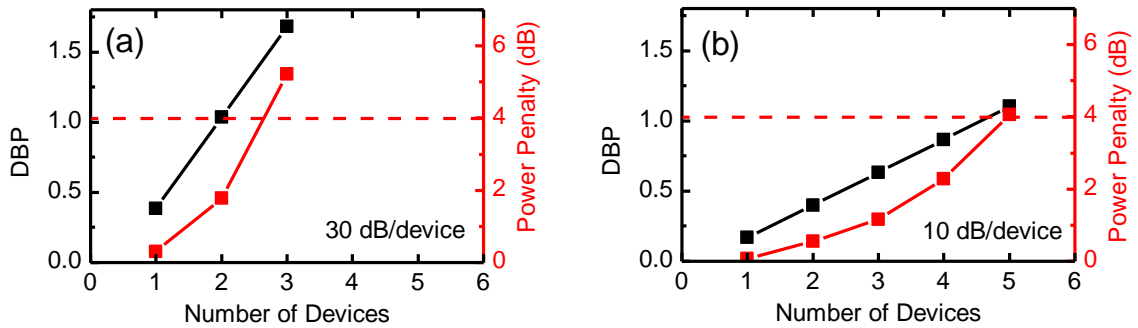


**Figure 4.7(a).** DBP (black) and power penalty (red) vs. number of slow light devices in a cascade. The gain of each device is 30 dB, each device is followed by a -30 dB attenuator. The power penalty exceeds our arbitrary limit of 4 dB between 2 and 3 devices at a DBP of 1.4 pulses. **Figure 4.7(b).** Same as (a) except the gain of each slow light device is limited to 10 dB. The penalty reaches 4 dB after 5 slow light devices, but the DBP is lower, only 1.1.

Another possible way of extending the DBP is to use a cascade of alternating gain- and loss-based slow light devices. Note that this scheme is quite different than the SOA – electro-absorption modulator (EAM) cascade studied in [53,52,54]. In that work, the EAMs provided slow light and the parameters of the SOAs were carefully chosen such that they would provide amplification without providing a counter-productive fast light effect. In this work, we leverage the alpha parameter to provide slow light in the gain stages *and* in the loss stages. The loss stages consist of an SOA biased below

transparency such that the population pulsations create a spectral hole in the loss. There are three primary differences between the reverse-biased and forward-biased SOAs. First,  $\alpha_e$  is zero for the reverse biased device, meaning that the situation is identical to CPO; there is a symmetrical hole in the absorption spectrum and an anti-symmetrical slow light dispersion. Second,  $I_0$  decreases along the length of the device. Third, the carrier lifetime  $\tau_S$  is reduced, leading to a broader spectral width.

Figure 4.8 shows the performance of this type of cascade by plotting DBP vs. number of devices for a power penalty limit of 4 dB. A color bar along the bottom of the figure indicates whether a particular span is through a gain-based device (blue) or an absorption-based device (red). The gain device parameters are fixed ( $I_0 = 8$ ,  $g_0 = 100 \text{ cm}^{-1}$ ) except the gain per device, which is varied from 10 dB to 30 dB. The carrier lifetime  $\tau_S$  of the absorption devices is varied from 30 ps to 100 ps,  $I_0$  is varied from 0.5 to 3.0, and  $g_0$  is varied from  $-10 \text{ cm}^{-1}$  to  $-400 \text{ cm}^{-1}$  ( $g_0 < 0$  for devices biased in absorption regime). The length of the absorption device is then set to cancel the gain of the previous stage. As can be seen by the grouping of the curves on Figure 4.8 in three families, the gain per device is the most important parameter, and the absorption device parameters have little impact. Also, the gain stages are providing most of the delay, particularly when the gain/device is 30 dB. Finally, the highest overall DBP achieved is 0.8. This is a 60% improvement over a single device, but not nearly as good as the 150% improvement from the gain/attenuator cascade discussed previously. As the signal passes through the gain and then absorption, it is subjected to two different gain spectra and index dispersions. The result is greater distortion and power penalty.

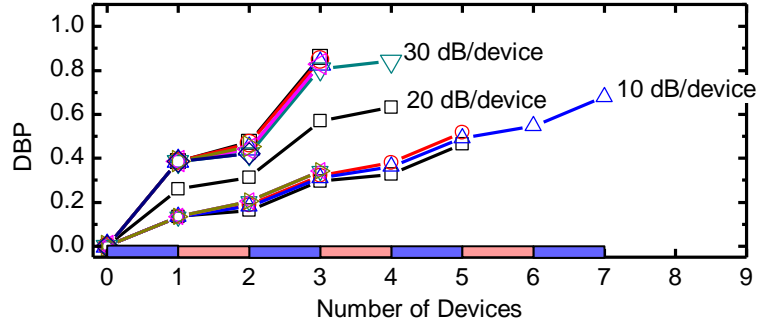


Figure 4.8. DBP vs. number of devices for a gain-based/absorption-based slow light device cascade with a 4 dB power penalty limit. The number of devices is the *total* number in the cascade, the colored bar indicates whether a particular span is gain-based (blue) or absorption-based (red). The gain/device took three values: 10 dB, 20 dB, and 30 dB, while the other parameters of the gain-based devices were held fixed ( $I_0 = 8$ ,  $g_0 = 100 \text{ cm}^{-1}$ ). The carrier lifetime, pump parameter, and unsaturated loss ( $g_0 < 0$ ) of the absorption devices were all swept, to little effect.

There are some important effects which are neglected in these simulations. Most important is the generation of the conjugate signal due to four-wave mixing (FWM). Generation of the conjugate and the subsequent influence of the conjugate upon the original signal slightly reduces the group index change and creates further asymmetry in the dispersion [55]. Additionally, separating the conjugate from the signal can be very difficult when  $\Omega$  is only a few GHz. Detection of the conjugate causes additional delay to be measured and inhibits detection of fast light advance [55]. A second complication which was omitted was the effect of the signal upon the pump as the signal is amplified. These effects can be mitigated by using low gain/device in a gain/attenuation cascade. Finally amplified spontaneous emission (ASE), which degrades signal-to-noise ratio and increases power penalty, will also play a significant role in long cascades.

#### 4.4 Simulation of Fast Light Propagation

We now turn our attention to the fast light detuning  $\Omega > 0$ . Earlier theoretical and experimental work on fast light propagation has focused on the speed of “information” and compatibility with Einstein’s Relativity theories [57,56,4]. In this section we analyze

some of the attributes of a fast light system in terms of practical metrics relative to a communication system. Rather than concerning ourselves with questions of where the “information” resides in a pulse, we are interested only in advancing the time at which a bit is detected. With regards to any distortion of the pulse we only concerned with the ability to correctly identify the bit as a 0 or 1, quantified in terms of BER or power penalty.

A practical simulation begins with practically realizable input pulses. As mentioned before, the data is first translated into a series of square pulses (NRZ amplitude encoding) and is then sent into a low-pass filter to create a realistic, finite-bandwidth pulse train. For the fast light system, the filtering process has increased significance. Figure 4.9 shows the propagation of a pulse through a fast light medium (red) and through an “empty” waveguide of the same length and group index  $n_{bg}$  (black) for filters of various order  $N$ . Figure 4.9(a) shows the case with no filter ( $N = 0$ ), the signal distorts severely and there is no advance. In Figure 4.9(b) a 2<sup>nd</sup>-order low-pass filter smooths the pulse, which experiences distortion and some advance. Figure 4.9(c) shows the pulses from a 4<sup>th</sup>-order filter, which has smoothed them to the point where they are nearly symmetrical peaks. Here there is only slight distortion. Finally, an 8<sup>th</sup>-order filter allows the pulse to propagate undistorted.

The causal nature of the low-pass filter and the fast light system both play a crucial role in this behavior. Because the low-pass filter is causal, it delays the pulses as it smooths them. In Figure 4.9(a) the middle of the reference pulse sits at 0.2 ns, while in Figure 4.9(d) it has shifted back to 0.7 ns. The fast light dispersion can advance the

pulses, but because it is causal it cannot advance them ahead of the “front,” the point where the pulse becomes non-zero, at 0 ns.

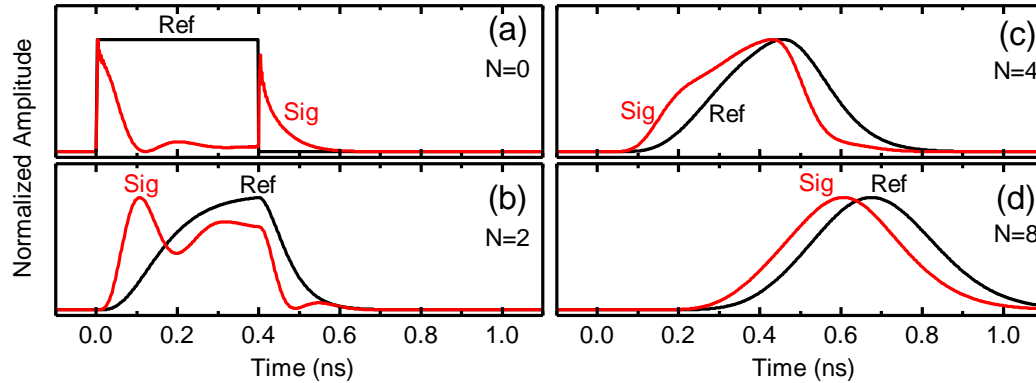
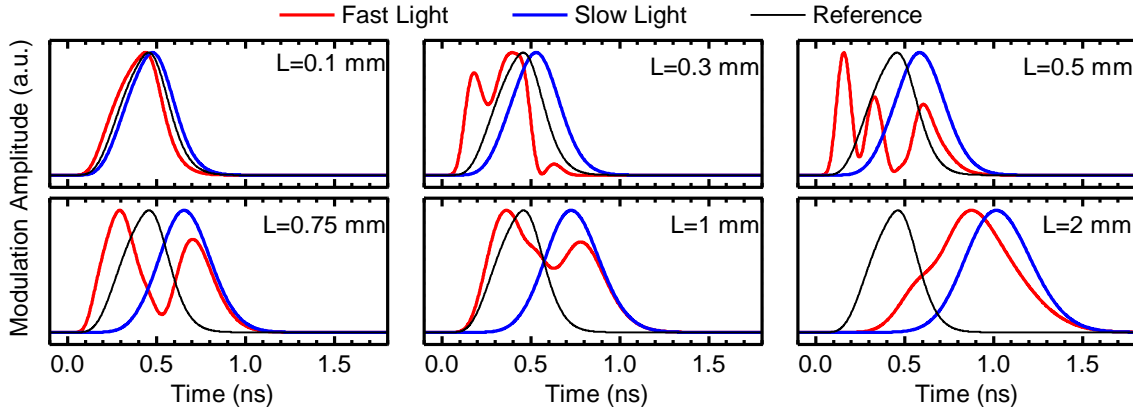


Figure 4.9. Advance of pulse due to fast light distortion for different filter orders  $N$ . The reference (black) is a pulse which travels through an “empty” waveguide of length  $L$  and group index  $n_{bg}$ . The signal (red) travels through the pumped SOA under the same conditions for all four plots. In (a) no filter is used, the signal pulse distorts but experiences no advance. As the filter order is increased, (b) – (d), the signal experiences more advance relative to the reference and less distortion. However, in addition to smoothing the input pulse the filters also *delay* the pulse from the turn on time at  $t = 0$ . The causal fast light system cannot advance the pulse past the time where the pulse first becomes nonzero.

We now examine the evolution of the fast light pulse as it propagates through the medium. Figure 4.10 shows the evolution of a 400 ps pulse from a 4<sup>th</sup>-order low pass filter at the fast light detuning (red) and the slow light detuning (blue) propagating through an SOA with  $g_0$  of  $150 \text{ cm}^{-1}$  and  $I_0$  of 1. Also shown is a reference pulse (black) propagating in an empty waveguide with group index  $n_{bg}$ . The zero of the time scale is set to the front of the reference pulse. Initially, the fast light pulse advances with little distortion ( $L = 0.1 \text{ mm}$ ) but further along the fast light pulse begins to distort severely as it hits the front ( $L = 0.5 \text{ mm}$ ). At this same distance the slow light pulse is still undistorted and is continuing to experience increasing delay. Still further along the device, the advance of the fast light pulse relative to the reference begins to decrease until the pulse is actually *delayed* ( $L = 2 \text{ mm}$ ).



**Figure 4.10.** Evolution of fast light pulse (red), and slow light pulse (blue) as they propagate through the device. Also shown is the reference pulse (black). At 0.1 mm, there is very little distortion, the fast light pulse is slightly ahead of the reference and the slow light pulse is slightly behind. As the length is increased to 0.3 mm and then to 0.5 mm, the fast light pulse “piles up” at the pulse front, while the slow light pulse continues to fall further behind the reference. From 0.75 mm to 2 mm, the fast light pulse begins to shift *behind* the reference and the distortion is decreasing.

This conversion from advance to delay can be understood by considering the propagation in the frequency domain. Figure 4.11(a) shows the spectrum of the input pulse (black), the pulse at  $L = 1$  mm (purple), and 2 mm (blue) along with the gain spectrum (red). The spectrum of the input spectrum is centered on the fast light dip. Due to the 4<sup>th</sup> –order filter the power is attenuated by 30 dB out at the slow light peak. However, the fast light frequency components are experiencing a loss while the slow light components are being amplified. After only 1 mm there is more power in the slow light components than the fast; after 2 mm the frequency components experiencing slow light dispersion are completely dominant. The transition from advance to delay is clearly illustrated in Figure 4.11(b), which plots DBP vs. propagation distance for pulses at the slow light detuning (blue) and at fast light detuning (red). The transition occurs sharply at about 0.6 mm.

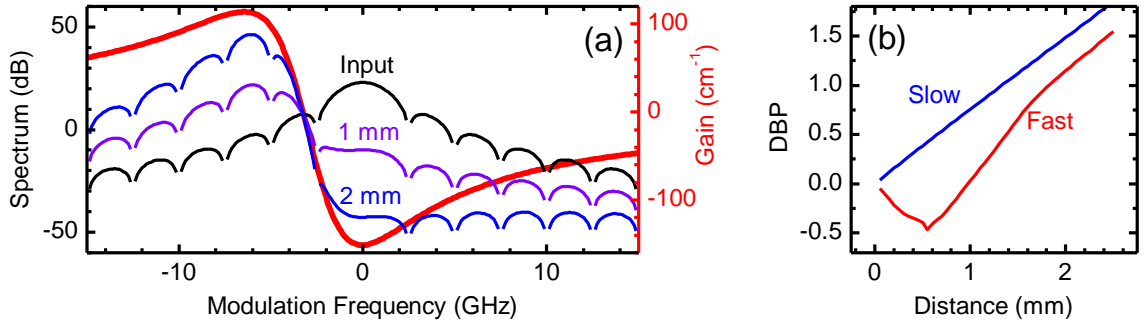


Figure 4.11(a). Spectra for a 400 ps pulse after propagating various distances (black, purple, blue), and gain spectrum (red). The original signal has passed through a 4<sup>th</sup>-order low-pass filter so that the majority of the signal power fits within the region of fast light dispersion. After propagating 1 mm the frequency components within the fast light region have been attenuated by 30 dB while the components within the slow light gain peak have been amplified by 25 dB. After traveling 2 mm the slow light components are 90 dB higher than the fast light components, and completely dominate the propagation. Figure 4.11(b) plots DBP vs. distance for a pulse centered at slow light detuning (blue) and fast light detuning (red). This plot clearly shows the transition of the fast light pulse to a slow light pulse as the device length is increased.

## 4.5 Experimental Results

Experimental results in support of this work are detailed in [55]. The first set of experiments consisted of modulating the signal with a 500 MHz sine wave and measuring the phase shift of this modulation as a function of detuning and pump power. The results are shown on Figure 4.12(a). At lower pump powers the delay vs. detuning has the same asymmetrical shape shown in Figure 4.1(c). At higher pump powers a significant amount of conjugate signal is generated and detected. In this case, a delay is measured at positive detuning, where there is normally an advance, and the advance measured is reduced. This is the behavior predicted by more complex numerical calculations where the assumption that the conjugate is suppressed is dropped.

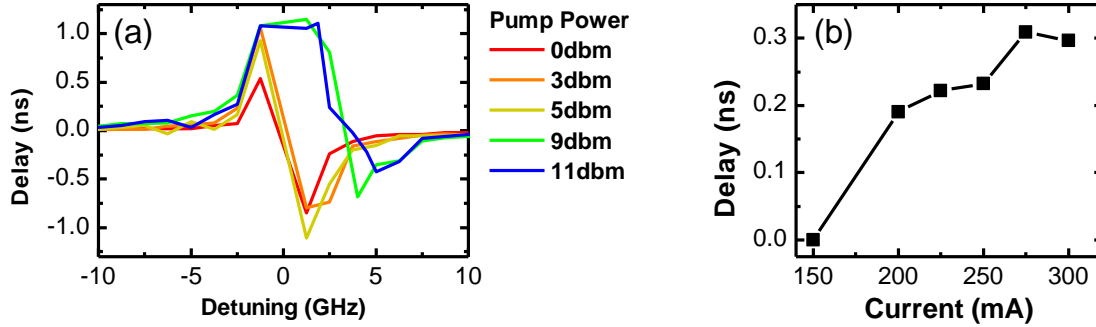


Figure 4.12. Experimental results for slow and fast light from population pulsations as reported in [55]. Figure 4.12(a). Delay of a 500 MHz sinusoidal modulation as a function of pump – signal detuning for various pump powers. At low pump powers the amount of conjugate remains small and the delay resembles the anti-symmetric curve in Figure 4.1(c). At higher pump intensities significant amount of conjugate signal is generated and detected, extending the slow light effect into positive detuning and reducing the measurable fast light advance. Figure 4.12(b). Delay of 1.3 ns pulses as a function of SOA bias current at a detuning of -3 GHz. Sweeping the current is equivalent to changing  $g_0L$ , and the curve shows a similar behavior, linear increase and just beginning to level off, is qualitatively similar to that shown in Figure 4.3(b).

The second type of experiment consists of modulating the signal with a single 1.3 ns pulse. Figure 4.12(b) plots the delay of this pulse vs. the bias current for a pump power of 0 dBm and a detuning of -3 GHz (slow light). Sweeping the bias current sweeps  $g_0L$ , and the curve shows a linear change beginning to saturate at higher values. This is qualitatively in agreement with the curve on Figure 4.3(b). The maximum DBP achieved is 0.3.

#### 4.6 Summary

Here we have presented a method of achieving slow light in a gain medium via a CPO effect. This eliminates residual absorption of the signal, but more importantly, the pump power can remain at a constant, optimal value throughout the length of the device. Thus the tunable delay of these devices increases linearly with length, up to the maximum allowed by the SBP of the device. However, in practice the residual *gain* is now a problem, as the signal amplitude must be kept small relative to the pump.

We examine two possible methods of mitigating this problem: a cascade of gain-based slow light devices and broadband absorbers, and a cascade of gain- and absorption-based slow light devices. Of these two schemes, the broadband absorber cascade ultimately performs better, as the absorption-based slow light cascade subjects the signal to two different GVD and transmission dispersions.

Finally we examine the fast light effect due to the gain dispersion. We observe that causality is preserved, and that signals can only advance up to their own front. Slow light does not suffer from any such limitation.

Practical difficulties remain with implementing CPO schemes in devices and experiment. The pump and the signal are co-polarized and co-propagating at very nearly the same wavelength. In a gain medium, the problem is further complicated by a presence of a third beam, the conjugate. Theoretical treatments and experimental data show that the interaction of the conjugate with the signal lessens the slow and fast light effect.

## **5 Intraband Effects in Semiconductor Optical Amplifiers**

### **5.1 Motivation**

In the Introduction, we have seen that the ratio of the bandwidth of a slow light system to the group velocity represents the number of “bits” that are stored per unit length. However, for a broad class of devices the length is related to bandwidth, resulting in a tradeoff between bit rate and maximum storage. This SBP is proportional

to maximum length and group index but proportional to the *square* of bandwidth. This demonstrates the primacy of higher bandwidths over higher group index when the goal is a maximization of total storage capacity. Another reason to examine systems with higher bandwidth is that it is only for very fast pulses that CMOS storage is no longer a viable alternative and all-optical buffering becomes necessary.

The mechanisms we have examined up to this point, EIT and CPO, have relied on transferring electrons from conduction band to valence band and back again. In modeling these effects, we have considered the semiconductor to be a two-level system. One of our original purposes for examining slow light in semiconductors was that the time scales for effects associated with these interband transitions were on the order of nanoseconds, much faster than the milliseconds of atomic systems. This offered bandwidth practical for communication systems, but certainly not beyond the capabilities of CMOS.

In this section we examine the use of *intragand* effects for the realization of slow and fast light in SOAs. The semiconductor will no longer be modeled as a two-level system, but rather as an ensemble of two level systems. As we shall see, rather than the nanosecond carrier lifetime or injection rate, the primary time constants are the picosecond and sub-picosecond carrier-carrier and carrier-phonon scattering times. This allows us to realize slow and fast light at THz bandwidths and to increase the A/DBP by more than an order of magnitude.

## 5.2 Background: Ultrafast Carrier Dynamics in an SOA

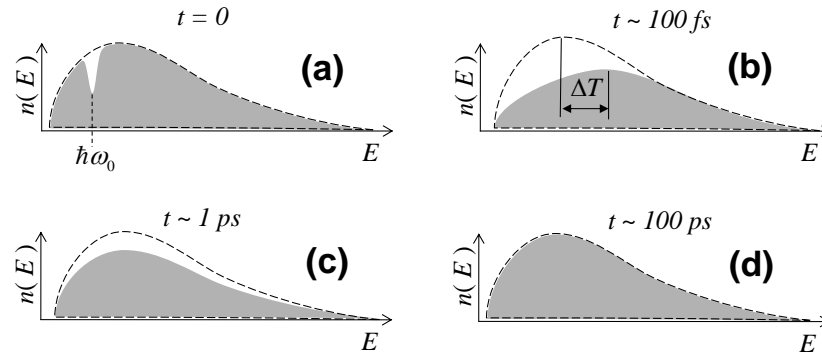


**Figure 5.1.** An illustration of the optical impulse response of the conduction band electrons in an SOA. At  $\omega_0$ , the optical frequency of the pulse, the SOA is biased in the gain regime. Immediately after the pulse the energy levels near  $\hbar\omega_0$  are depopulated via stimulated emission, a process called spectral hole burning (Fig. 5.1a). Carrier-carrier scattering then brings the population into thermal equilibrium at a temperature higher than the lattice temperature (Fig. 5.1b). This effect is called carrier heating. Carrier-phonon scattering brings the population back into thermal equilibrium with the lattice (Fig. 5.1c). Finally carrier injection brings the total number of electrons in the conduction band back to steady state (Fig. 5.1d).

Consider the response of an SOA to an optical impulse centered at frequency  $\omega_0$ .

There are three stages in the evolution of the conduction band electron distribution as it returns to steady state [58]. These stages are shown schematically in Figure 5.1. First, we consider the SOA biased such that the impulse, centered at optical frequency  $\omega_0$ , is within the gain regime. Almost instantaneously, the pulse depopulates the energy levels surrounding  $\hbar\omega_0$  via spontaneous emission (Figure 5.1a). This effect is called spectral hole burning (SHB), and leads to a very brief suppression of gain at frequencies within the hole. Carrier-carrier scattering causes the electrons to regain a Fermi distribution, filling in the hole. However, the initial interaction of the electrons with the pulse increases the average energy of the population and the thermalized carrier distribution is at a higher temperature than before. This phenomenon is referred to as carrier heating (CH) (Figure 5.1b). There are several mechanisms by which the pulse increases the average energy of the population. A small fraction of electrons participate in two-

photon absorption or free-carrier absorption, but these processes impart large amounts of energy to the carriers involved. Thus, these infrequent processes can significantly increase the average energy of the population. CH leads to a decrease in gain at all wavelengths above the band gap. The carriers cool to the lattice temperature via carrier-phonon scattering (Figure 5.1c). At this point, the electron distribution is congruent with that of the steady state, but the number of carriers (integrated over all energy levels) is smaller; the SOA is in a state of carrier depletion. Finally, carrier injection increases the number of electrons back to the steady state value (Figure 5.1d). SHB and CH are called “intraband” effects, and usually take place on picosecond and sub-picosecond time scales. Carrier depletion is an “interband” effect.

If the SOA is biased such that the impulse is within the absorption regime, then these effects are altered. The pulse will initially increase the occupancy of energy levels near  $\hbar\omega_0$ , creating a “hole” in the absorption spectrum. In contrast to the gain case, SHB in absorption increases transmission. The electrons thermalize to a Fermi distribution above lattice temperature, again experiencing the CH effect and an increase of absorption at all wavelengths. CH decreases transmission in both the gain and absorption regimes. After cooling back to the lattice temperature, the total electron population is still greater than it was in the steady state and in contradistinction with the gain regime, the transmission is higher. The total number of electrons decreases back to steady state with spontaneous emission or carrier sweep out.

Carrier-carrier scattering is much faster for the holes and thus they can be assumed to remain in a Fermi distribution. The hole population distribution only affects the

interband processes: the initial stimulated emission that creates the spectra hole and the final relaxation of the carrier depletion.

### 5.2.1 Potential for Slow and Fast Light

The ultrafast intraband effects of SHB and CH can drive ultrafast optical nonlinearities, which can be used for broad bandwidth ( $> 1$  THz) slow and fast light. Most obviously, the dip in gain or absorption caused by SHB is reminiscent of the spectral holes caused by EIT and CPO. Indeed, SHB has been used before to demonstrate slow light in atomic systems [59], but with a separate pump beam burning the hole, allowing the SHB to be treated as a linear system with respect to a weak signal. While such a scheme might work in principle in semiconductors, the power required for a CW pump to burn an appreciable hole would be too high. A short pulse with duration on the order of the SHB relaxation time has an easier time burning such a hole. Rather than use a pulsed pump to induce slow or fast light on a signal pulse, a simpler scheme is to simply use the same pulse as both pump and signal.

It is not immediately obvious that a pulse traveling in its own hole will experience a fast light dispersion. The Kramers-Kronig relations assume a linear system response, which is not the case here. Assuming that the pulse will experience a fast light group index, the lifetime of the hole becomes important. In the limiting case where the pulse is much longer than the SHB recovery time (dictated by carrier-carrier scattering), then the electrons remain in a Fermi distribution throughout the pulse and no hole in the gain is formed. As we are interested in exploring the group delay experienced by an ultrashort pulse due to the spectral hole created by the pulse itself, it is essential to

measure the SOA gain dynamics and establish a time regime within which the spectral hole can be sustained.

Measurements of ultra-fast gain dynamics in semiconductors using time domain pump-probe experiments were pioneered more than two decades ago [61,58,60]. Our experimental setup is shown in Figure 5.2. A mode-locked fiber laser produces pulses of 500 fs duration and approximately 4 W of peak power. The 25 MHz repetition rate allows 40 ns for the SOA gain to recover before the next pulse arrives. The pulses are split into a pump (90%) branch and probe (10%). The pump pulse removes large numbers of carriers from the conduction band in a short amount of time via stimulated emission. The probe is delayed by a variable amount  $t_0$  before entering the SOA. Measuring the probe transmission as a function of  $t_0$  maps out the transient gain response with a temporal resolution on the order of the pump and probe pulse width. To distinguish between the pump and probe at the detector, the probe is mechanically chopped at 2.5 kHz and lock-in detection is used. The 50/50 combiner is made with polarization maintaining fiber, assuring that the pump and probe are co-polarized. The SOA is a fiber-coupled commercial device designed for operation at 1550 nm with a small signal gain of 28 dB and a saturation power of 13 dBm. It is polarization insensitive with less than 2 dB polarization dependent gain.

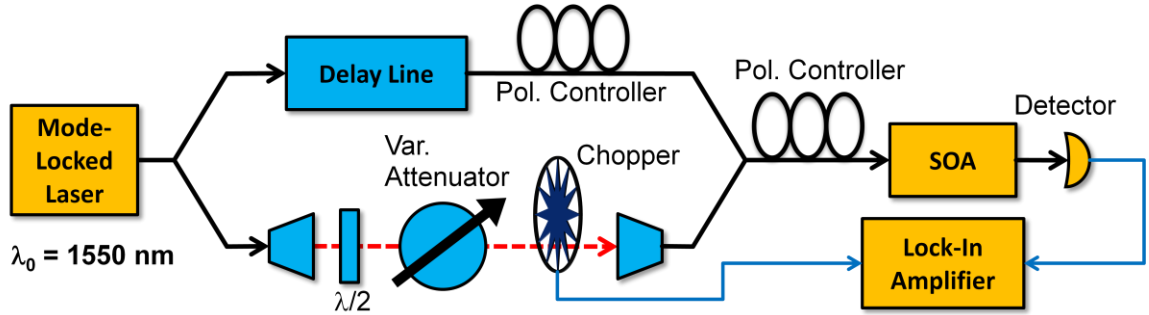


Figure 5.2. Experimental setup for measurement of gain dynamics. Fiber is shown in black, free-space in red, and electrical connections in blue. The pulses are split into two branches, the pump (90%) and probe (10%). The probe propagates through a half wave plate, a polarizer, a variable attenuator, and a mechanical chopper for lock-in detection. The free-space propagation distance of the probe is varied with a precision linear stage. The polarization state of the pump is adjusted with a fiber polarization controller and matched to that of the probe. Both are polarized along the slow axis of the PM 50/50 splitter. A final fiber polarization controller adjusts the polarization state of the SOA input.

Measurements of average probe intensity as a function of  $t_0$  yield the recovery times for the different gain suppression effects. Assuming that the gain saturation response is linear in pump power, the average probe intensity at the SOA output can be expressed as [62]

$$I_{probe}(t_0) = \int h(t' + t_0)F(t')dt' \quad 5.12$$

where  $h(t)$  is the impulse response of the medium and  $F(t)$  is the cross-correlation between pump and the probe. The impulse response function is assumed to be of the form [58]

$$h(t) = u(t) \cdot (a_0 + a_{SHB}e^{-t/\tau_{SHB}} + a_{CH}e^{-t/\tau_{CH}}) \quad 5.13$$

where  $u(t)$  is the unit step function and  $\tau_{CH}$  and  $\tau_{SHB}$  are relaxation time constants for the gain saturation effects under consideration. At the time scale of our experiment, the effect of carrier depletion is a constant ( $a_0$ ).  $I_{probe}(t_0)$  and  $F(t)$  are measured at three SOA bias currents: one for gain, one for transparency, and one for absorption. At each bias current we fit the  $I_{probe}(t_0)$  data by varying  $a_0$ ,  $a_{SHB}$ , and  $a_{CH}$  in Eq. 5.13 and then

numerically integrating Eq. 5.12. We recursively search for values of  $\tau_{CH}$  and  $\tau_{SHB}$  which produce the best fits at all bias currents. This process is similar to those used in [58,63]. Figure 5.3 shows the pump-probe cross-correlation at the input and output of the SOA. For our setup the pump and probe pulse widths are the limiting factor. Unfortunately, as can be seen in Figure 5.3, the pulses are broadened significantly as they propagate through the SOA. We find that the best fits are obtained when we use the output cross-correlation traces in Eq. 5.12.

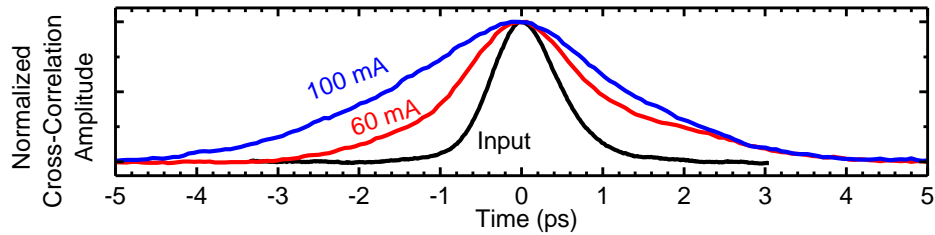


Figure 5.3. Broadening and distortion of pump-probe cross-correlation after propagation through the SOA at various currents. Note that cross-correlation traces shown above are broader than the actual pulses.

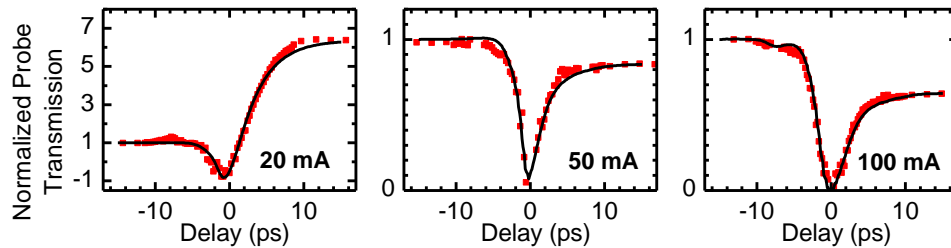


Figure 5.4. Normalized probe transmission vs. delay for three SOA biases: absorption (20 mA), near transparency (50 mA), and gain (100 mA). Data points are red squares, black lines are fits. The fits consist of a simple analytical impulse response (Eq. 5.13) numerically convolved with the pump-probe cross-correlation (Figure 5.3).

Figure 5.4 shows the data and fits at three different SOA currents: 20 mA, 50 mA, and 100 mA corresponding to absorption, near transparency, and gain. At absorption bias, the probe absorption will be first reduced due to SHB by the pump, and subsequently increased due to the CH effect. On the other hand, with the SOA biased in the gain region, SHB and CH both are expected to reduce the gain. At transparency, the

contribution of SHB to the impulse response should be zero, while CH will decrease the probe transmission. Note that in all three cases the effect of CH is to attenuate the probe, whereas SHB will amplify or attenuate depending on the bias [58]. The time constants which best fit the data in all three regions are 0.83 ps and 3.3 ps. Corresponding coefficients  $a_{SHB}$  and  $a_{CH}$  at the different bias points are given in Table 1. The signs of the coefficients are as expected, switching from positive to negative for SHB and remaining negative for CH. The best-fit time constant for spectral hole burning is at the limit of our resolution. Prior measurements on InGaAsP strained layer multiple quantum well amplifiers place the carrier-carrier scattering time for SHB relaxation at approximately 100 fs and the carrier-phonon scattering time for CH relaxation at approximately 1 ps [58,64]. The time constants we obtained here are well within the acceptable range, given the effects under consideration are strongly dependent on wavelength, material composition, and QW structure. Hence, we conclude that pulses having a width comparable to 0.83 ps should be within the time scale where the carriers depleted by a pulse have not completely relaxed to a Fermi-Dirac distribution. In this case, the pulse may travel within a spectral hole created by itself and experience a group delay.

Transient Effect	Relaxation Time	Coefficients ( $a_{SHB}$ or $a_{CH}$ )		
		Absorption	Near Transparency	Gain
Carrier Heating	3.3 ps	-14.2	-0.61	-0.61
Spectral Hole Burning	0.83 ps	7.47	-1.62	-2.37

**Table 5.1.** Time constants and coefficients from Eq. (5.13) for intraband gain or absorption saturation effects. A negative coefficient corresponds to an initial decrease in probe transmission relaxing upward with the specified time constant.

## 5.3 Experimental Results

### 5.3.1 Setup, Equipment, and Techniques

Figure 5.5 shows the basic schematic for a generic intraband fast light experiment. A mode-locked laser produces a train of sub-picosecond pulses at 1550 nm. The pulses are split into two arms: the reference and the signal. The reference goes through a fixed delay and into one port of an optical cross correlator. The signal pulses pass through a variable attenuator and polarization controller before entering the SOA. The polarization controller is required because we find that the amount of delay and advance as well as the output pulse shape depend upon carefully selected input polarization. At the SOA output, the signal passes through additional polarization control and into an Erbium-doped fiber amplifier (EDFA) to boost the signal (the polarization control is required here because our EDFA happens to be a polarization maintaining device). Finally the signal is routed into the other arm of the cross-correlator. All experiments are performed at room temperature. The SOA bias current or input pulse power is changed and the delay or advanced is measured from the cross-correlation traces. Optical cross-correlation is discussed in more detail in the Appendix.

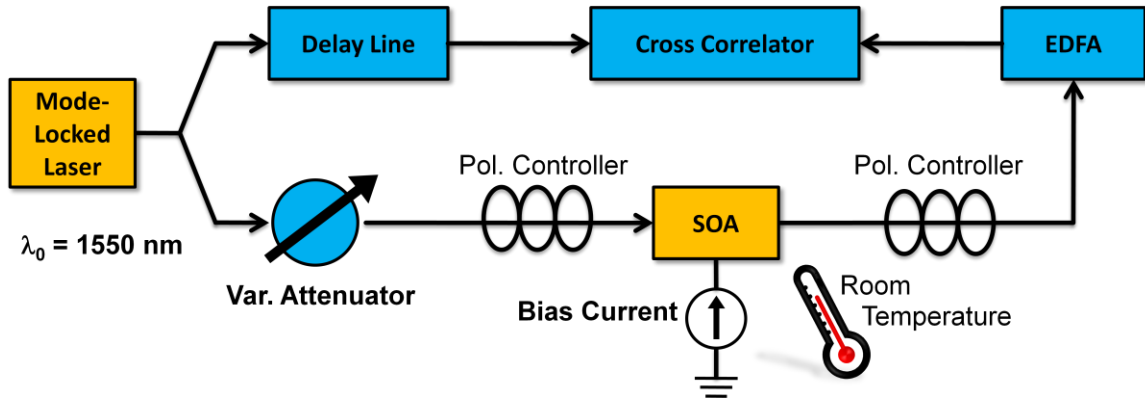


Figure 5.5. Basic schematic of experiment to measure advance and delay of pulses. Sub-picosecond pulses are generated by a mode-locked laser. The light is split into a fixed reference path and a signal path, which passes through the SOA. Delay and advance are measured from optical cross-correlation traces. All experiments are conducted at room temperature.

### 5.3.2 Fast Light Results

Our initial experiments used fiber based components. The SOA used was the same one on which the gain dynamics measurements were performed, a packaged, fiber coupled device with 28 dB small signal gain and 13dBm output saturation power. The mode-locked laser is also the same one described above: 500 fs pulses at a 25 MHz repetition rate.

Because each component in our setup has long ( $\sim 1$  m) fiber pigtailed, there are several meters of fiber between the output of the laser and the input of the SOA. Because this fiber can cause broadening, we need to measure the pulse width at the SOA input to calculate the ABP. Figure 5.6(a) shows an auto-correlation trace of the pulse at the SOA input (black). Assuming a  $\text{sech}^2$  pulse shape, the pulse width is obtained by multiplying the FWHM of the auto-correlation trace by the deconvolution factor of 0.65 (see Appendix). The input pulse has broadened from 500 fs to 720 fs due to fiber dispersion between the laser and SOA input. Also shown in Figure 5.6(a) is a

typical pulse after propagation through the SOA (red); for a bias current of 70 mA the pulse width is 1.5 ps.

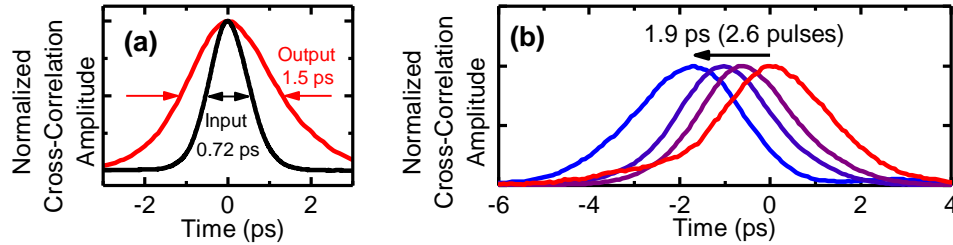
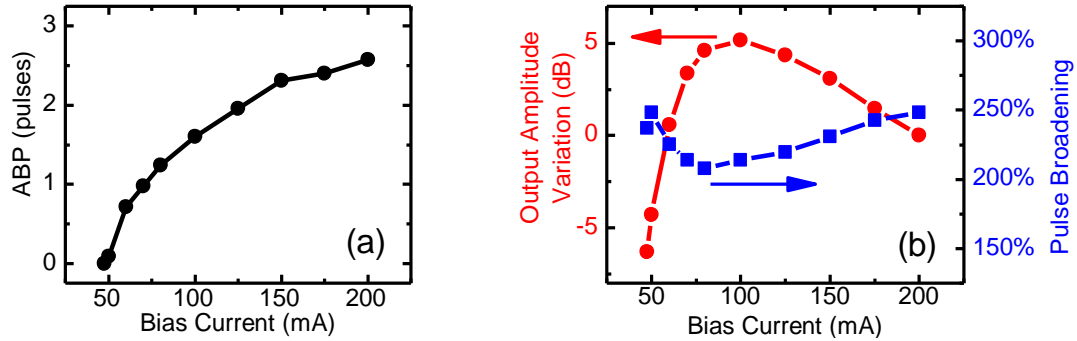


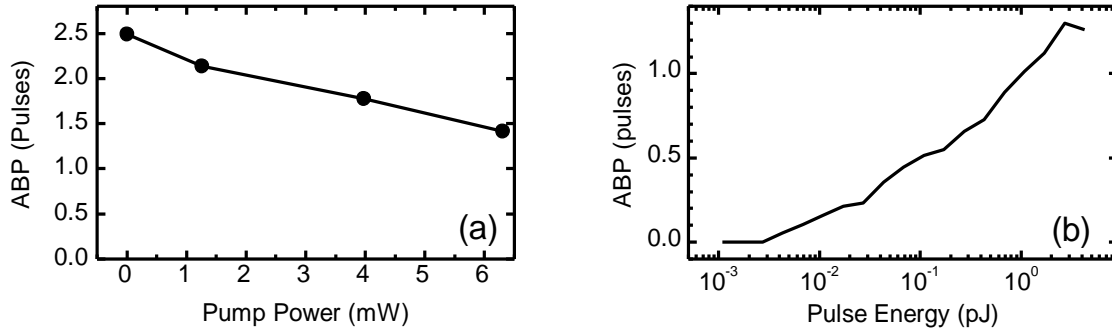
Figure 5.6(a). Normalized auto-correlation at the SOA input and signal-reference cross-correlation at the SOA output (70 mA). FWHM, assuming  $sech^2$  pulse shape, is labeled on the figure. Figure 5.6(b). Normalized cross-correlation at the SOA output showing delay of pulses as current is varied. Note that the cross-correlation traces are broader than the actual pulses.

Figure 5.6(b) shows normalized cross-correlation traces as SOA bias is swept from 50 mA (near transparency) up to 200 mA (maximum gain). The negative temporal shift of the pulses shown in Figure 5.6(b) is the signature of fast light. A continuously tunable advance of up to 1.9 ps is observed, corresponding to an ABP of 2.5. It should be noted that the actual pulses are narrower than the cross-correlation traces of Figure 5.6(b). Because the SOA is providing gain, SHB corresponds to fast light dispersion. As the SOA current is increased, the gain is increased and the input pulse experiences a deeper spectral hole. This leads to a larger negative group index and further advance of the pulse. This trend of increasing advance with increasing SOA gain is shown more clearly in Figure 5.7(a), where the ABP is plotted against bias current.



**Figure 5.7(a).** ABP vs. SOA bias current. **Figure 5.7(b)** Amplitude variation (red) and pulse broadening (blue) as a function of SOA bias current. Change in amplitude is measured relative to amplitude at maximum gain.

Amplitude variation and broadening of the output pulse are plotted in Figure 5.7(b) as the advance is tuned. The red curve is the variation of pulse amplitude plotted against SOA bias current. Change in amplitude is measured relative to amplitude at maximum gain. There is less than 11 dB amplitude variation over the entire tuning range, despite the fact that small signal gain is varying by almost 30 dB. This is more evidence that the pulse is strongly affected by SHB and CH. Also shown in Figure 5.7(b) is the variation in pulse broadening (blue), defined as the ratio between output pulse duration and input pulse duration, as the current is changed. The pulse duration is approximately doubled after propagation through the SOA, and varies by about 50% as the bias current is swept. Most of this broadening is in fact due to the long fibers connected to the SOA and polarization controllers. Free-space optics as well as pre- and post-propagation dispersion compensation techniques will eliminate the “background” pulse doubling, as will be discussed in later sections. The pulse duration decreases with increasing amplification such that the broadening is inversely correlated to the amplitude change.



**Figure 5.8. Optical control of group velocity.** Figure 5.8(a) shows the tuning of ABP via a counter-propagating CW pump beam injected at the SOA output. Values plotted are for SOA biased at maximum gain; the advance is measured relative to the SOA biased at transparency. Increasing the pump depletes carriers and decreases the depth of the spectral hole. Figure 5.8(b) is a study of ABP as a function of input power for fixed SOA bias. Pulses with larger energy and higher peak power burn deeper holes, experiencing more advance.

There are two ways in which the group velocity may be tuned optically. Our first attempts at optical control involved injecting a 1550 nm CW pump into the output of the SOA, counter-propagating with respect to the signal. This technique was successful in atomic SHB slow light experiments [59], where increasing the pump power deepened a spectral hole in absorption and delayed the signal pulse. In our experiments, the maximum advance obtained by sweeping SOA bias (gain) was measured at several different pump powers. Figure 5.8(a) shows the maximum ABP obtained as a function of pump power. The advance is shown to decrease as the pump power increases. This indicates that the pump is not burning a hole (in which case advance would increase with increasing pump power) but rather is simply depleting the steady state carrier density. Higher pump means lower steady state gain which means less depth in the spectral hole.

The second way to control optical group velocity is to simply change the input pulse energy. We studied the effect of input power on advance by sweeping the SOA bias at several settings of the variable attenuator (see Figure 5.5). The maximum ABP obtained

is plotted against input pulse energy in Figure 5.8(b). As pulse energy increases, ABP increases, demonstrating the ability of the pulse to burn a deeper hole. At some point, it is expected that this increase should saturate suddenly when the input pulse energy is so high that the pulse immediately burns a hole down to transparency. The last two data points on Figure 5.8(b), at the highest pulse energies, might be the beginnings of this saturation effect. The relationship between pulse energy and advance is somewhat complicated, since a pulse which initially does not burn a deep hole may acquire enough gain during propagation that it burns a hole down to transparency near the output. Limitations due to saturation of hole depth will be discussed in more detail in the section on time-wavelength division multiplexing (TWDM).

These initial experiments yielded extremely promising results. The ABP of 2.6 is a large jump over our previous work with FWM ( $A/DBP=0.45$ ) [55] and was also a world record for semiconductors in general. Additionally, it exceeds the requirement of  $ABP > 1$  necessary for some applications in RF photonics. The previous record, a DBP of 2.0, was achieved with exciton-induced dephasing in GaAs quantum wells [65], a technique which is only effective at low temperatures. Our work was done at room temperature and at communication wavelength. But most importantly, the experiments were conducted with signal bandwidths far in excess of the capabilities CMOS, the regime where all-optical signal processing becomes a necessity.

### 5.3.3 Slow Light

SHB and CH effects are also present when the SOA is biased below transparency, in the absorption regime. In this situation SHB will decrease the absorption felt by the

pulse. A decrease in absorption is associated with a slow light group velocity, and we expect to observe delays.

These delays are observed with the same basic experimental setup used to measure the advance (Figure 5.5). In this case, we use the full power from our newer mode-locked laser, producing pulses at a 20 MHz repetition rate with a peak power of approximately 300 W. The pulse duration at the SOA input is 600 fs (FWHM, assuming  $\text{sech}^2$  pulse). It is the higher power of the laser which allows observation of the pulse when the SOA is biased below transparency. For these experiments the fiber-coupled SOA was used and all other components, such as the polarization controllers, are also fiber devices.

Cross-correlation measurements reveal a smooth transition from delay to advance as SOA bias current is swept. Figure 5.9 shows the cross-correlation traces as the SOA current is increased from 17 mA to 100 mA, a change in small-signal “gain” of more than 50 dB. The transition from absorption to gain for this SOA (see Figure 5.4) occurs at approximately 50 mA. At currents below 50 mA the background absorption is increasing as the bias is decreased. This allows the pulse to burn a deeper hole, increasing delay. The total temporal shift (delay plus advance) is 1.52 ps, an A/DBP of 2.5 pulses.

Increasing the SOA current beyond 100 mA results in significant pulse distortion due to gain saturation effects. The large input powers required to observe significant delay in the absorption regime also cause broadening and other distortion in the gain regime. Additionally, we observe that settings of the polarization controllers which minimize distortion and broadening in the gain regime are different than the settings which

optimize for the loss regime. For the data in Figure 5.9 we have set the polarization controllers to a point with the best compromise between optimizing for the loss regime and optimizing for the gain regime. Free space measurements are required to obtain a clearer picture of the difference between slow and fast light with respect to polarization. Additionally, the large pulse powers are generating nonlinear effects in the fiber before and after the SOA, compounding the problem of pulse broadening and distortion.

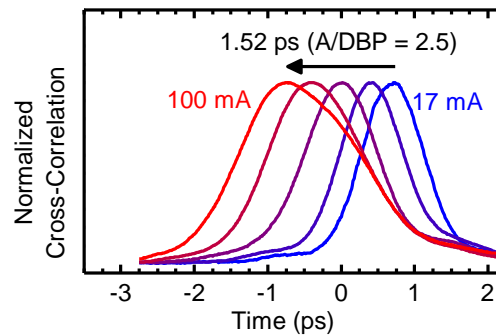


Figure 5.9. Continuous tuning from slow to fast light. SOA bias is swept from 17 mA through transparency (50 mA) to 100 mA. Above transparency, gain increases with increasing bias and hole deepens, leading to larger advance. Below transparency, absorption increases with decreasing bias, leading to larger delay. The total temporal shift is 1.52 ps, an A/DBP of 2.5 pulses. Above 100 mA the pulse becomes even more distorted. This is because large delay and large advance require different optimizations of experimental conditions, as discussed in the text.

Slow light measurements are more difficult than fast light measurements because the required powers are higher. Nevertheless, investigation into slow light is particularly important. First there are subtle differences between the physical mechanisms which may contribute in the absorption and gain regimes. Second, the gain dispersion associated with fast light consists of reducing transmission of central frequency components, creating a “notch filter” effect. For large advances, this will ultimately cause fast light pulses to “break apart” [66], see results in Section 4.4.

### 5.3.4 Cascaded SOAs

If a pulse traverses a device with a group velocity of  $v_g$ , the most obvious way to extend the total advance or delay is cascade two of the devices together. In this section we present experiments performed to assess the feasibility of such a cascade for two of our SOAs acting as fast light devices in the gain regime. We modify our experimental setup such that the single SOA is replaced by two devices with an optical isolator and an additional polarization controller between them. The bias currents of the SOAs can now be controlled independently.

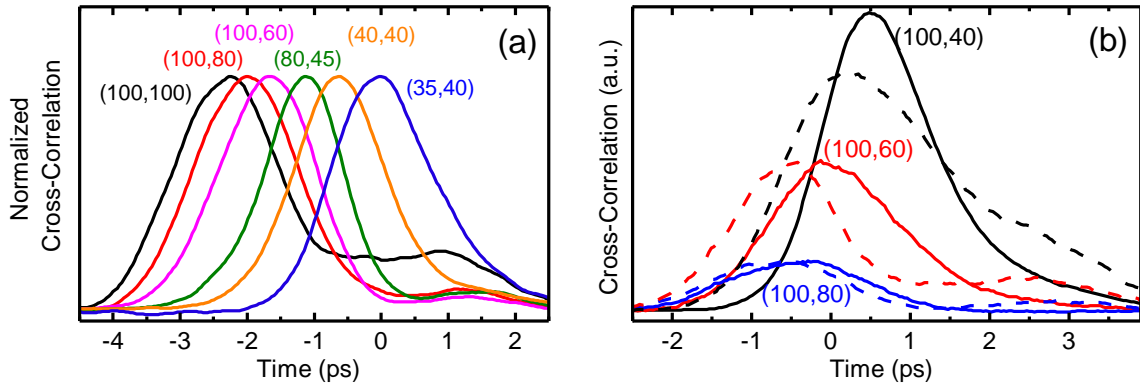


Figure 5.10(a). Normalized cross correlation traces of the pulse after it propagates through two SOAs. The bias currents applied to each of the amplifiers are indicated above the traces. At (100,80) the pulses are advanced by 2 ps, an ABP of 3.3 pulses (red curve). If the bias currents are increased to (100,100), the pulse advances by 2.7 ps (ABP = 3.75), but with significant distortion in the form of a “shelf” (black curve). Figure 5.10(b). Cross-correlation traces at  $(I_1, I_2)$  (solid lines) and  $(I_2, I_1)$  (dashed lines) for three different pairs of bias currents. The pairs of bias currents are not equivalent because spontaneous emission from the first SOA is injected into the second.

The improvement gained by using two devices is demonstrated by Figure 5.17(a), which shows the cross correlation traces for the cascade. Bias conditions are given by the ordered pair  $(I_1, I_2)$ , representing the bias currents of the first and second SOAs in milliamperes. An advance of 2.0 ps, corresponding to an ABP of 3.3 pulses, is obtained at (100,80) (red curve) with relatively little pulse distortion. As before, the depth of the spectral hole increases as the bias currents of the SOAs are increased, resulting in pulse

advance. Above a current of (100,80) the pulse begins to suffer from distortion in the form of a pedestal or “shelf” (black curve). The prevalence of this pedestal and the bias at which it appears are both strongly affected by adjusting the polarization controllers. This suggests again that distortion is the result of imperfect polarization control at the SOA input (all components in these experiments are fiber-coupled).

Figure 5.17(b) demonstrates that  $(I_1, I_2)$  is not equivalent to  $(I_2, I_1)$ . The most significant cause for this is that the first SOA injects spontaneous emission into the second, altering the gain spectrum. Another contribution may come from small differences between the SOAs or, due to the difficulty in controlling polarization in fiber, small differences in input polarization between the two devices. Finally, it should be noted that because SHB and CH effects are not linear, there is no *a priori* reason that the order in which two different “operations”, corresponding to propagation at the two different bias currents, should commute with each other. These measurements imply that several short SOAs in a cascade may offer opportunities for optimization that are not available in a single, long device.

### 5.3.5 SOA Loop

The increase in ABP from our initially measured value of only 2.5 pulses for a single SOA to 3.3 pulses for two devices demonstrates the viability of scaling ABP by cascading devices. However, as we increase the number of SOAs in the chain, the additional advance we get decreases due to spontaneous emission noise, spectral broadening and reshaping. These problems can be partially mitigated by including optical filters, attenuators and dispersion compensators between each optical amplifier. In order to

better understand these limitations, we propose a novel scheme that uses a single SOA in a loop configuration and simulates the effect of cascading multiple SOAs.

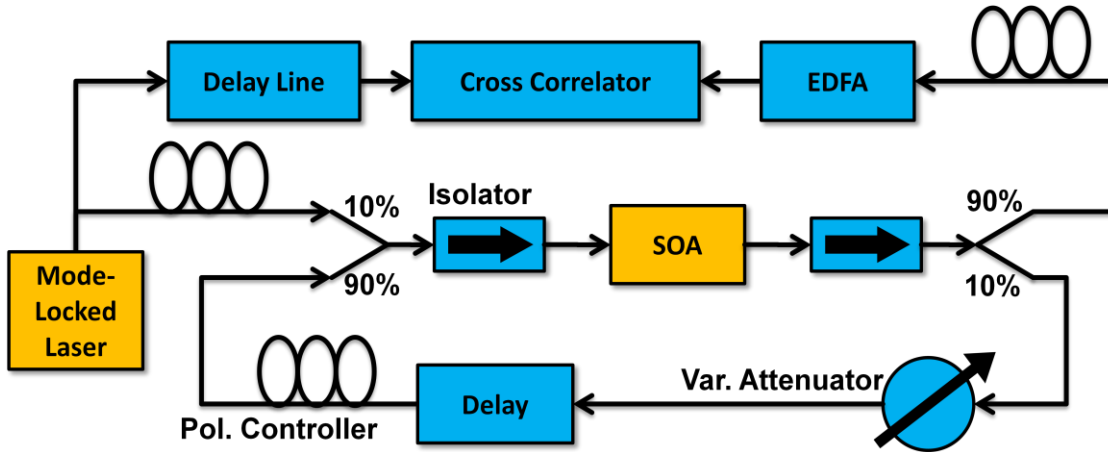
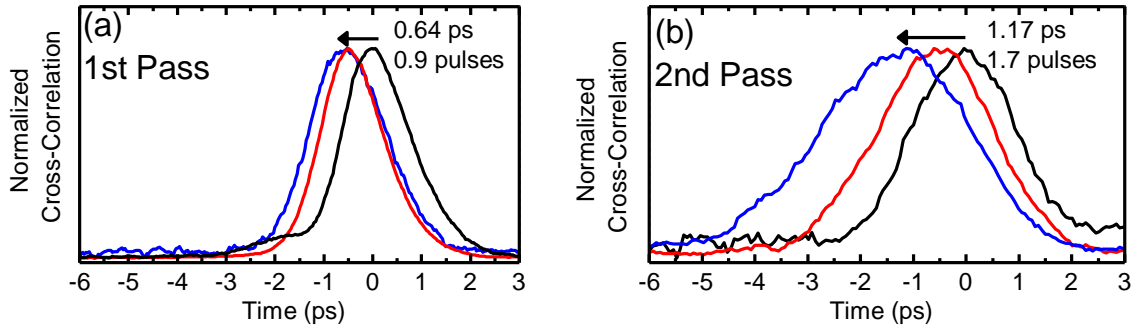


Figure 5.11. Novel experimental scheme to study the effect of cascading multiple SOAs. 10% of the SOA output is fed back into the input. By adjusting the time delay in the reference arm, we can selectively examine pulses that have gone through the SOA multiple times.

The experimental set-up for this scheme is shown in Figure 5.11. Similar to earlier set-up, the output from the fiber laser is split into reference and signal. At the SOA output, 10% of the signal is picked off, sent through an attenuator, a short delay (of a few ns), and a polarization controller, and then is re-injected into the SOA input via another 90/10 splitter. The attenuator prevents the SOA and loop from becoming a ring laser and ensures that the influence of the pulses will fade out and the SOA fully recover before the next pulse arrives from the laser. The result is that each pulse from the laser produces a set of output pulses of diminishing amplitude, each of which has passed through the SOA one more time than the pulse before it. Adjusting the delay line in the reference arm selects the pulse measured in the cross-correlator.



**Figure 5.12(a).** Cross-correlation traces of pulses which have passed through the SOA a single time. The bias is swept from 50 mA to 100 mA, advancing only 0.64 ps (ABP = 0.9). **Figure 5.12(b).** Cross-correlation traces after two passes through the SOA. The advance has almost doubled to 1.17 ps (ABP = 1.7), again demonstrating the scalability of the fast light scheme. The bias can only be swept over a limited range to prevent instabilities resulting from the onset of lasing.

The cross-correlation traces for a 700 fs pulse are shown in Figure 5.12. On Figure 5.12(a) are the traces for pulses which have passed through the SOA once. The bias current is only swept over a limited range (50 mA to 100 mA) so as to prevent instabilities which occur as the loop nears the threshold for lasing. An advance of 0.64 ps is achieved, an ABP of 0.9 pulses. For a pulse propagating through the SOA twice, Figure 5.12(b), the advance has increased to 1.17 ps, an ABP of 1.7. This doubling of advance is consistent with the earlier measurement using two cascaded SOAs. However, the ABP achieved by two passes through a single SOA remains lower than the ABP of 2.6 achieved in our initial results and much lower than the ABP of 3.3 achieved with a cascade. Also immediately noticeable is the broadening which has occurred between the first and second pass. This is due to the extra fiber in the loop (the polarization controller is also a fiber-based device).

Though the cascade initially performed better than the loop, this type of experiment can be prohibitively expensive for studying a long chain of  $N$  devices. Not only is it necessary to purchase or fabricate  $N$  SOAs, but  $N$  dispersion compensators, isolators,

filters, gain flatteners, etc. In this case the loop becomes the tool of choice, and there are many steps which can be taken to improve its performance. First, an optical bandpass filter can be used to remove a substantial amount of the spontaneous emission. Dispersion compensation can correct for pulse broadening after passing through the SOA. Switching to free-space further reduces pulse distortion and allows polarization optics to block still more spontaneous emission. With the cascade, individual sections can have their own bias, giving an extra degree of freedom in maximizing temporal shifting and minimizing distortion. This can even be replicated in the loop if the loop delay is long enough that the SOA bias can be changed between passes. Despite the increase in complexity, the loop configuration will be vital in investigating the scalability of intraband slow and fast light.

### 5.3.6 Multiple Pulses

First, we note that pulses in a bit stream will not allow the same recovery time as pulses from a 20 MHz or 25 MHz source. A higher repetition rate will lower the average carrier concentration in the SOA, so we expect that advance of a bit stream would require an increase in bias current to produce the same ABP. Because carrier recovery operates on a time scale much longer than our pulses, we do not expect any appreciable pattern dependence for data.

The present experimental repetition rate is limited by our instrumentation. However, a quirk in the operation of one of our older mode-locked lasers gives us an opportunity to begin to explore the issue of multiple pulses in rapid succession. The experimental setup is as presented in Figure 5.5. The laser produces pulses at a 25 MHz repetition

rate and with a FWHM (assuming  $\text{sech}^2$  pulse) at the SOA input of 630 fs. The SOA is a free-space coupled chip-on-carrier device, allowing both precise control of polarization and better coupling. The coupling is so good that at higher SOA bias currents we can observe a “pre-pulse” emitted from the laser before the main pulse. The cross correlation traces showing both the pre-pulse and the main pulse are shown in Figure 5.13(a). The pre-pulse is normally negligible relative to the main pulse, but in this case enough of it is coupled into the SOA that it is amplified to significant levels.

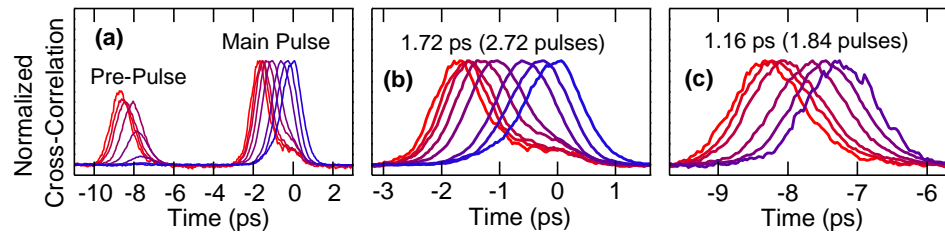


**Figure 5.13(a).** At high SOA gain, a small pre-pulse from the laser is amplified significantly. The pre-pulse arrives 7.2 ps before the main pulse. Trace amplitudes are normalized to the main pulse. **Figure 5.13(b).** Advance of main pulse as SOA bias is increased from near transparency to maximum. The pulse advances by 1.72 ps (DBP = 2.7). **Figure 5.13(c).** Advance of pre-pulse as SOA bias is swept from near transparency to maximum. The pre-pulse experiences advance similar to the main pulse. The total advance of 1.16 ps (DBP = 1.8) is smaller than the main pulse due to the lower power.

This SOA offers significant improvement over the DBP of 2.5 reported in our initial experiments with the fiber-coupled SOAs. In Figure 5.13(b), cross-correlation traces show the pulse advancing by 1.72 ps (ABP = 2.7) when the SOA current is varied from near transparency to maximum. This advance is achieved despite any depletion of carriers due to the amplification pre-pulse.

The pre-pulse arrives 7 ps before the main pulse. Figure 5.13(c) shows the advance of the pre-pulse (1.16 ps, ABP of 1.8). The advance is lower than the main pulse for two reasons. First, the pre-pulse must be amplified to a point where it can participate in the nonlinear effects of CHB and CH, which means that it can only experience these effects

in the latter part of the SOA. Second, because of the limited signal-to-noise ratio of our equipment the pre-pulse is undetectable near the lower range of SOA bias currents, yielding an incomplete picture of the total advance. Nevertheless, these results are an important step towards demonstrating that intraband effects can delay or advance groups of closely spaced pulses, as would be found in a data stream. The 7 ps spacing between the two pulses corresponds to a bit rate of 140 Gbps.

### 5.3.7 Polarization

As mentioned in the previous sections, the amount of advance achieved and the quality of the pulses are sensitive to the settings of the polarization controllers, despite the polarization insensitivity of the small signal gain of the SOAs under test. However, quantum wells are inherently asymmetric structures; it may be that important intraband parameters like the carrier-carrier and carrier-phonon scattering times are still polarization dependent. However, a study of this dependence cannot be made with a fiber-coupled device. Also, the polarization controllers function as wave plates by using strain-induced birefringence. Dispersion associated with the strain may be distorting the pulse in unpredictable ways. This idea is supported by the dependence of the pulse shape and advance on the *output* polarization controller.

It is clear that clean polarization control over broad wavelength ranges requires free-space components. With this in mind, we purchased a chip-on-carrier SOA suitable for polarization studies. This high-confinement, high gain device is designed to enhance optical nonlinearities and has a fast (25 ps) gain recovery. Using a CW DFB laser we measure the gain for TE and TM polarizations as a function of SOA bias current (Figure

5.14), where “TE” defines an electric field in-plane with the quantum well. The gain for the TM polarization is about 2 dB higher than that of the TE polarization.

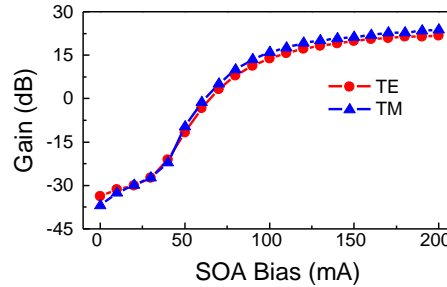


Figure 5.14. Gain for TE and TM polarization as a function of SOA bias current. The input for these measurements was a CW DFB laser, attenuated to -35 dBm. Gain for the TM polarization is slightly higher (2dB) than that of the TE polarization.

We study the effect of polarization on slow and fast light using the setup shown in Figure 5.15, a modification of the basic cross-correlation setup shown in Figure 5.5. The mode-locked laser used generates 630 fs pulses (FWHM, assuming  $\text{sech}^2$  pulse shapes) at a 25 MHz repetition rate. The signal arm is coupled to free space immediately after splitting from the reference. The input polarization controls consist of a quarter wave plate and a half wave plate, followed by a polarizer. The signal is coupled back to fiber after the output polarization controller, immediately before the EDFA.

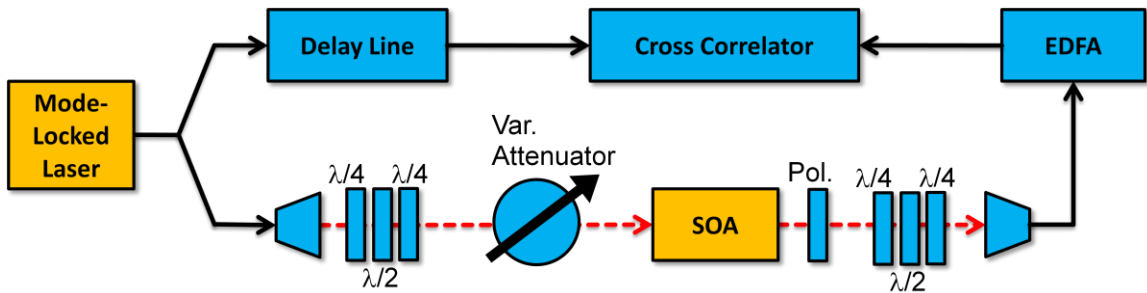


Figure 5.15. Experimental setup for free-space SOA. The principles of operation are identical to Figure 5.5, except that the fiber-based polarization controllers, attenuator, and SOA have been replaced with free-space components.

We first study the TM polarized input, shown in Figure 5.16(a). The SOA bias is swept from slightly below transparency (slow light regime) to maximum (fast light regime). The

total advance is 1.49 ps, corresponding to an ABP of 2.3 pulses. Next, we measure the TE polarized input for the same SOA bias conditions, shown in Figure 5.16(b), and measure a total advance of 1.72 ps, or 2.7 pulses. The higher ABP of the TE polarization, despite the slightly lower overall small signal gain, is an interesting result that underscores the importance of other parameters, such as the selection rules for the polarizations. First, there are the waveguide parameters; the “background” group velocity is likely to be different for the different modes. On a material level, TM and TE polarizations access different transitions between the conduction and valence bands. By conducting polarization experiments on SOAs which have not been designed for polarization independence, it may be possible to glean greater insight into the effect of band structure on intraband slow and fast light.

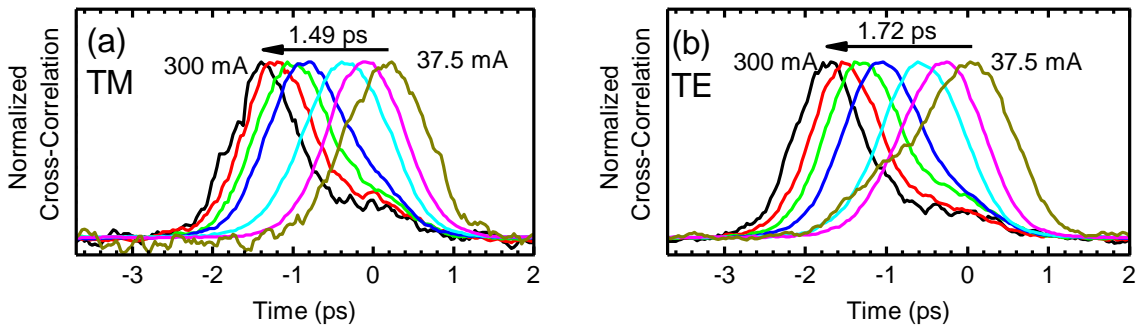
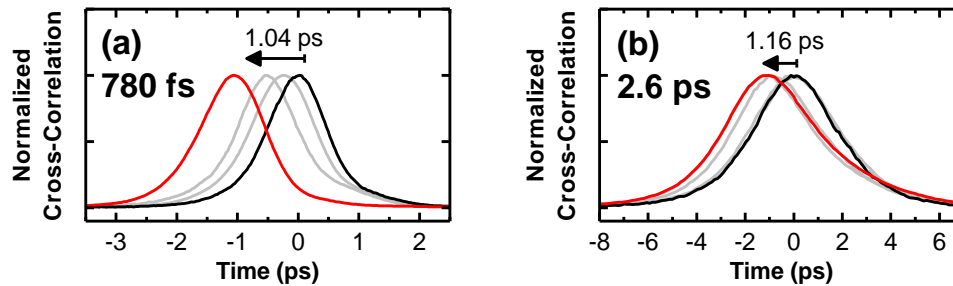


Figure 5.16(a). Cross-correlation traces for TM polarized input (perpendicular to plane of quantum well) as bias current is swept from slightly below transparency to maximum. The 1.49 ps advance corresponds to an ABP of 2.3. Figure 5.16(b). Cross-correlation traces for TE polarized input. The 1.72 ps advance corresponds to an ABP of 2.7 pulses. The small signal gain of the TE polarization is slightly lower than the TM, so the increase in ABP indicates the importance of other parameters, e.g. different selection rules for different polarizations.

### 5.3.8 Pulse duration

The duration of the pulse should have a significant impact on the amount of delay or advance which can be obtained. For a long pulse, the carrier population is subjected to an adiabatically changing field, and the rate equation model is applicable, i.e. there will

be no contributions from intraband effects. Thus, as the pulse becomes longer than the SHB and CH lifetimes, we do not expect to observe large ABP. Our mode-locked laser allows the duration of the output pulses to be tuned while remaining nearly transform limited. In the following, we use this capability and the experimental setup shown in Figure 5.15 to study the effect of pulse duration on the advance. Later, In Section 5.4 we will explore the effects of expanding the pulses in a non-transform limited fashion, i.e. by adding chirp.



**Figure 5.17. Normalized cross-correlation traces of the output pulses as SOA bias is swept from near transparency (black curve) to high gain (red curve), for two different pulse durations. Pulse durations were swept by tuning the mode-locked laser, producing nearly transform limited pulses. Figure 5.17(a). Input pulse has duration of 780 fs (FWHM) and shows an advance of 1.04 ps (ABP of 1.34). Figure 5.17(b). Input pulse has a FWHM of 2.6 ps (note change in time scale!) and shows an advance of 1.16 ps (ABP of 0.44).**

The general trend we discover is that the ABP decreases as the pulse duration increases. Representative cross-correlation traces are shown in Figure 5.17 for pulse duration of 780 fs (Figure 5.17(a) ) and 2.6 ps (Figure 5.17(b) ). For the 780 fs pulse the ABP is 1.34 pulses, whereas for the 2.6 ps pulse the ABP has dropped to 0.44 ps. This follows a general trend of slightly increasing advance and sharply decreasing ABP with increasing pulse width. Figure 5.18 summarizes these results. The very small increase in advance due to a lower bandwidth pulse (Figure 5.18(a) ) is less than the increase in pulse duration, so the ABP decreases (Figure 5.18(b) ). Recall (Table 5.1) that the measured SHB and CH recovery times are 0.83 ps and 3.3 ps, respectively. On Figure

5.18(b) there is a kink in the trend near 0.83 ps. Our laser cannot produce transform limited pulses beyond 3 ps, and so were not able to investigate the behavior of the ABP beyond the CH recovery time.

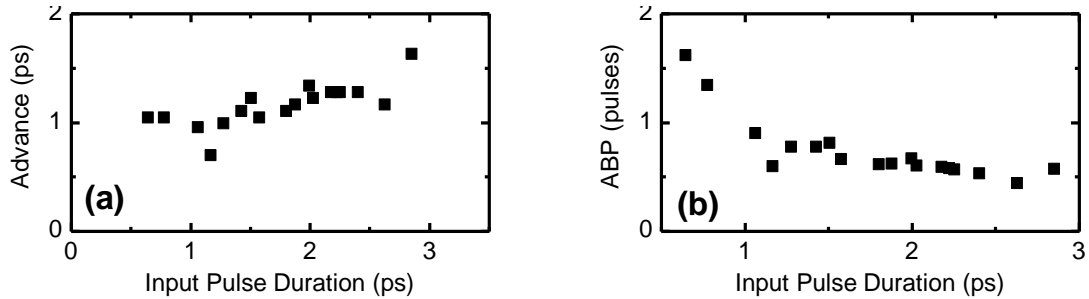


Figure 5.18(a). Effect of pulse duration on net advance achieved by sweeping SOA current from transparency to maximum. As the pulse duration increases, net advance increases slightly. Figure 5.18(b). ABP vs. pulse duration. For this SOA, the measured spectral hole burning and carrier heating recovery time are 0.83 ps and 3.3 ps, respectively. Despite the slight increase in net advance, the ABP drops as pulse duration increases beyond these times and intraband effects no longer contribute to pulse advance.

## 5.4 TWDM: Chirped Input Pulses

### 5.4.1 Motivation and Theory

The work presented in this Section was primarily motivated by the data shown on Figure 5.7(a). The ABP increases rapidly at low currents, but then begins to saturate. This is due to the inability of the pulse to burn a hole deeper than transparency. If the intensity of the pulse continues to increase, the hole begins to widen instead.

At low gain, the pulse is amplified as it propagates, the hole deepens, and the advance per unit length increases along the device. At higher gain, the hole gets burned to transparency and then begins to widen. As the pulse propagates beyond this saturation point, the advance per unit length begins decreasing; the extra distance is contribution less and less to the advance. As the gain is increased further, the saturation

point happens earlier and earlier in the pulse propagation and the extra gain does less and less to provide advance to the pulse.

To mitigate this problem, we propose a novel scheme which we refer to as time-wavelength division multiplexing (TWDM). We impose a linear GVD or “chirp” upon the pulse before it enters the SOA. This stretches the pulse duration and causes different spectral components to enter the SOA at different times. Each spectral component can now burn a hole in a different part of the SOA gain spectrum, delaying the onset of the saturation point. At the output of the SOA, chirp of the opposite sign is applied, recompressing the pulse. The recompressed pulse now has a larger ABP.

#### 5.4.2 Chirper Experiments

Figure 5.19 shows our experimental setup for TWDM. It is similar to the basic setup shown in Figure 5.5, except for the addition of the chirper and compensator. The chirper and compensator consist of grating pairs which add or remove a linear chirp to the pulse while leaving its spectrum unaltered [68,67]; thereby stretching or compressing the pulses in time. After stretching or “chirping out,” the pulses are no longer transform limited since they retain their original bandwidth. The chirpers can be switched into or out of the optical path at will. For now, we will discuss the case where the chirper provides negative chirp (so that blue components of the pulse enter the SOA first) and the compensator provides positive chirp. The opposite case will be discussed in the next section.

For these experiments the free space SOA described in Section 5.3.7 was used along with the variable pulse width laser. After the split between the signal and reference

arms, the signal pulses are coupled to the chirper via a fiber circulator. After the circulator, the beam is coupled to free space. A variable attenuator is used to maintain the same pulse energy at the SOA input throughout all experiments, approximately 0.23 pJ. After the SOA the signal is coupled back into fiber, where a second circulator directs it into the compensator. The compensator provides linear chirp in the opposite sense of the chirper, thereby re-compressing the pulse. Additional polarization controls are required throughout the signal path due to the polarization sensitivity of the gratings, the SOA, the EDFA, and the cross-correlator.

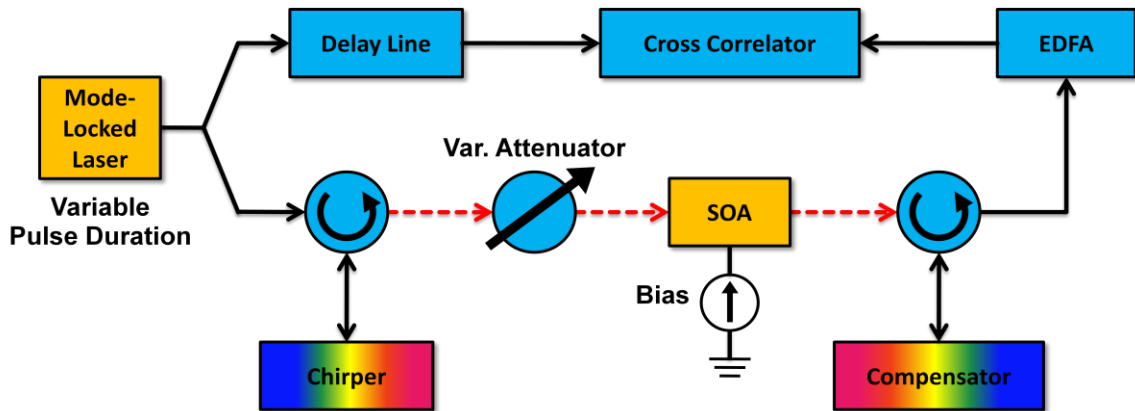
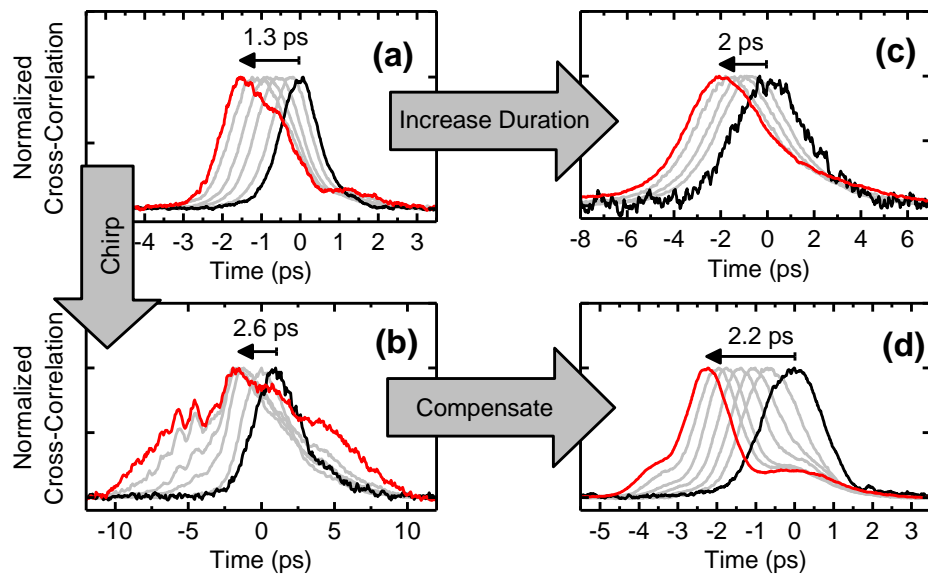


Figure 5.19. Experimental setup for chirped pulse measurements. The principle of operation is similar to the setup shown in Figure 5.5. The chirper adds a chirp to the pulse, stretching it in time and leaving the spectral width unchanged. The compensator applies the opposite chirp, recompressing the pulse. Black lines represent optical fiber, red lines are free-space.

A set of four different experiments were conducted. Each experiment consisted of sweeping the SOA bias current, taking cross-correlation traces, and measuring the ABP. First, both the chirper and compensator were bypassed and measurements were taken with a fast (700 fs) pulse. These pulses emerge from the fiber laser nearly transform-limited and we refer to them as “unchirped” pulses. Next, the chirper was used to stretch the 700 fs pulse to 2.68 ps and the ABP was measured. Then, for comparison purposes, the chirper and compensator were both removed again and measurements

were taken for a slow (2.68 ps) unchirped pulse (obtained by adjusting the laser), of the same duration as the chirped pulse. Finally both the chirper and compensator were employed to chirp the 700 fs pulse, advance the pulse with the SOA, and then recompress the pulse again – the full TWDM scheme. The variable attenuator was used to maintain the same pulse energy at the SOA input throughout all these experiments, approximately 0.23 pJ.



**Figure 5.20.** Cross-correlation traces from the TWDM experiments. Figure 5.20(a) shows the advance of a transform limited 700 fs pulse. Figure 5.20(b) shows the advance of the same pulse after it has been chirped out to 2.6 ps. The pulse suffers severe distortion. Figure 5.20(c) shows the advance of a transform limited 2.6 ps pulse. The advance is larger than that of the 700 fs pulse, but the ABP is smaller. In Figure 5.20(d) the chirped pulse of (b) has been recompressed after propagating through the SOA. This TWDM pulse has both a large advance and a large ABP while the distortion has been mitigated.

Figure 5.21 summarizes these results by plotting net advance vs. SOA bias current (Figure 5.21(a)) and ABP vs. SOA bias (Figure 5.21(b)) for the original pulse, the chirped pulse, and the chirped and compensated pulse. The advance of the chirped pulse rises faster with increasing bias and saturates at a higher value than the advance of the original pulse. The compensated pulse enjoys both the large advance of the chirped pulse and the short duration of the original pulse, yielding a large ABP.

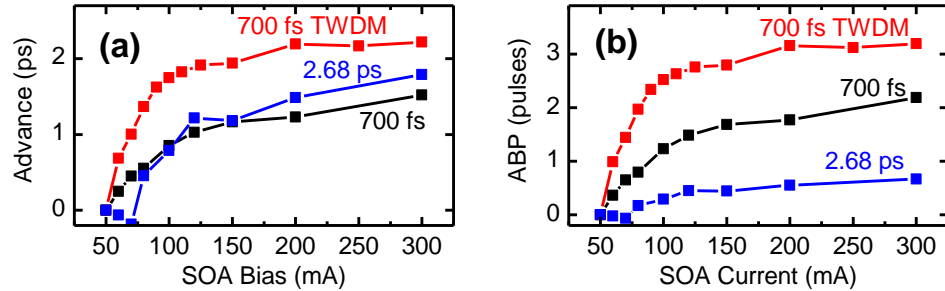


Figure 5.21(a). Advance vs. SOA bias for 700 fs (black) and 2.68 ps (blue) unchirped pulses and for the chirped and compensated TWDM pulse (red). Advance saturates in a similar fashion for both transform-limited pulses, but the TWDM pulse has a higher ceiling. Figure 5.21(b) shows ABP vs SOA bias. ABP also saturates with increasing SOA current. Different spectral components of the TWDM pulse enter the SOA at different times, allowing more efficient use of the SOA gain spectrum, and an increase of ABP to 3.14.

The study presented above illustrates the benefits of the TWDM technique. However, Figure 5.20(d) shows some distortion of the pulse in the form of a pedestal. Also, the pulses have broadened in comparison with the original, unchirped pulses shown on Figure 5.20(a), even when the SOA is biased near transparency. This is due to mismatch between the chirper and compensator and is not inherent in the TWDM scheme. Further optimization of the chirper-compensator pair allowed the use of faster input pulses, larger amounts of chirp, and the elimination of pulse broadening. Figure 5.21 shows the result of such an effort. Figure 5.22(a) shows the auto-correlation at the input of the chirper. The FWHM is 500 fs while the RMS width (see Appendix) is 320 fs. The chirper expands the pulse nearly 10 times to 4.7 ps. Figure 5.22(b) shows the cross correlation traces after the SOA and counter-chirper. The advance in this case is 1.76 ps, or 3.5 pulses. The RMS width of the output pulses is maximum near the lowest bias (434 fs, 33% broadening).

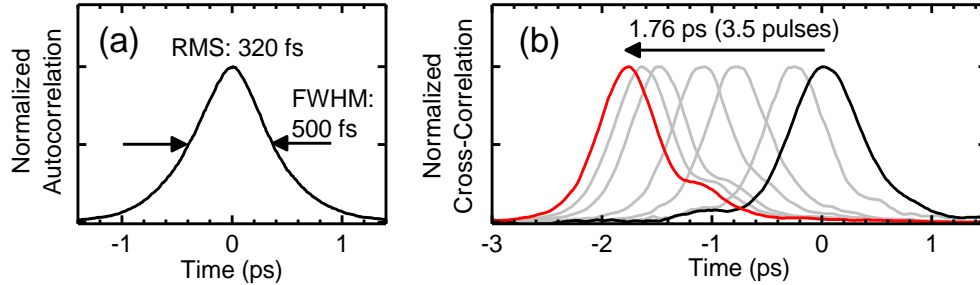


Figure 5.22. Compensator optimized for better re-compression of pulses at SOA output. Figure 5.22(a) shows the auto-correlation of the input pulse. The broadening of the reference pulse is nearly negligible in these experiments, so the auto-correlation can be directly compared to the cross-correlation traces of the compensated pulses, Figure 5.22(b). The improved compensation leaves the pulse widths almost unchanged. A small pedestal is still visible, less than 28% of the peak height.

The cross-correlation traces in Figure 5.22(b) still exhibit a small pedestal, the height of which is always less than 28% of the peak. The height and position of the pedestal relative to the peak are strongly affected by the polarization controls before and after the SOA. Because the peak power is very high in such a short pulse (about 1.4 W in these experiments) even a small fraction of pulse energy coupled into the orthogonal TM mode of the SOA can be easily amplified to a point where carrier dynamics are significantly affected. Additionally this orthogonally polarized pulse will experience different waveguide dispersion, propagating either ahead of or behind the main pulse, and will interact with the carrier population differently due to general anisotropy of a quantum well structure. Hence, the pedestal is attributed to an artifact of imperfect polarization control and can be corrected in future experiments.

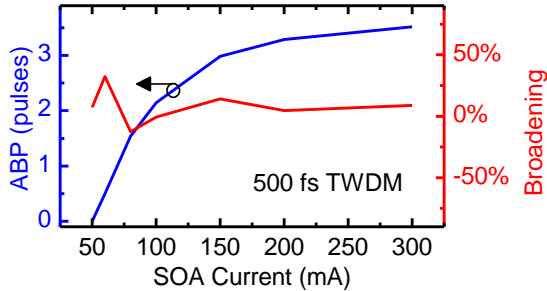


Figure 5.23. ABP and broadening (relative to the input pulse) of 500 fs TWDM. Chirper and counter-chirper have been optimized for minimal broadening and ABP of 3.5. Average broadening is 8% and never exceeds 33%.

Figure 5.23 summarizes the results from the 500 fs input pulse with improved matching between the chirper and compensator. Here, the pulse broadening, calculated from RMS pulse widths, is overlaid on top of the ABP. The ABP reaches 3.5 at maximum SOA current. The broadening is less than 9% for the majority of the operating regime. We expect considerable improvement if a 200 fs pulse is chirped out to 700 fs, where the ABP of the unchirped pulses is higher.

### 5.4.3 Negative Chirp and Delay

All of the preceding experiments were performed with a negatively chirped pulse entering the SOA, i.e. blue spectral components enter the SOA first. In this section, we investigate the effect of positive chirp. Note that the sign of the compensator is reversed as well, so that the compensator still recompresses the pulse. In this configuration, it is the red spectral components that enter the SOA first. As before, the chirper stretches the input pulse, for this study from 0.44 ps to 4.37 ps. Figure 5.24(a) shows the cross correlation traces after the pulse has been recompressed by the compensator. As the bias current is increased, the pulse is *delayed* instead of advanced. Up to 1.31 ps (DBP = 3.0) of delay is achieved as the SOA current is increased from transparency to 300 mA.

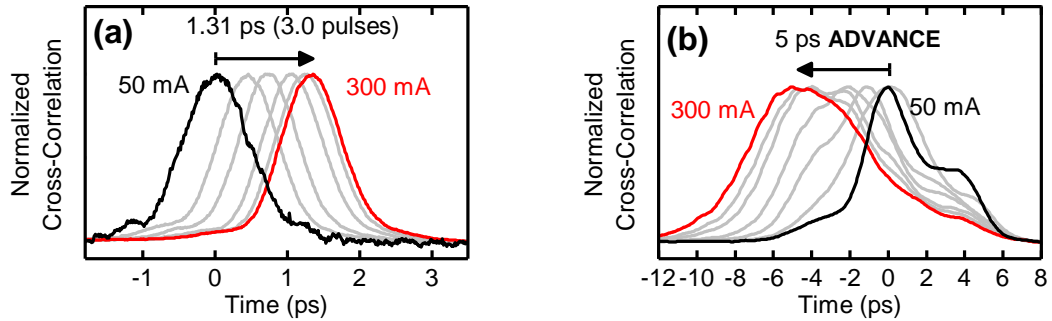


Figure 5.24(a). Cross-correlation traces of a positively chirped (red enters SOA first) and then compensated pulse. For this chirp a *delay* is observed with increasing current (1.31 ps, DBP = 3.0). Figure 5.24(b). Cross-correlation traces as in (a) but *without* compensator. Pulses experience *advance* of 5 ps with increasing bias current.

These results are somewhat shocking. The order in which the spectral components enter the SOA should not change a hole in gain into a peak. Figure 5.24(b) shows cross-correlation traces before the compensator. As expected, the pulses are broad and there is some distortion present. But the pulses are clearly seen to be *advancing*, by 5 ps, as SOA current is increased. This points to the recompression of the pulse as the cause of the delay. Figure 5.25(a) shows crude spectra of the input and output pulses for three different bias currents and provides the final piece of information required to explain the delay. These spectra were taken by sweeping an optical filter and measuring the amplitude of the impulse response of a fast detector. This is necessary to separate the spectrum of the pulse from that of the spontaneous emission (although the pulse intensity is much larger than the spontaneous emission, the pulse only occupies 0.002% of the pulse train period). From these measurements the wavelength of the pulse is seen to red-shift by more than 10 nm with increasing bias. The compensator recompresses the pulse by delaying red components, so a net red-shift leads to a net delay of the pulse. The wavelength shift is caused by the red spectral components entering the SOA first and receiving the highest amplification. The red leading edge of

the pulse depletes carriers, leaving less available for amplification of the blue components and resulting in a red-shift.

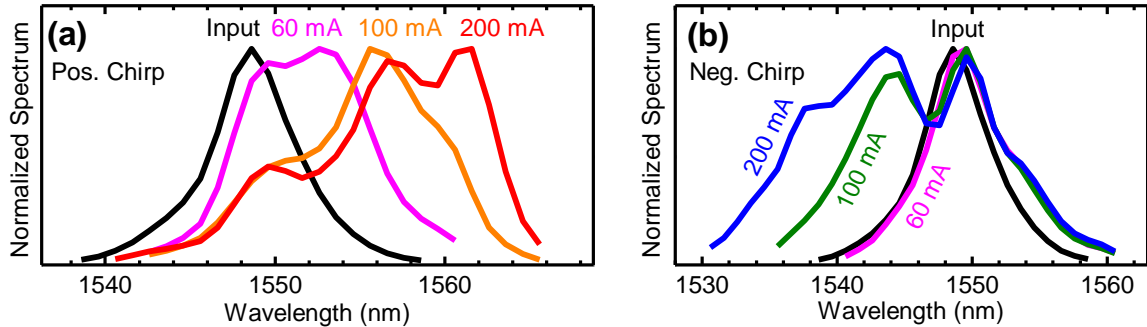


Figure 5.25(a). Crude spectra of input and output pulses with positive chirp (red enters SOA first) at three SOA bias currents. The wavelength of the pulses red-shifts by 10 nm with increasing bias. The compensator recompresses the pulse by delaying the red components relative to the blue; the net red-shift causes a net delay. Figure 5.25(b). Similar spectra for the negatively chirped pulses (blue enters SOA first). In this case, the pulses blue-shift by 6 nm, but now the compensator delays blue, again resulting in a delay. A net advance is observed for positively chirped pulses is observed because the wavelength shift, and hence delay, is not as large.

The question immediately arises: is the advance of negatively chirped pulses described earlier also due to a wavelength shift? Figure 5.25(b) shows the pulse spectrum at the output for a negatively chirped pulse. In this case the spectrum blue-shifts by 6 nm; as before, this is due to blue components entering the SOA first and getting preferentially amplified. But in this configuration, the compensator recompresses the pulse by delaying the *blue* components, and the net effect of the wavelength shift is a *delay*. The implication of this is that the 3.5 pulse advance (Figure 5.22(b)) discussed earlier is in spite of the delay from the wavelength shift. For negatively chirped pulses the advance dominates the delay because the wavelength shift is only 6 nm. We expect that the intraband effects are yielding a larger advance than what we actually measure.

The larger red-shift and the “rippled” appearance of the spectrum can both be explained by self phase modulation (SPM). Interband SPM [70,69] is the change in phase as a function of carrier density due to the linewidth enhancement parameter. Unlike the grating-based chirper and compensator, which leave the spectrum unmodified but stretch the pulse in time, SPM imposes a negative chirp on the pulse by red-shifting the spectrum. When the chirper positively chirps the pulse, red components enter the SOA first and are preferentially amplified, red-shifting the pulse. The interband SPM then red-shifts the spectrum further. In contrast, if the input pulse is negatively chirped then preferential amplification shifts the wavelength blue, working against the red-shift of the SPM. This is why the red-shift for the positively chirped pulses is larger than the blue shift for the negatively chirped pulses. The multi-peaked appearance of the spectrum, despite the relatively undistorted appearance of the pulse, is a general feature of SPM [70].

#### 5.4.4 Maximizing Delay and Advance

Figure 5.26 shows a schematic for a novel scheme to obtain both delay and advance from a single SOA and two chirpers. When the two  $2 \times 2$  crossbar switches are in the bar state light is negatively chirped before entering the SOA. The pulses can then be continuously advanced by increasing SOA bias. After the SOA the pulses are recompressed with a positive chirp. When the switches are in the cross state light is positively chirped before entering the SOA, allowing the pulses to be delayed by increasing bias current. They are then recompressed by a negative chirp. The second crossbar switch is required because the SOA is not bi-directional.

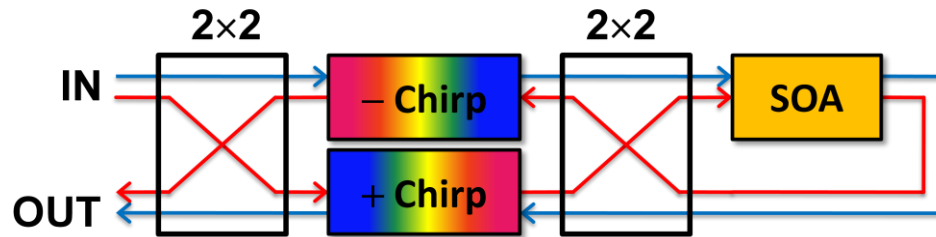


Figure 5.26. A novel scheme to use both the delay and advance obtainable by TWDM. When the 2x2 crossbar switches are in the bar state, pulses are negatively chirped, advanced by the SOA, and then recompressed with a positive chirp (blue line). When the switches are crossed, the pulses are positively chirped, delayed, and then recompressed with a negative chirp (red line).

Next, we study the delay or advance as a function of chirp. Because an unchirped pulse has already been shown to advance with increasing bias current then we expect to see a transition from advance to delay at some finite value of positive chirp. These results are shown in Figure 5.27. We quantify the chirp of the input pulse with the dispersion parameter  $D$ , defined as the broadening of a pulse divided by the spectral width in nanometers. Note that  $D > 0$  corresponds to negative chirp. As seen from the figure, a 440 fs pulse chirped to 6 times ( $D = -0.9$ ) gives 0.7 pulses delay while a pulse chirped only 3 times ( $D = -0.43$ ) gives 0.9 pulse advance showing a smooth transition from delay to advance.

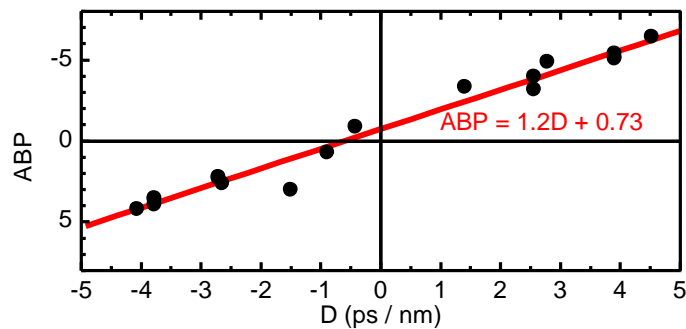


Figure 5.27. ABP as a function of the dispersion  $D$  of the input chirper. The parameter  $D$  gives the spread of the pulse per unit pulse bandwidth (ps/nm) and is a standard way to quantify GVD. Note that  $D > 0$  represents a *negative* chirp, and a pulse advance. The transition from advance to delay occurs at  $D = -0.61$ . This is the point where the delay due to wavelength shift equals the advance from intraband fast light effects.

The largest combination of delay and advance measured at the time of this publication is an A/DBP of 10.7 pulses, representing the leftmost and rightmost points on Figure 5.27. Cross-correlation traces for these data points are shown in Figure 5.28. For this experiment, the original pulse with a duration of 370 fs is chirped out 35 times to 13 ps. At this point the chirper and compensator are pushing the limits of their designed capabilities and therefore are no longer able to stretch and recompress the pulses without distortion. Also, the experimental setup at this point is all free-space *except* for the chirper and compensator, which each have large amounts of fiber in the form of long pigtails on the circulators (see Figure 5.19). We are currently in the process of improving upon these results in two ways. First, we are building new chirpers without fiber and designed to provide larger amounts of GVD. Second, we are building a non-linear pulse compressor so that we may begin with a still faster initial pulse [72,71]. Our goal is to chirp a sub-100 fs out to tens of picoseconds and to realize an A/DBP of approximately 80.

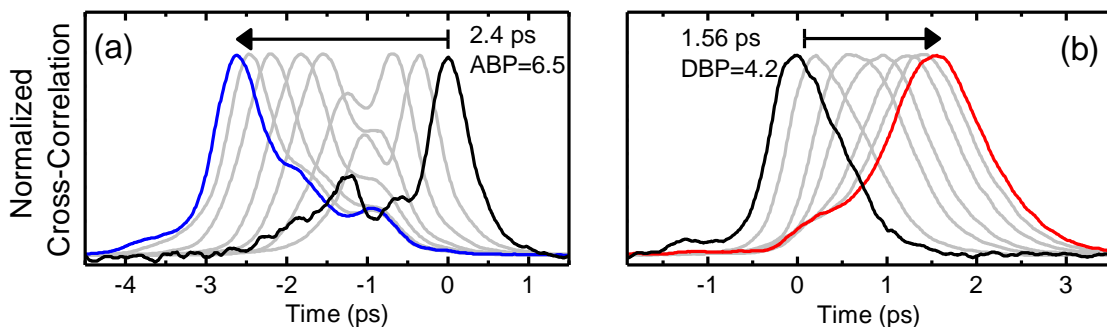


Figure 5.28(a). Cross-correlation traces with negative chirp (blue enters SOA first) showing 2.4 ps advance (ABP = 6.5). Figure 5.28(b). Cross-correlation traces with positive chirp, demonstrating 1.56 ps delay (DBP = 4.2). In both cases the original pulse of duration 370 fs is chirped out to 13 ps. These large chirps operate at the limits of our current chirper design and the chirper and compensator are unable to stretch and compress the pulses without distortion.

## 5.5 Theory and Simulation

We now turn to the task of developing a more quantitative theory describing the delay and advance of sub-picosecond pulses. We begin the chapter with a look at some well-established physical mechanisms by which a pulse may be delayed or advanced. We demonstrate that these mechanisms alone cannot account for the large pulse shifts which we have measured. Next we outline a model of sub-picosecond pulse propagation based on a density matrix treatment which moves beyond the adiabatic approximation. From this treatment we show that there are corrections to group index which arise not only from the SHB hole, but from dynamical effects as well.

### 5.5.1 Well-Known Effects

The first, and perhaps simplest, possible explanation for the observed pulse shift is the change in refractive index due to the change in carrier density. As mentioned in Section 4.2 in our discussion of the linewidth enhancement parameter, injection or depletion of carriers can significantly alter the refractive index of an SOA. Assuming a device length of approximately 1 mm, an advance of 1.5 ps would require a change in refractive index of 0.22, which is much larger than is possible via this mechanism. A related possibility is the group index associated with the spectral dispersion of the gain peak itself. For a Lorentzian peak of height  $\Delta g$  and FWHM  $\Delta\omega$  the Kramers-Kronig relations predict a group  $\Delta v_g$  velocity at the center of (see Eq. (1.21) )

$$v_g^{-1} = \frac{\omega}{c} \cdot \frac{dn}{d\omega} = \frac{1}{2\pi} \cdot \frac{\Delta g}{\Delta\omega} \quad 5.14$$

For a device of length  $L$ , the pulse advance is

$$T_{adv} = \frac{L}{v_g} = \frac{L}{2\pi} \cdot \frac{\Delta g L}{\Delta \omega} \quad 5.15$$

Based on measurements of CW gain at 1.55  $\mu\text{m}$  and on ASE spectra, we estimate the gain peak to be wider than 4 THz FWHM, which implies the gain peak would need to be over 200 dB to explain the observed advance. Obviously the gain peak of the SOA is not a Lorentzian, but the order of magnitude of our estimate makes the gain peak a very unlikely source of the observed advance.

It is also possible that a pulse can be made to advance due to gain saturation [70]. The leading edge of the pulse is amplified, depletes the carriers, and leaves less gain for the trailing edge. This effect is shown in Figure 5.29 (red curve), where we have numerically simulated the advance of a 700 fs  $\text{sech}^2$  pulse due to interband gain saturation. For this case intraband effects are neglected and the semiconductor is modeled as a saturable two-level system. Under these assumptions the pulse can be advanced by an unlimited amount given an unlimited amount of saturable gain. Limiting the small signal gain to a reasonable value of 30 dB, the pulse advances by 0.53 ps, an ABP of only 0.75, which is short of the 2.5 pulses measured in our experiments.

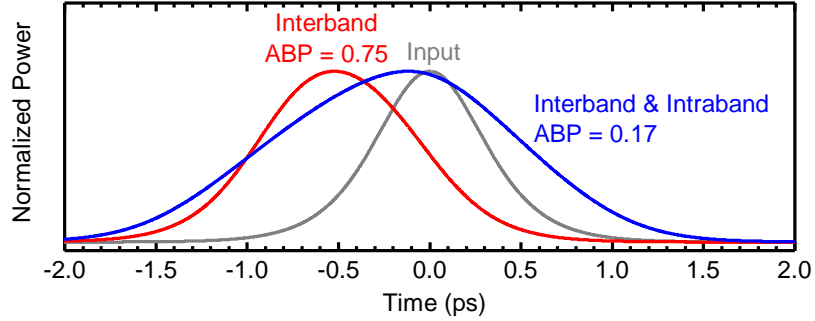


Figure 5.29. Numerical simulation of pulse advance due to gain saturation for a 700 fs input pulse. A pulse propagating with no saturation (e.g. when SOA is biased at transparency) is identical to the input (shown in grey for reference). First, we include only interband gain saturation (red curve), i.e. the semiconductor is modeled as a two-level system. The leading edge of the pulse is amplified, depletes carriers, and leaves the trailing diminished, resulting in a net advance. Next we include additional suppression due to intraband effects (blue curve). Note that this is only including the reduction of gain due to these effects, not any contribution of group index. The advance is actually reduced when these effects are included. In neither case does the pulse obtain an ABP of 2.5 as measured in experiment.

Intraband effects can be included in this simple model using a phenomenological gain suppression factor  $\epsilon$ . This factor modifies the gain to become an explicit function of photon density  $S$  [40,39,38]

$$g(N, S) = \frac{g_0(N)}{(1 + \epsilon S)} \quad 5.16$$

where  $g_0(N)$  is the gain calculated from carrier density  $N$  (also called “linear” gain). Note that this model includes SHB and CH only as mechanisms that instantaneously suppress gain, and does not include any effects they may have on the pulse spectrum or group velocity. The blue curve in Figure 5.29 adds the intraband gain suppression to the interband gain saturation. Near the base of the pulse, where photon density is low, the intraband effects increase the advance of the pulse slightly, but for the majority of the pulse the advance is suppressed. The peak advances by merely 120 fs (ABP = 0.17). The intraband suppression decreases the amplitude of the pulse, which inhibits the ability of the leading edge and peak to deplete carriers and advance the pulse.

Pulse reshaping via gain saturation is an example of one way a nonlinear response may induce a temporal shift. A simple analysis in [73] demonstrates a shift in pulse peak due to the amplification of the leading edge relative to the trailing edge. However, as the authors pointed out, their basic model cannot account for a fractional delay of more than approximately 50%, as no amount of pulse reshaping can cause the peak to shift outside of the original pulse. That model is based on the assumption that pulse duration is much shorter than the carrier lifetime, but much longer than carrier-carrier scattering times. Their approximation neglects any pulse-induced change in the carrier distribution which may give rise to a spectral hole and subsequent group velocity effects.

### 5.5.2 Nonlinear Group Index

We begin by modeling the semiconductor as an ensemble of two-level systems. The state of the  $k^{\text{th}}$  two-level system is given by the conduction band occupation  $\rho_{ck}$ , the valence band occupation  $\rho_{vk}$ , and the coherence  $\sigma_k$  (the “slowly varying” amplitude of the off-diagonal elements under the rotating wave approximation), from which the expectation value of the dipole moment may be calculated and hence, the susceptibility. Note that  $\rho_{ck}$  and  $\rho_{vk}$  are the occupations for an electron and a hole, respectively, and therefore the inversion is given by  $\rho_{ck} + \rho_{vk} - 1$ .

The equations of motion for the occupations  $\rho_{xk}$  ( $x = c, v$ ) are

$$\frac{\partial \rho_{xk}}{\partial t} = -\frac{i}{\hbar} \mu_k E (\rho_{xk} - \rho_{xk}^*) - \frac{\rho_{xk} - f_{xk}^T(t)}{\tau_{1x}} - \frac{\rho_{xk} - f_{xk}^L(t)}{\tau_{hx}} - \frac{\rho_{xk} - f_{xk}^0}{\tau_s}. \quad 5.17$$

The first term on the RHS of Eq. (5.17) describes stimulated emission and absorption, where  $\mu_k$  is the dipole matrix element between the conduction band and valence band

states. The second term describes the relaxation of the carrier distribution to a Fermi distribution of a carrier temperature  $T_x(t)$ , where  $\tau_{1x}$  is the phenomenological lifetime associated with carrier-carrier scattering. SHB effects are due to this term. The third term is the CH term and describes a relaxation to a Fermi distribution at lattice temperature  $T_L$  with a time constant  $\tau_{hx}$  associated with carrier-phonon scattering. Note that though  $T_L$  does not change with time, the corresponding distribution  $f_{xk}^L$  does because the total number of carriers is being increased or decreased via injection, spontaneous emission, sweep-out, etc. Finally the fourth term represents a return to steady state, described by the “carrier lifetime”  $\tau_s$ .

The time evolution of the coherence is given by

$$\frac{\partial \sigma_k}{\partial t} = i(\omega_k - \omega_0)\sigma_k - \frac{\sigma_k}{\tau_{2k}} - \frac{i}{\hbar} \mu_k E (\rho_{ck} + \rho_{vk} - 1). \quad 5.18$$

The first term on the RHS of Eq. (5.18) is the effect of detuning between the electric field frequency  $\omega_0$  and the resonant frequency of the transition  $\omega_k$ . The second term describes the dephasing of the quantum coherence with time constant  $\tau_{2k}$ . The final term describes the coherence established by the electromagnetic field.

In addition to the occupation and coherence, Eq. (5.12) and Eq. (5.13) can be used to formulate rate equations for the carrier temperature and carrier density. The total carrier density  $N$

$$\frac{\partial N}{\partial t} = -\frac{N - N_0}{\tau_s} - i \frac{\mu}{\hbar V} \sum_k (\sigma_k E^* - \sigma_k^* E). \quad 5.19$$

where  $N_0$  is the steady state value of the carrier density and  $V$  is the volume of the active region. The evolution of carrier temperature is described by

$$\frac{\partial T_x}{\partial t} = -\frac{T_x - T_L}{\tau_{hx}} + 2K_x |E|^2 \left(\frac{\partial U_x}{\partial T_x}\right)^{-1} - i \left(\frac{\partial U_x}{\partial T_x}\right)^{-1} \cdot \frac{\mu}{\hbar V} \sum_k \left(\epsilon_{xk} - \frac{\partial U_x}{\partial N}\right) (\sigma_k E^* - \sigma_k^* E). \quad 5.20$$

The first term is the relaxation of carrier temperature to lattice temperature via carrier-phonon scattering (see RHS Eq. (5.12), 3<sup>rd</sup> term). The second and third terms describe the change in carrier temperature due to a change in total carrier energy  $U_x$ . The second term describes carrier heating due to free-carrier absorption [74], where  $K_x$  is a phenomenological proportionality constant describing the increase in energy of the population of carriers due to free carrier absorption. The third term is the change in temperature due to interband transitions.

Eq. (5.13) and (5.17) are typically solved by making the adiabatic approximation, where the derivative of the coherence  $\sigma_k$  is taken to be zero. Physically, this means that the material polarization responds instantaneously to the electric field. This approximation leads directly to the rate equation model for semiconductor lasers and amplifiers and was used in deriving Eq. (5.) and (5.20). However, once we have obtained the rate equations for carrier temperature and carrier density, we decline the adiabatic elimination of  $\sigma_k$  when we subsequently look for solutions to Eq. (5.17) – (5.20) as a system. Our analysis in this regime is based on earlier work on “virtual” carrier density and the macroscopic Stark effect [76,75].

We begin with the 1-D propagation equation

$$\frac{\partial E}{\partial z} + \frac{1}{v_g} \frac{\partial E}{\partial t} = \frac{i\omega_0}{2\varepsilon_0 c n_b} \Gamma \cdot P \quad 5.21$$

where  $E(z, t)$  and  $P(z, t)$  are the slowly varying amplitudes of the electric field and polarization,  $v_g$  is the “empty waveguide” group velocity,  $n_b$  is the background refractive index due to non-resonant effects, and  $\Gamma$  is the confinement factor. The first step beyond the adiabatic approximation is to take the polarization  $P$  to be not only proportional to electric field  $E$ , but also to the time derivative of the field [78,77]:

$$P(t) = \varepsilon_0 \left( \chi_0 E + \chi_1^{(1)} \frac{\partial E}{\partial t} + \chi_1^{(2)} \frac{E^2}{|E|^2} \cdot \frac{\partial E^*}{\partial t} \right). \quad 5.22$$

When Eq. (5.22) is inserted into (5.21), the new  $\chi_1$  susceptibility terms are collected together with  $v_g^{-1}$  to give a correction to the group velocity.

The group index change  $\Delta n_g$ , which is a function of carrier density  $N$  and photon density  $S$  (where  $S \propto |E|^2$ ), can be written as the sum of three contributions:

$$\Delta n_g = \Delta n_g^{lin}(N) + \Delta n_g^{SHB}(N, S) + \Delta n_g^{CH}(N, S) \quad 5.23$$

where  $\Delta n_g^{lin}$  is the “linear” change due to dispersion of the “linear” gain  $g(N)$  and where  $\Delta n_g^{SHB}$  and  $\Delta n_g^{CH}$  are the group index changes due to SHB and CH effects. Note that  $\Delta n_g^{lin}$  depends only on carrier density, and does not directly depend upon  $S$ . In contrast, the “nonlinear” changes in group index,  $\Delta n_g^{SHB}$  and  $\Delta n_g^{CH}$ , are functions of both  $N$  and  $S$ . As in [79,76,75], we have evaluated  $\Delta n_g^{SHB}$  and  $\Delta n_g^{CH}$  to first order in  $S$ . In our numerical simulations and the results shown in the remainder of this section, contributions from  $\Delta n_g^{lin}$  are negligible and are neglected.

It may not be readily apparent that CH should contribute significantly to the group index. Typically, large contributions to group velocity are made by the dispersion of refractive index; i.e. they are due to dip- or hole-like spectral features where transmission changes over a small range of wavelengths. Conversely, when the temperature of the carriers is raised, transmission decreases at all wavelengths. However, CH can still produce a spectral dip via a dynamical effect, similar to CPO. In the case of CPO, the carrier density oscillates at the beat frequency between the spectral components of the pulse and the pump. The nanosecond carrier lifetime limits the bandwidth of this effect to a few gigahertz. The carrier temperature can respond much faster than the carrier density, so the temperature of the distribution can pulsate at THz frequencies and act over the entire bandwidth of a sub-picosecond pulse. The pulse acts as both pump and signal, and the oscillation of temperature mixes the frequency components of the pulse in such a way that the pulse experiences a nonlinear change in group index:

$$\Delta n_g^{CH} = -c\tau_h \varepsilon_{CH} \cdot g_0(N) \cdot S \quad 5.24$$

where  $\varepsilon_{CH}$  is the gain suppression factor due to carrier heating (see Eq. (5.16) ).

In fact, these dynamical effects are also important in the SHB term. There are two contributions to  $\Delta n_g^{SHB}$  such that

$$\Delta n_g^{SHB} = \Delta n_g^{SHB-DIP} + \Delta n_g^{SHB-WM} \quad 5.25$$

First there is an incoherent contribution due to the “dip” in the gain spectrum and consequent dispersion, as required by the Kramers-Kronig relations:

$$\Delta n_g^{SHB-DIP} = -\frac{c\tau_2 \varepsilon_{SHB}}{4} \cdot g_0(N) \cdot S \quad 5.26$$

where  $\varepsilon_{SHB}$  is the gain suppression factor for SHB (see Eq. (5.16)) and  $\tau_2$  is the dephasing time. It is important to note that incoherent effects such as the SHB dip can be calculated *without* going beyond the adiabatic approximation. The coherent contribution obtained by declining the adiabatic approximation yields the second term in Eq. (5.25)

$$\Delta n_g^{SHB-WM} = -3\frac{c\tau_2 \varepsilon_{SHB}}{4} \cdot g_0(N) \cdot S \quad 5.27$$

This contribution is labeled SHB-WM for “wave-mixing.” Physically, this represents wave mixing between spectral components of the pulse due to pulsations of the carrier distribution. Damped by carrier-carrier scattering, these oscillations can respond even faster than the carrier temperature and can mix frequency components across the entire bandwidth of a sub-picosecond pulse. These dynamical effects are in fact the dominant contribution to the SHB nonlinear index:  $\Delta n_g^{SHB-WM} = 3\Delta n_g^{SHB-DIP}$ .

Figure 5.30(a) shows the result of adding the nonlinear group index to the inter- and intraband saturation effects (green). For comparison, the saturation-only pulses shown in Figure 5.29 are also included on Figure 5.30(a). The nonlinear group index clearly plays a dominant role in the advance of the pulse, achieving an ABP of almost 2.0. This demonstrates the previously unknown importance of the nonlinear group index. Also visible is a pulse steepening effect. The nonlinear group index is larger at higher photon density, so the peak of the pulse moves faster than the base. This causes the pulse to experience substantial broadening. While it is true that our experimental pulses also

experienced broadening on the order of 200% (see Figure 5.7(b) ), the experimentally measured broadening is relatively constant with bias current and is easily removed by a fixed dispersion compensation, indicating it is due to some “background” GVD. The broadening from our model observed in Figure 5.30 increases as the bias current is increased from transparency.

Figure 5.30(b) is the comparison of our theory (green) with experiment (black). For this figure, the simulated pulse has been cross-correlated with the input. After cross-correlation the pulse shape is qualitatively closer to that measured experimentally. However, the advance of the peak has also decreased slightly and the theory now can account for only roughly half of the total advance. There are several effects which are not yet taken into account in our simple calculations. Two effects which may be important in determining overall pulse shape are GVD and gain dispersion. Another important point is that Eq. (5.24) – (5.27) are derived in the limit  $\varepsilon_x S \ll 1$ , where  $x = SHB, CH$ . For the simulation, these equation are extended *phenomenologically* and by analogy to carrier density pulsations to higher photon density by the substitution

$$\varepsilon_x S \rightarrow \frac{\varepsilon_x S}{(1 + \varepsilon_x S)^2}. \quad 5.28$$

More details regarding these calculations can be found in [77].

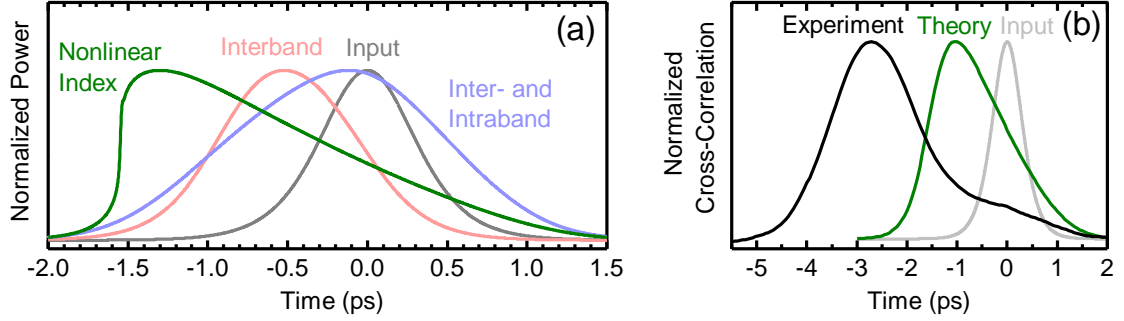


**Figure 5.30(a).** Numerical simulation of pulse advance due to nonlinear group index for a 700 fs input pulse (green). Pulses propagating with purely linear gain, interband saturation, and interband plus intraband saturation are shown in light gray, red, and blue, respectively, as in Figure 5.29. The effects due to nonlinear group index are clearly dominant, shifting the peak of the pulse forward by almost two pulse widths, and nearly matching the ABP of 2.5 observed in experiment. **Figure 5.30(b).** After cross-correlation the calculated pulse with the input (green) the peak shifts back slightly and the self-steepening is hidden. Also shown in the experimental result from Section 5.3 (black). It is clear that the theory still cannot completely explain the large advance observed.

The equations for the nonlinear group index, Eq. (5.24) – (5.27), have been derived in the time domain. However, the same expressions may also be obtained from the CW pump-signal model used in Ref [79]. in the limit that  $\delta \ll \tau_1^{-1}, \tau_2^{-1}, \tau_h^{-1}$ , where  $\delta$  is the pump-signal detuning. The pump-signal experiment can also be considered a case of single sinusoidal signal acting as both pump and signal simultaneously. The agreement between the two analyses is a good check of theory and further supports our physical interpretation of the coherent terms in  $\Delta n_g$ .

## 6 Conclusion

In the beginning, we had no slow light device on which to experiment and thus turned to simulation. Simulations of a slow light device operating in an optical communications link reveal important and general results. At the time it was well understood that there is a trade-off between the delay and the bandwidth and that it was their product, the DBP, which was a more significant metric. The DBP was actually a

storage per unit length, since the delay was assumed to scale linearly with  $L$ . The length was assumed to be limited only by residual absorption.

The most important result from our simulation is the storage-bit rate product (SBP). If the loss (or gain) is not constant over the bandwidth of the signal then the device 1) has a maximum length and therefore maximum total storage and 2) is subject to a tradeoff between the maximum storage and the operating bandwidth. Because the SBP depends on the square of the bandwidth, it is much more important to increase the bandwidth for a given delay than to increase the delay at a given bandwidth, when optimizing a slow light device for use as a storage component.

Our experimental accomplishments began shortly after we started the simulations. We measured and quantified the first slow light dispersion in semiconductors using the CPO effect. Time domain measurements followed shortly thereafter and then waveguide geometry and room temperature operation. The latter was the first CPO on (110) GaAs QW, and thus was an important first step in realizing EIT at room temperature. We were able to observe EIT based on spin coherence in (110) QW up to 100 K, limited by our experimental apparatus. The spin coherence time, inferred from the linewidth of the EIT resonance, appears to be constant with increasing temperature. Unfortunately, EIT has yet to be observed at room temperature, but the above results give hope that it may still be possible.

We then show how the nonzero linewidth enhancement parameter of QW SOAs can be used to implement both slow and fast light in a gain medium. Such gain-based CPO slow light devices do not suffer from disadvantages such as pump absorption and

residual signal absorption. Additionally, a single device can provide a greater amount of overall temporal shift by switching between slow and fast light detuning. However, simulations of such a device in an optical communications link indicate that gain experienced by the signal can cause almost as many complications as residual absorption. This leads to a cascade design of alternating gain-based slow light devices and attenuators such that the average signal gain is zero. At this point we find that the maximum delay is limited by distortion and the amount of power penalty allowed in the power budget of the link.

Finally, we have presented novel research into fast light in SOAs using the intraband processes of spectral hole burning and carrier heating. The ABP of 2.5 is a record for any slow or fast light system in semiconductors. We then present a very novel method of enhancing the performance of this scheme by imposing a linear chirp on pulses at the device input, allowing different spectral components to enter the device at different times and then removing the chirp at the output. We call this scheme time-wavelength division multiplexing (TWDM). We find that the advance can be increased to 6.5 with this scheme. Additionally, we find that by using chirp of the opposite sign, a delay can be realized via a completely different physical mechanism. We demonstrate a combined A/DBP of more than 10 pulses and present a schematic for a device which allows simple switching between delay and advance.

Slow light effects from atomic systems served as an inspiration for this project, but had limited bandwidth (from  $\sim 100$  Hz to  $\sim 100$  kHz) and operated at wavelengths unsuitable for optical communications. We were able to implement EIT and CPO in GaAs

quantum wells and observed a bandwidth increase of more than three orders of magnitude, to  $\sim 1$  GHz. However, the DBP was never more than 0.1 and the wavelengths were not compatible with telecommunications. Next we implemented CPO in an SOA and the DBP increased to 0.3, but in telecom devices at room temperature. Finally, we moved to intraband effects and measured ABP of 2.5 and then, with TWDM, A/DBP of 10, a factor of 100 larger than our initial results. The THz bandwidth of the sub-picosecond pulses is a three orders of magnitude improvement over our early work and more than size orders of magnitude improvement over the original slow light experiments.

## 7 Appendix: Auto- and Cross-Correlation

Autocorrelation is a method of measuring ultrafast pulses developed in the late 1960's [80]. The pulse to be measured is sent through a beam splitter and divided along two paths. The length of one of the paths may be varied, implementing a variable delay between the pulses. The two paths are then brought back together within a nonlinear crystal. The delay is swept and when the pulses overlap, a second harmonic signal is generated. The intensity of the second harmonic signal  $I_{SHG}$  as a function of delay  $\tau$  follows the correlation of the intensities of the two pulses

$$I_{SHG}(\tau) = \frac{\int I(t)I(t - \tau)dt}{\int I(t)^2 dt}. \quad 7.1$$

Autocorrelation does not provide enough information to calculate the shape of the original pulse. The autocorrelation signal is always symmetric and tends to “wash out” any complex structure the pulse may have.

A key parameter one seeks from autocorrelation measurements is the pulse duration. If the functional form of the pulse is known in advance, then the FWHM of the original pulse is calculated from the FWHM of the autocorrelation function by using an appropriate conversion factor [81]. Common practice is to make a reasonable assumption of the pulse shape, typically  $\text{sech}^2$  for mode-locked lasers, and estimate FWHM of the pulse with the corresponding conversion factor, 0.65 for  $\text{sech}^2$ . When calculating pulse broadening, the ratio of the FWHM of the autocorrelation pulses may be used as long as the pulse shape does not change significantly.

A second technique, cross-correlation, is very similar to auto-correlation, except that the pulse collides with a separate reference pulse instead. Cross-correlation is important in our experiments because unlike autocorrelation it can detect a temporal shift of the signal pulse. Also, there are two situations in which calculating the signal pulse duration is trivial. First, if the shape of the reference pulse is known, then the shape of the original pulse can be calculated. Second, if the reference pulse is much shorter than the signal pulse, then the cross-correlation trace is approximately equal to the signal pulse intensity. As with autocorrelation, pulse broadening can be calculated from the FWHM of the correlation trace even if neither of the above conditions are true, as long as the pulse shape does not change.

When the pulse shape differs between input and output, the broadening can still be quantified using the root-mean-square (RMS) width of the pulses [27]. The RMS width of a function  $f(t)$  is given by

$$\sigma = \sqrt{\int t^2 \cdot f(t) dt - \left( \int t \cdot f(t) dt \right)^2} . \quad 7.2$$

The RMS width of an auto- or cross-correlation signal is related to the RMS widths of the constituent pulses by [82]

$$\sigma_{corr} = \sqrt{\sigma_1^2 + \sigma_2^2} \quad 7.3$$

where for auto-correlation  $\sigma_1 = \sigma_2$ . For measurements of pulse broadening (Section 5.4.2) the RMS width of the reference pulse  $\sigma_{ref}$  is first determined by auto-correlation, then the RMS of the signal pulse can be determined from the cross-correlation measurements by inserting  $\sigma_{ref}$  into Eq. (7.3). Note that the RMS width is an appropriate metric for calculating pulse broadening when the shape of the pulse is changing, but the FWHM remains a more appropriate (and generally accepted) metric for pulse duration when calculating the DBP and ABP.

## 8 Bibliography

- [1] ] L.V. Hau et al., "Light speed reduction to 17 metres per second in an ultracold atomic gas," *Nature*, vol. 397, Feb. 1999, pp. 594-598.
- [2] ] S.E. Harris, J.E. Field, and A. Kasapi, "Dispersive properties of electromagnetically induced transparency," *Physical Review A*, vol. 46, Jul. 1992, p. R29.
- [3] ] A. Kasapi et al., "Electromagnetically Induced Transparency: Propagation Dynamics," *Physical Review Letters*, vol. 74, Mar. 1995, p. 2447.

- [4 ] L. Brillouin, *Wave propagation and group velocity.*, New York: Academic Press, 1960.
- [5 ] J. E. Heebner, R.W. Boyd, and Q. Park, "Slow light, induced dispersion, enhanced nonlinearity, and optical solitons in a resonator-array waveguide," *Physical Review E*, vol. 65, Mar. 2002, p. 036619.
- [6 ] S.E. Harris and L.V. Hau, "Nonlinear Optics at Low Light Levels," *Physical Review Letters*, vol. 82, Jun. 1999, p. 4611.
- [7 ] M.M. Kash et al., "Ultraslow Group Velocity and Enhanced Nonlinear Optical Effects in a Coherently Driven Hot Atomic Gas," *Physical Review Letters*, vol. 82, Jun. 1999, p. 5229.
- [8 ] M.D. Lukin and A. Imamoglu, "Nonlinear Optics and Quantum Entanglement of Ultraslow Single Photons," *Physical Review Letters*, vol. 84, Feb. 2000, p. 1419.
- [9 ] C. Liu et al., "Observation of coherent optical information storage in an atomic medium using halted light pulses," *Nature*, vol. 409, Jan. 2001, pp. 490-493.
- [10 ] M. Fleischhauer and M.D. Lukin, "Dark-State Polaritons in Electromagnetically Induced Transparency," *Physical Review Letters*, vol. 84, May. 2000, p. 5094.
- [11 ] M.F. Yanik and S. Fan, "Stopping and storing light coherently," *Physical Review A (Atomic, Molecular, and Optical Physics)*, vol. 71, Jan. 2005, pp. 013803-10.
- [12 ] A. Seeds, "Microwave photonics," *Microwave Theory and Techniques, IEEE Transactions on*, vol. 50, 2002, pp. 877-887.
- [13 ] C.J. Chang-Hasnain et al., "Variable optical buffer using slow light in semiconductor nanostructures," *PROCEEDINGS OF THE IEEE*, vol. 91, Nov. 2003, pp. 1884-1897.
- [14 ] R. Minasian, "Photonic signal processing of microwave signals," *Microwave Theory and Techniques, IEEE Transactions on*, vol. 54, 2006, pp. 832-846.
- [15 ] K. Jackson et al., "Optical Fiber Delay-Line Signal Processing," *Microwave Theory and Techniques, IEEE Transactions on*, vol. 33, 1985, pp. 193-210.

- [16 ] J. Capmany et al., "Discrete-Time Optical Processing of Microwave Signals," *J. Lightwave Technol.*, vol. 23, 2005, p. 702.
- [17 ] S.J.B. Yoo, "Optical Packet and Burst Switching Technologies for the Future Photonic Internet," *Lightwave Technology, Journal of*, vol. 24, Dec. 2006, pp. 4468-4492.
- [18 ] Z. Zhu et al., "High-Performance Optical 3R Regeneration for Scalable Fiber Transmission System Applications," *J. Lightwave Technol.*, vol. 25, Feb. 2007, pp. 504-511.
- [19 ] D. Wolfson et al., "40-Gb/s all-optical wavelength conversion, regeneration, and demultiplexing in an SOA-based all-active Mach-Zehnder interferometer," *Photonics Technology Letters, IEEE*, vol. 12, Mar. 2000, pp. 332-334.
- [20 ] P. Ku, C. Chang-Hasnain, and S. Chuang, "Variable semiconductor all-optical buffer," *Electronics Letters*, vol. 38, Nov. 2002, pp. 1581-1583.
- [21 ] R.S. Tucker, P.C. Ku, and C.J. Chang-Hasnain, "Slow-light optical buffers: Capabilities and fundamental limitations," *JOURNAL OF LIGHTWAVE TECHNOLOGY*, vol. 23, Dec. 2005, pp. 4046-4066.
- [22 ] S.L. Chuang, *Physics of Optoelectronic Devices*, Wiley-Interscience, 1995.
- [23 ] R.H. Pantell and H.E. Puthoff, *Fundamentals of Quantum Electronics*, John Wiley & Sons Inc, 1969.
- [24 ] P. Ku, "Semiconductor Slow-Light Device," Oct. 2003.
- [25 ] A. Yariv, *Quantum Electronics, 3rd Edition*, Wiley, 1989.
- [26 ] S.M. Reimann and M. Manninen, "Electronic structure of quantum dots," *Reviews of Modern Physics*, vol. 74, Nov. 2002, p. 1283.
- [27 ] G.P. Agrawal, *Fiber-Optic Communication Systems*, Wiley-Interscience, 2002.
- [28 ] R. Tucker et al., "Delay-bandwidth product and storage density in slow-light optical buffers," *Electronics Letters*, vol. 41, Feb. 2005, pp. 208-209.

- [29 ] D.S. Chemla and D.A.B. Miller, "Room-temperature excitonic nonlinear-optical effects in semiconductor quantum-well structures," *J. Opt. Soc. Am. B*, vol. 2, 1985, p. 1155.
- [30 ] M. Phillips and H. Wang, "Spin Coherence and Electromagnetically Induced Transparency via Exciton Correlations," *Physical Review Letters*, vol. 89, Oct. 2002, p. 186401.
- [31 ] M.C. Phillips et al., "Electromagnetically Induced Transparency in Semiconductors via Biexciton Coherence," *Physical Review Letters*, vol. 91, Oct. 2003, p. 183602.
- [32 ] M. Phillips and H. Wang, "Electromagnetically induced transparency due to intervalence band coherence in a GaAs quantum well," *Opt. Lett.*, vol. 28, 2003, pp. 831-833.
- [33 ] S. Sarkar et al., "Inducing electron spin coherence in GaAs quantum well waveguides: Spin coherence without spin precession," *Physical Review B (Condensed Matter and Materials Physics)*, vol. 72, Jul. 2005, pp. 035343-5.
- [34 ] S. Chang et al., "Slow light using spin coherence and V-type electromagnetically induced transparency in [110] strained quantum wells," *JOURNAL OF THE OPTICAL SOCIETY OF AMERICA B-OPTICAL PHYSICS*, vol. 24, Mar. 2007, pp. 849-859.
- [35 ] T. Li et al., "Electromagnetically induced transparency via electron spin coherence in a quantum well waveguide," *Opt. Express*, vol. 11, 2003, pp. 3298-3303.
- [36 ] I. Žutić, J. Fabian, and S. Das Sarma, "Spintronics: Fundamentals and applications," *Reviews of Modern Physics*, vol. 76, Apr. 2004, p. 323.
- [37 ] Y. Ohno et al., "Spin Relaxation in GaAs(110) Quantum Wells," *Physical Review Letters*, vol. 83, Nov. 1999, p. 4196.
- [38 ] S. Dörhmann et al., "Anomalous Spin Dephasing in (110) GaAs Quantum Wells: Anisotropy and Intersubband Effects," *Physical Review Letters*, vol. 93, Oct. 2004, p. 147405.
- [39 ] F. Meier and B.P. Zakharchenya, *Optical Orientation*, North-Holland, 1984.
- [40 ] M.S. Bigelow, N.N. Lepeshkin, and R.W. Boyd, "Observation of Ultraslow Light Propagation in a Ruby Crystal at Room Temperature," *Physical Review Letters*, vol. 90, Mar. 2003, p. 113903.

- [41 ] H. Wang, M. Jiang, and D.G. Steel, "Measurement of phonon-assisted migration of localized excitons in GaAs/AlGaAs multiple-quantum-well structures," *Physical Review Letters*, vol. 65, 1990, p. 1255.
- [42 ] P.C. Ku et al., "Slow light in semiconductor quantum wells," *OPTICS LETTERS*, vol. 29, Oct. 2004, pp. 2291-2293.
- [43 ] M. Xiao et al., "Measurement of Dispersive Properties of Electromagnetically Induced Transparency in Rubidium Atoms," *Physical Review Letters*, vol. 74, Jan. 1995, p. 666.
- [44 ] H. Wang et al., "Transient nonlinear optical response from excitation induced dephasing in GaAs," *Physical Review Letters*, vol. 71, 1993, p. 1261.
- [45 ] K. Ogawa, T. Katsuyama, and H. Nakamura, "Time-of-flight measurement of excitonic polaritons in a GaAs/AlGaAs quantum well," *Applied Physics Letters*, vol. 53, 1988, pp. 1077-1079.
- [46 ] J.Q. Liang et al., "Slow light produced by stimulated Raman scattering in solid hydrogen," *Physical Review A*, vol. 65, Feb. 2002, p. 031801.
- [47 ] H. Wang et al., "High resolution laser spectroscopy of relaxation and the excitation lineshape of excitons in GaAs quantum well structures," *Surface Science*, vol. 228, Apr. 1990, pp. 69-73.
- [48 ] P. Palinginis et al., "Ultraslow light (< 200 m/s) propagation in a semiconductor nanostructure," *APPLIED PHYSICS LETTERS*, vol. 87, Oct. 2005.
- [49 ] P. Palinginis et al., "Room temperature slow light in a quantum-well waveguide via coherent population oscillation," *OPTICS EXPRESS*, vol. 13, Nov. 2005, pp. 9909-9915.
- [50 ] K. Vahala et al., "On the linewidth enhancement factor alpha in semiconductor injection lasers," *Applied Physics Letters*, vol. 42, Apr. 1983, pp. 631-633.
- [51 ] "2005EL\_Slow and superluminal light in SOA (Uskov).pdf."
- [52 ] F. Öhman, K. Yvind, and J. Mørk, "Voltage-controlled slow light in an integrated semiconductor structure with net gain," *Opt. Express*, vol. 14, Oct. 2006, pp. 9955-9962.

- [53 ] F. Ohman et al., "Slow Light in a Semiconductor Waveguide for True-Time Delay Applications in Microwave Photonics," *Photonics Technology Letters, IEEE*, vol. 19, Aug. 2007, pp. 1145-1147.
- [54 ] S. Sales Maicas et al., "Controlling Microwave Signals by Means of Slow and Fast Light Effects in SOA-EA Structures," *Photonics Technology Letters, IEEE*, vol. 19, Oct. 2007, pp. 1589-1591.
- [55 ] B. Pesala et al., "Experimental demonstration of slow and superluminal light in semiconductor optical amplifiers," *OPTICS EXPRESS*, vol. 14, Dec. 2006, pp. 12968-12975.
- [56 ] R.Y. Chiao, "Superluminal (but causal) propagation of wave packets in transparent media with inverted atomic populations," *Physical Review A*, vol. 48, Jul. 1993, p. R34.
- [57 ] S. Chu and S. Wong, "Linear Pulse Propagation in an Absorbing Medium," *Physical Review Letters*, vol. 48, Mar. 1982, p. 738.
- [58 ] K.L. Hall et al., "Subpicosecond gain and index nonlinearities in InGaAsP diode lasers," *Optics Communications*, vol. 111, Oct. 1994, pp. 589-612.
- [59 ] R.M. Camacho, M.V. Pack, and J.C. Howell, "Slow light with large fractional delays by spectral hole-burning in rubidium vapor," *PHYSICAL REVIEW A*, vol. 74, Sep. 2006.
- [60 ] M.P. Kesler and E.P. Ippen, "Subpicosecond gain dynamics in GaAlAs laser diodes," *Applied Physics Letters*, vol. 51, Nov. 1987, pp. 1765-1767.
- [61 ] T.L. Koch et al., "Picosecond carrier dynamics and laser action in optically pumped buried heterostructure lasers," *Applied Physics Letters*, vol. 41, Jul. 1982, pp. 6-8.
- [62 ] Z. Vardeny and J. Tauc, "Picosecond coherence coupling in the pump and probe technique," *Optics Communications*, vol. 39, Nov. 1981, pp. 396-400.
- [63 ] K.L. Hall et al., "Femtosecond gain dynamics in InGaAsP optical amplifiers," *Applied Physics Letters*, vol. 56, Apr. 1990, pp. 1740-1742.
- [64 ] A. D'Ottavi et al., "4.3 terahertz four-wave mixing spectroscopy of InGaAsP semiconductor amplifiers," *Applied Physics Letters*, vol. 65, Nov. 1994, pp. 2633-2635.

- [65 ] S. Sarkar, Y. Guo, and H.L. Wang, "Tunable optical delay via carrier induced exciton dephasing in semiconductor quantum wells," *OPTICS EXPRESS*, vol. 14, Apr. 2006, pp. 2845-2850.
- [66 ] R.W. Boyd and P. Narum, "Slow- and fast-light: fundamental limitations," *Journal of Modern Optics*, vol. 54, 2007, pp. 2403-2411.
- [67 ] E. Treacy, "Optical pulse compression with diffraction gratings," *Quantum Electronics, IEEE Journal of*, vol. 5, Sep. 1969, pp. 454-458.
- [68 ] O. Martinez and O. Martinez, "3000 times grating compressor with positive group velocity dispersion: Application to fiber compensation in 1.3-1.6  $\mu\text{m}$  region," *Quantum Electronics, IEEE Journal of*, vol. 23, Jan. 1987, pp. 59-64.
- [69 ] N.A. Olsson and G.P. Agrawal, "Spectral shift and distortion due to self-phase modulation of picosecond pulses in 1.5  $\mu\text{m}$  optical amplifiers," *Applied Physics Letters*, vol. 55, Jul. 1989, pp. 13-15.
- [70 ] G. Agrawal, G. Agrawal, and N. Olsson, "Self-phase modulation and spectral broadening of optical pulses in semiconductor laser amplifiers," *Quantum Electronics, IEEE Journal of*, vol. 25, 1989, pp. 2297-2306.
- [71 ] Y. Lin and G. Lin, "Dual-stage soliton compression of a self-started additive pulse mode-locked erbium-doped fiber laser for 48 fs pulse generation," *Opt. Lett.*, vol. 31, May. 2006, pp. 1382-1384.
- [72 ] G. Lin, Y. Lin, and C. Lee, "Simultaneous pulse amplification and compression in all-fiber-integrated pre-chirped large-mode-area Er-doped fiber amplifier," *Opt. Express*, vol. 15, Mar. 2007, pp. 2993-2999.
- [73 ] M. van der Poel, J. Mork, and J.M. Hvam, "Controllable delay of ultrashort pulses in a quantum dot optical amplifier," *OPTICS EXPRESS*, vol. 13, Oct. 2005, pp. 8032-8037.
- [74 ] B. Gomati and A. DeFonzo, "Theory of hot carrier effects on nonlinear gain in GaAs-GaAlAs lasers and amplifiers," *Quantum Electronics, IEEE Journal of*, vol. 26, Oct. 1990, pp. 1689-1704.
- [75 ] J. Mork and A. Mecozzi, "Non-adiabatic effects in semiconductor waveguides," *Physics and Simulation of Optoelectronic Devices VIII*, R.H. Binder, P. Blood, and M. Osinski, eds., SPIE, 2000, pp. 658-672; <http://link.aip.org/link/?PSI/3944/658/1>.

- [76 ] J. Mork and A. Mecozzi, "Dispersion-induced nonlinearities in semiconductors," *Optics Communications*, vol. 210, Sep. 2002, pp. 173-177.
- [77 ] A.V. Uskov et al., "Ultrafast nonlinear group index and fast light in semiconductor optical amplifiers," Oct. 2007.
- [78 ] A.V. Uskov, F.G. Sedgwick, and C.J. Chang-Hasnain, "Ultrafast Nonlinear Group Index in Semiconductor Optical Amplifiers for Slow and Fast Light," San Jose, CA: 2007.
- [79 ] A. Uskov, J. Mork, and J. Mark, "Wave Mixing In Semiconductor-Laser Amplifiers Due To Carrier Heating and Spectral Hole Burning," *IEEE JOURNAL OF QUANTUM ELECTRONICS*, vol. 30, Aug. 1994, pp. 1769-1781.
- [80 ] H.P. Weber, "Method for Pulsewidth Measurement of Ultrashort Light Pulses Generated by Phase-Locked Lasers using Nonlinear Optics," *Journal of Applied Physics*, vol. 38, Apr. 1967, pp. 2231-2234.
- [81 ] J.M. Diels et al., "Control and measurement of ultrashort pulse shapes (in amplitude and phase) with femtosecond accuracy," *Appl. Opt.*, vol. 24, May. 1985, p. 1270.
- [82 ] E.T. Jaynes, *Probability Theory: The Logic of Science*, Cambridge University Press, 2003.